INFORMATION TO USERS

This manuscript has been reproduced from the microfilm master. UMI films the text directly from the original or copy submitted. Thus, some thesis and dissertation copies are in typewriter face, while others may be from any type of computer printer.

The quality of this reproduction is dependent upon the quality of the copy submitted. Broken or indistinct print, colored or poor quality illustrations and photographs, print bleedthrough, substandard margins, and improper alignment can adversely affect reproduction.

In the unlikely event that the author did not send UMI a complete manuscript and there are missing pages, these will be noted. Also, if unauthorized copyright material had to be removed, a note will indicate the deletion.

Oversize materials (e.g., maps, drawings, charts) are reproduced by sectioning the original, beginning at the upper left-hand corner and continuing from left to right in equal sections with small overlaps.

Photographs included in the original manuscript have been reproduced xerographically in this copy. Higher quality 6" x 9" black and white photographic prints are available for any photographs or illustrations appearing in this copy for an additional charge. Contact UMI directly to order.

ProQuest Information and Learning
300 North Zeeb Road, Ann Arbor, MI 48106-1346 USA
800-521-0600

UMI®

Reproduced with permission of the copyright owner. Further reproduction prohibited without permission.

DISSERTATION

THE SUCTION INDUCED BY CONICAL VORTICES ON LOW-RISE BUILDINGS WITH FLAT ROOFS

Submitted by

David Banks

Civil Engineering Department

In partial fulfillment of the requirements

For the Degree of Doctor of Philosophy

Colorado State University

Fort Collins, Colorado

Spring 2000

UMI Number: 3013876

UMI Microform 3013876

Bell & Howell Information and Learning Company
300 North Zeeb Road
P.O. Box 1346
Ann Arbor, MI 48106-1346

COLORADO STATE UNIVERSITY

April 11, 2000

WE HEREBY RECOMMEND THAT THE DISSERTATION PREPARED UNDER OUR SUPERVISION BY **DAVID BANKS** ENTITLED **THE SUCTION INDUCED BY CONICAL VORTICES ON LOW-RISE BUILDINGS WITH FLAT ROOFS** BE ACCEPTED AS FULFILLING IN PART REQUIREMENTS FOR THE DEGREE OF DOCTOR OF PHILOSOPHY.

Committee on Graduate Work

Pierre Julien

Robert N. Meroney
Advisor

Department Head

ABSTRACT OF DISSERTATION

THE SUCTION INDUCED BY CONICAL VORTICES ON LOW-RISE BUILDINGS WITH FLAT ROOFS

Wind tunnel and full scale pressure studies of the flow over low-rise buildings have repeatedly shown that the largest mean, peak, and rms suction values observed anywhere on the building occur beneath the dual conical vortices that form along the leading edges of the roof during cornering winds. The manner in which these vortices cause extreme suction events is not well understood. In addition, pressures beneath the vortices display a range of unusual characteristics, such as the failure to adhere to quasi-steady theory, and discrepancies between wind tunnel and full-scale measurements.

The objective of this study is to examine the process or "flow mechanism" by which a vortex instantaneously controls rooftop suctions. By better understanding the workings of the vortex itself, the upstream flow conditions which influence vortex behaviour can be directly connected to these suctions. This then permits the unusual pressure characteristics to be examined methodically.

A unique experimental facility was developed to simultaneously record images of a vortex while measuring pressures beneath the visualization plane and flow velocities nearby. A new analytical model for the vortex pressure field was also developed and assessed experimentally. The model quantifies how two parameters, streamline curvature and flow speed above the vortex, control surface pressure. Experimental measurements confirm that the model accounts for changes in surface pressure with wind direction and proximity to the roof corner solely on the basis of these parameters.

A full evaluation of the application of quasi–steady theory to pressures beneath the vortices is performed. Data gathered during the experiments and an analysis of the flow model show explicitly how the quasi-steady theory fails to accurately predict the condition and location of the vortex, though it does capture the essence of pressure changes due to vortex motion.

Finally, the model suggests that by inhibiting the flow reattachment, the effect of the vortices on the roof can be eliminated. Several retrofit mitigation techniques that perform this role are assessed experimentally, and compared to the potential for suction reduction circumscribed by the model.

David Banks
Fluid Mechanics and Wind Engineering
Civil Engineering Department
Colorado State University
Fort Collins, Co 80523
Spring 2000

ACKNOWLEDGEMENTS

I would like to thank my father, Ivor Banks, for his help in working through the vortex model, and for introducing me to Monty Python at an early age.

I would like to thank the best university educator I have ever met, Prof. Bob Meroney, for advising this research patiently and supportively.

I am also grateful to Dr. David Neff and Dr. Bernd Leitl for their extensive help in the laboratory, and to Prof. David Surry for regularly offering advice and encouragement.

TABLE OF CONTENTS

LIST OF SYMBOLS

a	Normalized z-direction distance from the core
B	Largest building plan dimension (either Length or Width)
C_1	Arbitrary constant
C_p	Pressure coefficient = $(P-P_{ref})/\frac{1}{2}\rho U^2_{ref}$
Cp_{inner}	Cp in viscous region of a Rankine votex
Cp_{min}	Minimum pressure coefficient along a given x = constant line (same as Cp_S)
Cp_o	Pressure Coefficient at the vortex core
Cp_{outer}	Cp in inviscid region of a Rankine votex
Cp_M	Cp at the point M (directly above the vortex core)
Cp_S	Cp at the point S (on the roof surface, directly beneath the vortex core)
$Cp^{nom\theta}$	Mean Cp as a function of the nominal wind angle
$Cp^{inst\theta}$	Mean Cp as a function of the instantaneous wind angle
Cp^N	Cp corrected by the normalized local velocity
$C_{\bar{p}}, C_{\sigma_p}, C_{\check{p}}$	Mean, rms, and peak negative values of the pressure coefficient time series $C_p(t)$, where $C_p(t) = (P(t)-P_{ref})/\frac{1}{2}\rho U^2_{ref})$
Cp_{mean},Cp_{rms}	Mean and rms values of pressure coefficient time series
Cp_{rms_TI}	Component of Cp_{rms} due to Turbulence Intensity
Cp_{rms_X}	Component of Cp_{rms} due to variable 'X'; variables include θ, g', and ω'.
f	frequency
$f_x(x)$	Probability Distribution Function (pdf) for the variable 'x'
g	Integral of centripetal acceleration from inviscid region, through core, to roof
g_s	Value of g at the point S
h	Height or distance of the vortex core above the roof surface
h_0	Height of the vortex core above the roof surface at the roof apex ($x = 0$)
H	Height of building or prism
I_U	Turbulence intensity in the longitudinal (along wind) direction

k	Arbitrary constant
L_x	Integral scale
n	Unit normal to streamline
P	Static pressure
P_∞	Static pressure at the stagnation point (when $U = 0$)
q	Flow head = $\frac{1}{2}\rho U^2$
r	Radial distance from the vortex core
R	Radial distance of border between viscous and inviscid flow in Rankine vortex
R_c	Radius of curvature
t	Time
$\vec{u}$	Flow velocity vector
U	Flow speed
U_{ref}	Flow speed measured upstream at roof height
U_{max}	Maximum mean velocity above the vortex core
$U_{(point)}$	U at the location (point) ex: U_C, U_M
u	Flow velocity fluctuations in the direction of the mean flow vector
v, w	Horizontal flow velocity fluctuations normal to the mean flow vector
x	Distance from the apex or leading edge corner, measured along the leading edge
y	Distance from the leading edge wall, along a line normal to the leading edge
$y_{1/2}$	Half width of the of the y-direction pressure profile suction peak.
z	Distance above the roof surface
z_m	Theoretical vortex core height above roof surface, used in potential flow theory
α	Wind angle above the vortex, relative to the vortex core axis
β	Wind angle due to vertical component of wind
ΔCp^N	Drop in Cp^N from M to S due to vortex; see Equation (3.4)
ΔP_{min}	P-P_∞ directly beneath the vortex, on the roof surface
$\Delta x, \Delta h, \Delta y$	Incremental change in the quantities x, h, or y.
ϕ	Angle formed along the roof surface with respect to the leading edge
$\phi_{\bar{c}}$	Angle formed between the ray of the mean vortex core position and the leading edge
$\phi_{\bar{p}}, \phi_{\sigma_p}, \phi_{\check{p}}$	Angles between the leading edge and the rays of highest - $C_{\bar{p}}$, $C\sigma_p$, and $C_{\check{p}}$
η	Transfer function to calculate Cp at a fixed tap based on tap location and Cp_S.

θ	Horizontal wind direction relative to building (0 to 360° scale)
ρ	Air density
σ_x	Standard deviation of quantity represented by the variable x (ex: U, Cp)
ω	Wind angle; 90° is normal to the leading edge
ω_{nom}	Nominal wind direction, determined by the orientation of the model building
ξ	Distance from the vortex core, in the y direction
$\xi_{1/2}$	Half width of the y-direction pressure profile
ζ	Distance from the vortex core, in the z direction

- Subscripts generally denote the position in space at which a quantity is measured, i.e. Cp_o is the pressure coefficient at the point O, which is the centre of the vortex core.
- Overbars indicate time averaged quantities (ex: $\bar{g}$).
- Prime symbols indicate fluctuating quantities. (ex: g')

INTRODUCTION

Windstorm related losses average several billion dollars annually (Bienkiewicz 2000). Of individual weather disasters in the US since 1985, hurricanes have accounted for 13 of 40 individual events causing in excess of one billion dollars in damage, and for 80 billion dollars in damage out of a total of 170 billion (Ross and Lott 2000). While much of the damage in a hurricane is related to flooding either from the storm surge or rainfall, the most damaging of these storms, Hugo ($12.6 billion, 1989) and Andrew ($32.4 billion, 1992) both caused substantial damage to or destruction of homes through severe winds. The Natural Hazards Research and Applications Information Center states that "of all the hazards posed by hurricanes, hurricane-force wind causes the greatest property loss" (Ayscue 1996).

While the incidence of tropical storms worldwide does not appear to be increasing, forecasts for hurricanes in the Atlantic basin indicate that "it is quite possible that the extreme activity since 1995 marks the start of another active period that may last a total of 25-40 years" (Landsea 1999). Given the great cost of wind hazards and the possibility of more numerous severe storms striking the highly populated areas along the East coast of the U.S., several American initiatives have been proposed to study their mitigation. The National Plan for Wind Hazard Mitigation, the Wind Hazard Mitigation Consortium, and the Partnership for Natural Disaster Reduction HomeSaver Project have all been proposed in the past two years (NHC 1999). A bipartisan Wind Hazard

Reduction Caucus has also been created in the U.S. House of Representatives to increase congressional awareness of public safety and economic loss issues associated with hurricanes, thunderstorms, and tornadoes (Bienkiewicz 2000).

One proposed initiative, Project Storm Shelter, was prepared by an international steering committee of wind engineering for the 10th International Conference on Wind Engineering, as part of the United Nations' International Decade for Natural Disaster Reduction. The committee's proposal focused on the vulnerability of housing, and on the lack of reliable pressure data for even simple house shapes (Davenport et al. 1999). David Surry, in a special plenary session on low-rise buildings at this same conference, summarized the current situation in three statements (Surry 1999):

- "We know enough about the wind loads on low buildings now, so that disastrous failures (such as seen during hurricane Andrew) to storms other than severe tornadoes, are much more likely to be due to faults in codes, or construction and inspection practices, than due to lack of basic wind engineering knowledge."
- "The details of the flow and pressures due to the corner vortices remain as an outstanding conundrum, although the practical implications may be limited."
- "The optimization of design for wind loads on low buildings still retains many challenges due to their variety of geometries and surroundings".

Research into mitigation of the effects of tornadoes has focused on saving lives through the development of shelters (FEMA 1999), since it is generally not cost effective to attempt to build residential homes to withstand a tornado. As the above quote from Surry indicates, however, damage due to hurricane winds can be considerably reduced through a better understanding of the pressures induced on the building.

The greatest force on the building is known to be the uplift on the roof, and this is a very common failure mode. More than 17,300 homes in Puerto Rico received temporary roofing following the passage of Hurricane Georges in 1998 (FEMA 1998). Again I quote from the Natural Hazards Research and Applications Information Center report (Ayscue 1996):

> "Roof covering failure was the most widespread type of damage observed after Hugo, according to Manning and Nichols (1991). Roof coverings which were not adequately attached, and corner and eaves regions of roofs were frequently damaged. Smith and McDonald (1991) note that in the Charleston area probably more than 75% of all roofs had at least minimal damage. Once roofs were breached, house interiors were exposed to further damage from water. Roof failures were also the most frequently observed structural failures from Andrew. Richard L. Cook (1991) estimates that over 80% of losses were related to roof failures and associated water damages. In Dade County, Florida, the most common building failure observed was loss of roof cladding (shingles, tiles, etc.). Ninety percent of all homes in Dade County had some degree of roof damage (Doehring et al. 1994)."

The worst suction on both gabled and flat roofs are known to occur beneath the vortices that form in the separated flow along the roof edges (Kanda and Maruta 1993, Kind 1986). For flow normal to a wall, a condition known as "bubble separation" predominates. In this situation, the position of the reattachment varies considerably, and the vortices which form along the roof edge in the separated flow form and are convected away from the edge at irregular intervals. In contrast, for cornering flow, the flow separation on flat or gabled roofs takes the form of stable dual conical vortices.

The nature of these vortices is the subject of the experimental study and flow model development described in this dissertation. Tests have focused on the conical vortices, rather than those that form under bubble separation, because the conical vortices, being more stable, are easier to observe, but the results are equally applicable to the more cylindrical vortices associated with bubble separation. Tests have also been limited to the flat roof case both for simplicity and to allow comparison with a full-scale low-rise building experimental facility constructed at Texas Tech University (TTU) in Lubbock (Levitan and Mehta 1992). Full-scale data from TTU was available for comparison because the work in this dissertation was funded by the National Science Foundation as part of a five-year joint research program between TTU and CSU called the Co-operative Program in Wind Engineering. Some full-scale data is presented in both Chapters 1 and 5.

In wind engineering research, interest in roof corner vortices is keen not only because of their connection to high roof suction but because of several peculiarities observed during pressure measurement:

1) The discrepancy between full-scale and model-scale peak pressures: While the results of scaled model studies and full-scale test provide matching mean pressure coefficients over the whole building, the peak and rms pressure coefficients do not match under the separated flow, where the vortices are located. There, the full-scale rms and peak suctions are higher for the full-scale tests. This is a concern, since the building codes of many countries are based upon scaled-model tests in boundary layer wind tunnels.
2) The quasi-steady theory is often used in building codes to predict peak pressures based upon knowledge of mean pressure coefficients and of the turbulence characteristics of the upstream flow. The quasi-steady theory is generally fairly accurate for most of the building, but does not work well for pressures beneath the separated flow.

3) Taps beneath the vortices have exhibited bi-modal probability distributions. This is not seen anywhere else on the structure.

4) Extreme peak pressures beneath the vortices are better correlated along the length of the vortex than velocity gusts in the upstream flow, or pressures elsewhere on the building.

While item 4 is simply the result of the presence of a coherent flow structure on the building roof (the vortex), the other items in this list have elicited considerable discussion in pressure studies of low-rise buildings. One author has written nearly a dozen papers attributing the discrepancy of item 1 to a failure to adequately simulate small scale turbulence and lateral turbulence intensity in the wind tunnel studies (see, for example, Tieleman et al. 1997).

Tieleman bases his arguments for better simulation of small-scale turbulence on the fact that studies of prisms immersed in turbulent flow have shown that increased turbulence intensity reduces the size of the separation bubble and reduces the minimum mean and rms values of Cp (Li and Melbourne 1995). Similarly, the call for increased lateral turbulence intensity (σ_v/U) is based upon the observation of increased Cp fluctuations on the roofs of buildings downstream from "regions" of complex terrain. These regions produce a greater σ_v/U, regardless of the local roughness near the building (Tieleman 1992).

These attempts to understand how upstream flow conditions could control rooftop surface pressures reveals that the debate over the discrepancies is really subordinate to the question of explaining how the extremely low pressures near the roof edge occur. Cp values below –20 have been measured at TTU. Tieleman writes, "So far no acceptable explanation has been found for the existence and occurrence of these (extremely low pressures)" (Tieleman 1993). Melbourne, who has co-authored several studies examining the effects of turbulence on shear layer separation, has written that

> "Alhough we may still not fully understand the mechanism causing these very low pressures, the boundary conditions for their occurrence is very clear. Simply, if very high freestream turbulence ($\sigma_u/U >> 0.2$) combines with an edge discontinuity the scene can be set for the occurrence of very low pressures under the reattachning shear layer." (Melbourne 1993).

This dissertation examines this mechanism both experimentally and theoretically. Chapter 1 describes the experimental facilities used to examine the vortex, which consist principally of simultaneous flow visualization and pressure measurement system. Chapter 1 also presents basic information about the vortex size, shape, and position, as well as some preliminary results regarding the connection between vortex size and surface pressure in smooth flow.

Chapter 2 offers a simple theoretical explanation for the pressure drop across the vortex core to the roof surface which quantifies the manner in which the flow curvature and flow speed above the vortex combine to determine the surface pressure at the roof. The model suggests how both lateral turbulence and small-scale turbulence can influence surface pressure. Chapter 3 evaluates this model using the experimental configuration developed in Chapter 1. The flow model is shown to explain general mean pressure patterns beneath the vortex, and suggests that the peaks are simply the result of a solid reattachment and high local flow acceleration.

Chapter 4 examines the pressures beneath the vortex, looking closely at the failure of the quasi-steady theory (which turns out to work surprisingly well for cornering winds) and the existence of a bi-modal probability distribution (which can be explained by the quasi-steady theory). Finally, Chapter 5 examines some methods of reducing peak suction beneath near the roof edges in light of the limitations and possibilities suggested by the model presented in Chapter 2.

References

Ayscue, J. K. (1996), *Hurricane Damage to Residential Structures: Risk and Mitigation*, produced by Natural Hazards Research and Applications Information Center, Institute of Behavioral Science, University of Colorado, November, 1996.

Bienkiewicz, B. (2000). "Special Public Policy Symposium, Reducing losses from windstorms held in Washington, DC, November 18-19, 1999", in *The Wind Engineer*, pp. 1-2.

Davenport, A., Goliger, A., Krishna, P., Lee, B., Niemann, H.-J., and Walker, G. (1999), *Project Storm Shelter: Outline*, produced for the International Association of Wind Engineering, June 1999.

Doehring, F., W.Duedall, I., and Williams., J. M. (1994), *Florida Hurricanes and Tropical Storms 1871-1993: An Historical Survey*, produced by Division of Marine and Environmental Systems, Florida Institute of Technology.

FEMA (1998), *Hurricane Georges Surpasses Hurricane Andrew in Total Number of Disaster Applicant Registrations*, produced by Federal Emergency Management Agency, available at www.fema.gov/hu98/d1247n20.htm since October 19, 1998

FEMA (1999), *Taking Shelter From the Storm: Building a Safe Room Inside Your House*, produced by Federal Emergency Management Agency, available at http://www.fema.gov/mit/tsfs02.htm since August 1999

Kanda, M., and Maruta, E. (1993), "Characteristics of fluctuating wind pressure on long low-rise buildings with fable roofs", *J. Wind Eng Ind. Aerodyn.*, 50(1-3), pp 173-182.

Kind, R. J. (1986), "Worst suctions near edges of flat rooftops on low-rise buildings", *J. Wind Eng Ind. Aerodyn.*, 25, pp 31-47.

Landsea, C. W. (1999), *FAQ : hurricanes, typhoons, and tropical cyclones : Part G : Tropical Cyclone Climatology*, produced by the Hurricane Research Division of the Atlantic Oceanographic and Meteorological Laboratory, and available at http://www.aoml.noaa.gov/hrd/tcfaq/tcfaqG.html#G4 since August 12, 1999

Levitan, M. L., and Mehta, K. C. (1992), "Texas Tech field experiments for wind loads part 1: building and pressure measuring system", *J. Wind Eng Ind. Aerodyn.*, 41-44, 1565-1576.

Li, Q. S., and Melbourne, W. H. (1995), "An experimental investigation of the effects of freee-stream turbulence on streamwise surface pressures in separated and reattaching flows", *J. Wind eng. Ind Aerodyn.*, 54/55, pp 313-323.

Manning, B. R., and Nichols, G. G. "Hugo Lessons Learned" in: *Hurricane Hugo One Year Later*, edited by B. A. Sill and P. R. Sparks. New York: American Society of Civil Engineers, 1991.

Melbourne, W. H. (1993), "Turbulence and the Leading Edge Phenomena", *J. Wind Eng Ind. Aerodyn.*, 49, pp 45-64.

NHC (1999), *Disaster Research Newsletter*, v 283, produced by Natural Hazards Center at the University of Colorado, Boulder, available at http://www.colorado.edu/hazards/dr/dr283.html since February 22, 1999

Richard L. Cook, J. "Lessons Learned by a Roof Consultant" in: *Hurricane Hugo One Year Later*, edited by B. A. Sill and P. R. Sparks. New York: American Society of Civil Engineers, 1991.

Ross, T., and Lott, N. (2000), *Billion Dollar U.S. Weather Disasters 1980-1999*, produced by National Climatic Data Center, available at http://www.ncdc.noaa.gov/ol/reports/billionz.html since January 01, 2000

Smith, T. L., and McDonald, J. R. "Roof Wind Damage Mitigation: Lessons from Hugo" in: *Hurricane Hugo One Year Later*, edited by B. A. Sill and P. R. Sparks. New York: American Society of Civil Engineers, 1991.

Surry, D. (1999), "Wind loads on low-rise buildings: Past, present and future", *Wind Engineering into the 21st Century*, proceedings of the 10th International Conference on Wind Engineering, v 1, Copenhagen, Denmark,21-24 June 1999.

Tieleman, H. W. (1992), "Problems associated with flow modelling procedures for low-rise structures", *J. Wind Eng Ind. Aerodyn.*, 41-44, pp. 923-934.

Tieleman, H. W. (1993), "Wind loads on Roofs of low rise structures: buffeting of interaction", Proceedings of the Symposium on Hurricanes, Dec 1-3 1993.

Tieleman, H. W., Reinhold, T. A., and Hajj, M. R. (1997), "Importance of turbulence for the prediction of surface pressures on low-rise structures", *J. Wind Eng Ind. Aerodyn.*, 69-71, pp. 519-528.

CHAPTER 1: FLOW VISUALIZATION ON FLAT ROOFS WITH SIMULTANEOUS SURFACE PRESSURE MEASUREMENT

Most of the material in Chapter 1 is also available in the Jan. 2000 Journal of Wind Engineering and Industrial Aerodynamics (Vol 84, pgs 65-85)

1.1 Introduction:

Many studies have shown that the worst mean and peak suctions on flat building roofs occur for cornering or oblique wind angles (see, for example, Lin *et al.*, 1995). At such angles, conical or delta wing vortices form along the roof edges (See Figure 1.1). Interest in the behaviour of these vortices has been heightened by the unexpected discrepancy between the peak and rms surface pressures measured under these vortices for full scale tests and those measured for model scale tests (see, for example, Tieleman *et al.*, 1996), though recent refinements to the wind tunnel boundary layer simulation appear to have reduced or eliminated this discrepancy (Ham and Bienkiewicz 1998).

In 1994, Tieleman wrote that "no comprehensive results are available for the variations of surface pressures on top surfaces of prisms, immersed in turbulent boundary layers, with the nature of the incident flow (mean flow profile, turbulence intensity and turbulence scales)", adding that discrepancies between extreme pressures measured in the separated flow zones of full scale and model scale building roofs were "attributed to the inadequate simulation of lateral velocity fluctuation." (Tieleman *et al.*, 1994) The paper went on to show that higher model scale peak suctions could be induced by placing small spires immediately upstream to increase the lateral turbulence intensity.

Lateral turbulence intensity had also been cited by Letchford and Mehta (1993) as playing an important role in pressure fluctuations for quartering winds. This conclusion was based upon the similarity between the shape of pressure eigenvectors under the vortices and the pattern of $\mathrm{d}C_{\bar{p}}/\mathrm{d}\theta$ values, where θ is the wind direction. This derivative, an indication of surface pressure dependence upon mean lateral wind direction, is linked to surface pressure fluctuations in quasi-steady theory by a term which couples this derivative with lateral turbulence intensity (Letchford and Marwood 1997). Note, however, that this later study concluded that the quasi-steady theory fails fundamentally to deal with flow distortion due to building generated turbulence.

Since 1994, several studies have addressed the link between incident flow and surface pressures, and in particular the issue of the effects of lateral turbulence. Letchford and Marwood (1997) compared simultaneous upstream laser doppler anemometer (LDA) measurements of *u-v-w* velocity fluctuations and model surface pressures. These flow velocity measurements were taken quite close to the building, at distances upstream of 50% and 10% of the building height. Conditional sampling was used to isolate the effects of instantaneous wind direction on C_p values. The conclusion was that extremes in pressures were associated with large excursions in lateral velocity, specifically excursions toward a flow normal to the wall.

This agrees qualitatively with the full scale work of Zhao (1997) for normal flows, who also compared roof pressures with wind flow and direction immediately upstream of the roof, and concluded that the local, non-conventional C_p (where pressures are normalized by the local wind speed to isolate wind direction effects) assumes peak suction values during fast and large fluctuations in lateral wind direction.

Kawai and Nishimura (1996) have also simultaneously measured roof suctions and upstream velocities for a flat roof low rise model building. They concluded, based on the correlation of suction fluctuation over the entire roof, that the dual conical vortices sway in unison. They also saw a correlation between suction fluctuation in the re-attachment zone and approaching low frequency lateral turbulence, leading them to conclude that the lateral component of approaching turbulence amplifies the sway of the vortex axes, causing increases in low frequency suction fluctuations.

While these studies have made progress in linking flow characteristics to surface pressures, Marwood and Wood (1997) wrote that "the mechanism linking vortex structure and surface pressure is little understood." This comment prefaced a report on a study in which surface pressures and flow velocities at a point within the vortex core were simultaneously sampled. Conditional analysis of the velocities at various points in the separated flow associated with peak and minimum suctions revealed some of the average separated flow characteristics associated with the largest and smallest suctions. For example, Figure 1.2 (adapted from their study) shows that the higher suctions were generally associated with larger vortices for turbulent flow.

The experimental work described in this Chapter continues, in the same vein as the previous two references, to pursue a link between vortex behaviour and surface pressures. It is hoped that once this link is better understood, the flow characteristics controlling vortex behaviour can be more directly associated with roof top surface pressure events, and the nature of the breakdown in the quasi-steady theory's link between flow parameters (such as lateral turbulence intensity) and surface pressures can be ascertained.

This chapter discusses the results of visualization studies that have been performed at both TTU and CSU to determine the position and size of the vortex as a function of incident wind characteristics, especially wind direction. In addition, surface pressures were simultaneously measured during the wind-tunnel visualization, providing a clear link between instantaneous surface pressures and vortex behaviour.

1.2 Experimental procedures

1.2.1 Preliminary flow visualization

Initial wind tunnel tests were performed for smooth flow in the CSU Environmental Wind Tunnel (EWT), which is a non-recirculating tunnel with a 3.7 m x 2.1 m cross section. Several different cuboidal models, ranging from 450 mm to 1.2 m on any given side, were mounted above the tunnel floor boundary layer. A laser light sheet was used to illuminate a plane within the vortex core region, and images were recorded on an SVHS camera. The laser was a Coherent Innova 70-5 Argon ion water-cooled laser, and it was operated in multi-line mode for these tests. It had a nominal maximum output power of 5 Watts, but was generally run at or below 1 Watt for these tests. The laser beam was focused and spread into a sheet by lenses mounted on the tunnel ceiling. Glycerin smoke was introduced through holes near the leading corner (apex) of a model's roof.

The light sheet was positioned at various distances from the apex, usually normal to the leading edge. It was found that the mean core position follows a straight line, beginning at the apex and running along the leading edge. The position of this core-line, or ray, can be defined by a vortex core angle ($\phi_{\bar{c}}$) and a height ratio (h/x), as shown in Figure 1.3. It should be noted that at $x = 0$, the core has an initial finite displacement above the apex of around $h_0 = 2$ mm (Figure 1.4). Since the core rises very slowly ($\Delta h/\Delta x$ = 7 mm per 100 mm for $\omega = 45°$), this will distort h/x values by over 10% for $x<300$ mm. This is important for comparing the normalized results of many vortex visualization studies, which are often carried out on small (100 mm to 200 mm long) models. Where possible, this study normalizes the vortex core height using $(h-h_0)/x$. Figure 1.3 also illustrates the definition of the wind angle (ω) used in this study. Winds normal to the leading edge wall are defined as $\omega = 90°$. This differs from some other studies, which define normal winds as 0°.

Vortex position sensitivity tests were carried out for a range of wind speeds. The mean core position was shown to be invariant for speeds from 3 m/s to 10 m/s. For speeds below 3 m/s, $\phi_{\bar{c}}$ increased by 10 to 20%.

1.2.2 Digital imaging

The images from the SVHS video recordings proved difficult to quantify, as even in smooth flow the core would move considerably and the intensity of the smoke would fluctuate. The result was that segments of the visualization would be unusable. By acquiring images digitally and enhancing the contrast as needed, the vortex core position and size could be traced for entire sequences of consecutive images.

The digital recording system makes use of a Pulnix TM-7CN CCD array camera which provides one 640×480 pixel grey scale image every 60th of a second. The camera has a variable shutter speed, providing exposure times ranging from a 60th of a second to a 10,000th of a second. The shutter speed was generally set at 125th of a second for these tests, so that the image effectively provides an average of the vortex position over this period of time. At a shutter speed of 60 Hz, the core's location was sometimes less discernible as core movement (changes in ϕ_c and h) would blur the image during the exposure time. At speeds above a 125th, synchronizing the images and the pressure profiles becomes difficult given that both the initial trigger synchronization between the image and pressure sequences, and the variation in the delays between different pressure tap signals, can only be estimated to within a 500th of a second. (These issues are currently being addressed. See sections 1.2.3 and 1.2.4 below.) Also, at these higher speeds, the intensity of the reflected light was often inadequate, though tests showed that this could be remedied through the use of titanium dioxide smoke and increased laser power to the light sheet.

The camera's 60 Hz video signal was digitized in a Pentium PC using an Imaging Technology Inc. MVC IC Image capture board. Compressed image sequences of up to 6 seconds could be recorded if the computer's entire 64 MB of RAM were dedicated to image acquisition. Sequences of 4 seconds were generally used, to leave some memory for image processing. Real time image acquisition and processing, as well as batch image file processing, were performed using ITI's Itex-IC c-language libraries. Interactive post processing of the image sequences was performed using the National Institute of Health's free NIH Image program for the Macintosh.

1.2.3 Pressure Measurement

The experiment was moved to the CSU Industrial wind tunnel (IWT). The IWT test section measures 1.8 m × 1.8 m, and test were run at tunnels speeds between 8 m/s and 12 m/s. Initial pressure tests were performed using a 450 mm Plexiglas cube, with a dozen taps located beneath the vortex core under the separated flow (ϕ between 10° and 18°, and values of x ranging from 50 mm to 200 m). These tests confirmed that there is a good correlation of suction fluctuations along this entire surface beneath the vortex, as reported elsewhere (Kawai and Nishimura 1996), thus indicating that any value of x within the range tested could be used for the pressure/visualization plane. Correlation coefficients between all taps were generally above 0.8, and increased to above .95 when the data was low-pass filtered at 10 Hz. Cross coherence functions remained above 0.5 only for frequencies below 20-30 Hz, confirming that the correlation was due to lower frequency phenomena and indicating that presence of such phenomena could be observed at the 60 Hz camera frame rate. A sample time series shown in Figure 1.5 illustrates one such phenomenon commonly seen in the smooth flow tests: low suction excursions ($|C_p|$ decreases) lasting around one or two seconds, and recurring at two to ten second intervals. It will be shown that these excursions can be explained by variations in the vortex size.

A microphone placed in the tunnel revealed that sound peaks at harmonics of 250 Hz were not being adequately damped out by the restrictor tubes. Since the camera is limited to a 60 Hz data rate, and the time series indicated that the presence of lower frequency phenomena of interest, it was decided to use analog filters to low pass all of the pressure signals at 100 Hz. Three different kinds of filters were used, and each type introduced a signal delay which was measured for a range of sine wave input frequencies. The Krohn Hite filters (models 3323 and 3202) introduced delays of 2 ms at all cutoff frequencies, while the Wavetek model 852's delays increased as the cutoff was reduced. At 100 Hz, the Wavetek's delay was 9 ms. This discrepancy in the delays between taps can pose a problem for the correlation of pressure patterns and vortex image. To counter this, longer restrictor tubes were used for those taps attached to Krohn Hite filters, since the longer tubes also introduce a greater signal delay. All restrictor tubes were designed and tested to provide a linear phase shift out to 200 Hz, and a gain (Gxy/Gx) of 1.00 ± 0.01 out to 100Hz. However, the tube length could not be increased enough to completely compensate for the filter delay discrepancy without undue signal distortion. The net difference in signal delay between any two channels was kept under 1/3rd of the image sample rate, or 5 ms. These delay differences were both predicted mathematically and measured experimentally to within 2 ms, so they could be partially accounted for during post processing.

It is shown above that the average pressure pattern and low frequency (<30 Hz) time series behaviour under the vortex is essentially the same for any value of x close enough to the apex, so that the pressure taps and imaging plane could be located far enough from the apex to allow 1.6 mm (1/16th inch) taps to be easily drilled near the leading edge. The vertical plane was also selected far enough from the apex to provide a large enough vortex so that its behaviour could be readily observed from outside the tunnel without the help of magnifying lenses, while being close enough to the apex to permit a strong pressure signal to be measured (the pressure drops off exponentially with distance from the apex (Lin *et al.*, 1995)). A plane normal to the leading edge at $x = 150$ mm was chosen. The row of taps was installed in a cubic aluminum model measuring 450 mm on a side. Eleven taps were drilled at 2.5° intervals, from $\phi = 5°$ to $\phi = 30°$. A 12th tap was installed at $x = 5$ cm and $\phi = 25°$ for comparison. All taps were connected to individual Honeywell Micro Switch transducers mounted inside the model. Pressure data was recorded at 600 Hz.

1.2.4 Simultaneous Pressure Measurement and Flow Visualization

A single external TTL signal was used to trigger both the image sequence acquisition and the pressure time series acquisition. As a result of the camera's internal clock, the start of the image sequence was generally delayed by 8ms from the start of the pressure time series, though the exact delay could only be estimated to within 2ms for the best of image sequences. This problem would later be solved through the use of a precisely timed LED light sequence, which would also be triggered by the TTL signal (see Section 3.2.1).

1.2.5 Upstream flow conditions

The tests were initially conducted in smooth flow, with no upstream trips, roughness, or spires. The turbulence intensity was measured at 4% at roof height using an LDA probe. These tests have been labeled "smooth flow" in this study.

Some turbulent tests were undertaken, though no atmospheric boundary layer (ABL) simulation was attempted because of the large size of the cubes. Turbulence was generated using individual trips and spires. Model scale experimental results from this study which are labeled "turbulent" (Figures 1.7, 1.8b, 1.8c, 1.11a, 1.12-1.14, 1.15a) were taken from runs using a single 200mm high trip spanning the width of the tunnel, placed 4m upstream of the model. Rooftop turbulence intensity was 15-20% in this case. The results of tests conducted in a full ABL simulation are reported in Chapters 3, 4 and 5.

1.2.6. Full scale visualization

Three different methods have been successfully employed at TTU for flow visualization at the full-scale test site (Sarkar *et al.*, 1997). These methods are the tuft-grid method, the smoke injection technique, and the airfoil-grid method. In all cases, visualizations were more effective at night when floodlights were used for illumination. An 8-mm video camera was used to record the flow in each method. The tuft grid method was employed for the visualization of the corner vortex flow for this chapter.

The airfoil-grid makes use of several light-weight airfoils made out of Balsa wood and paper, which are fixed to a metal grid in such a way that they are free to rotate in the plane of the grid. Reflective tape on the sides of the airfoils aids nocturnal visualization. In the tuft grid method, a 20 ft × 7 ft. (6 m × 2 m) metal frame with a 6-in. (150mm) grid was used. Coloured yarn segments were tied to the nodes of this grid. For tests close to the apex, a smaller tuff grid (7 ft. × 3.5 ft. or 2.1m × 1.1m) with a finer mesh size (4 in. × 4 in., or 100 mm × 100 mm) was used.

Wind speed and direction data was initially measured at the meteorological tower, located about 50 m from the WERFL building. Later tests made use of a sonic anemometer fixed 1.6m above the roof apex. This facility is described in detail by Zhao (1997).

1.3. Results

Several authors have presented rooftop pressures, measured along rays from the apex in the vortex region (for example, $\phi = 14°$ (Lin *et al.*, 1995) and $\phi = 16°$ (Marwood and Wood 1997)) in full ABL simulations. These rays were generally chosen to correspond with the expected location of the ray of maximum suction or the ray of vortex core position. Potential flow theory indicates that these two rays should coincide, since a free point vortex over an infinite plane produces a symmetrical bell-shaped suction curve on the surface of the plane, with the maximum directly beneath the vortex center (Greenwell and Wood 1992, Kawai and Nishimura 1996, Marwood 1996). An aerospace literature search performed illustrates that this is generally the case for swept delta wings (Greenwell and Wood 1992), and the coincidence of $\phi_{\bar{C}}$ and $\phi_{\bar{p}}$ is reported for roof top vortices by Kawai (1997), where $\phi_{\bar{p}}$ is defined as in Figure 1.6 (taken from Sun, 1993). Similarly, the angles $\phi_{\check{p}}$ and ϕ_{σ_p} can be defined from their respective C_p contour plots based on the angle ϕ for which $C_{\check{p}}$ or C_{σ_p} is a maximum for any value of x.

The potential flow theory surface pressure prediction is given by

$$\Delta P = \frac{\Delta P_{\max}}{\left((\xi / z_m)^2 + 1\right)^2} \tag{1.1}$$

where z_m is the theoretical vortex height above the surface, ξ is the distance from the core along the surface and normal to the core axis of rotation, and $\Delta P_{\max}$ is a function of the circulation and z_m. This theory gives the vortex height as

$$z_m = 1.55\, y_{½} \tag{1.2}$$

where $y_{½}$ is the half width of the suction peak. The development of Eqs. (1.1) and (1.2) is discussed in more detail in Chapter 2. Eq. (1.2) has been found to hold true for aerospace data, that is for vortices above highly swept wings (included angles less than 40°) at high angles of attack (Greenwell and Wood 1992).

However, Eq. (1.2) is not valid for rooftop vortices, which are more oblong (have a lower h/y_{core} ratio). This is perhaps not too surprising, given the substantial differences between these two flows, notably in the slower axial velocities seen on roofs (Marwood 1996). Since the circulation is generally unknown (though it has been experimentally measured for delta wings (Visser and Nelson 1993)), Eq. (1.1) becomes merely a curve fitting tool for the surface pressure profile data, where $\Delta P_{\max}$ is either measured or determined from empirical formulae like those reported by Lin *et al.*, (1995), and z_m is determined from Eq. (1.2).

This curve is fit to a sample average pressure profile in Figure 1.7, where $\Delta P_{\max}$ and r have been corrected to account for the $x = 150$ mm plane not being perpendicular to the vortex core's ray (in this case, $\phi_{\overline{c}} = 12°$). Note that the data is asymmetric, with pressures exceeding the curve fit values for $\phi < \phi_{\overline{c}}$. This is consistently true for all tests in this study, confirming trends seen elsewhere (Kawai and Nishimura 1996). Figure 1.7 also shows how the potential flow model under-predicts the half-width of the pressure profile if the actual vortex core height is used for z_m.

The profiles for C_{σ_p} and $C_p^{\vee}$ are similarly asymmetric in both turbulent and smooth flow (see Figure 1.8). Nonetheless, all of the profiles exhibit clear peaks, which correspond to the values of ϕ_{σ_p}, $\phi_p^{\vee}$, and $\phi_{\overline{p}}$. Several trends are evident when these angles are compared:

i. While $\phi_{\overline{p}}$ is slightly lower and $\phi_p^{\vee}$ slightly higher than $\phi_{\overline{c}}$, these angles of highest suction clearly follow the vortex core position closely.

ii. ϕ_{σ_p} is greater than $\phi_{\overline{c}}$ for turbulent flow, while being lower for smooth flow.

iii. Turbulence reduces $\phi_{\overline{c}}$ by around 30%, though the size of this reduction depends on the nature of the turbulence. This agrees with previous research which gives $\phi_{\overline{c}}$

= 10° for turbulent flow and $\phi_{\bar{c}} = 13°$ for smooth flow when $\omega = 45°$ (Kawai and Nishimura 1996).

These trends hold true for wind angles from 30° to 70°, as shown in Figure 1.9. The ratios between the rays are essentially preserved: $\phi_{\bar{c}} / \phi_{\bar{p}}$ stays nearly constant, while ϕ_{σ_p} remains greater than these two for all values of ω. $\phi_p^{\vee}$ is the exception, remaining in a narrow band between 10° and 16°. This could indicate that for low wind angles, peak suctions are associated with larger than average vortices, while at higher wind angles, peak suctions occur for average or below average sized vortices.

The curves for $\phi_{\bar{p}}$, ϕ_{σ_p}, and $\phi_p^{\vee}$ are adapted from the result of Sun (1993), and are all for simulated ABL flow over a 1:50 scale model of the WERFL building. The $\phi_{\bar{c}}$ curve is based on the full scale data presented in Figure 1.10b. Figure 1.10a shows the vortex core height dependence on ω. The model scale data presented is for smooth flow, illustrating again that $\phi_{\bar{c}}$ decreases in turbulent flow, though h shows little change.

There is also more scatter in the TTU data. This is explained in part by the fact that the TTU data points are single observations, while the model scale data points involve averaged images or averaged flow velocities. The vortex grows and shrinks considerably during a short span of time, as seen in Figure 1.11a, which shows all 240 vortex core position observation during a 4 second turbulent flow sequence. The range of motion is decreased for smooth flow (see Figure 1.11b), but even so the core is almost equally likely to be found anywhere in the range from $\phi = 20°$ to $26°$ for $\omega = 55°$.

It is this rapid motion which accounts for ϕ_{σ_p} being larger than $\phi_{\bar{c}}$ in turbulent flow. We see from Figure 1.12 that a typical instantaneous pressure profile generally exhibits the same characteristics as the average pressure profile: a gentle loss of suction between the peak and the wall, with a more rapid loss of suction towards the center of the roof. Comparison with the image taken simultaneously with this pressure profile shows that this transient pressure peak is located directly beneath the vortex core (Figure 1.13). Similar comparisons showed that the peak suction *always* closely follows the moving core. Since the core moves back and forth in ϕ or y, pressure taps beneath the rapid loss of suction inboard of the vortex core ($12.5° < \phi < 20°$ for turbulent flow and $\omega = 45°$) see the greatest fluctuations in suction, as the core approaches and recedes from them, sweeping this high pressure gradient flow over them. For smooth flow, however, the motion of the vortex is much slower, and ϕ_{σ_p} is not associated with the C_p gradient in the zone between the core and the re-attachment.

This motion might also account for the discrepancy between $\phi_{\bar{c}}$ and $\phi_{\bar{p}}$. As the vortex moves, regions between the core and the wall ($\phi < \phi_{\bar{c}}$) would generally see higher suctions than equidistant regions on the other side of the peak suction, due to the asymmetry of the profile. As a result, the highest mean suction would appear at a point closer to the roof edge than the average vortex position.

The motion also tends to produce an average pressure profile with smoother peaks and a wider half width than the individual profiles. However, even the instantaneous profiles with the steepest loss of suction for $\phi > 12.5°$ have a considerably larger half width than that predicted by potential flow theory, and the average of profiles with Cp_{max} above tap#4 (Figure 1.12) shows that the average pressure profile is a reasonably accurate reflection of the typical shape of the instantaneous profiles.

It is important to note that the discussion of typical or averaged characteristics is often too reductive. It has generally proven more instructive to individually examine the image and pressure sequences themselves. It was found that an immediate visual correlation could usually be made between the vortex position and the concurrently recorded surface pressures. To emphasize this connection, the pressure profiles which were measured while an image was being captured have been digitally superimposed on that image. Figure 1.13 describes a typical result. Figure 1.14 illustrates several flow phenomena, including large suction peaks for both small and large vortices (1.14a and 1.14b), widely varying profiles for similarly sized vortices (1.14c and 1.14d), and low suction events where the vortex has essentially disappeared (1.14f). These loss-of-vortex or washout events are only seen for turbulent flow, and are commonly followed by some of the larger suction excursions as the vortex reforms.

As might be anticipated from the images in Figure 1.14, no connection could be established in turbulent flow between suction strength and vortex size except for taps in the range $1.5\bar{\phi_c} < \phi < 2\bar{\phi_c}$. These taps are never beneath the core, and experience greater suctions for larger vortices simply because the core moves towards them as the vortex gets bigger. The actual magnitude of the suction beneath the core was independent of the core's height above the surface, as is evident from Figure 1.15a, which shows core height vs. suction at a tap located beneath the mean $\bar{\phi_c}$ position. Only samples where the core was within $\Delta y = 4$ mm (i.e. ±1.5°) of this tap are shown. Also shown is the least squares linear curve fit to this data. The null hypothesis that the slope is zero cannot be rejected with even a 60% level of certainty, and this conclusion does not change for any value of Δy.

Figure 1.15b shows that the situation for smooth flow is quite different, as the suction clearly increases linearly as the vortex gets smaller. In this case, vortex size is indicated by the size of the entire separation bubble. By introducing smoke at the apex of the model, the entire separation zone containing the vortex was clouded. The image could then be thresholded so that the separation zone was completely white, and image integration then gives a value for the vortex area.

Figure 1.16 is a time series showing how the pressure at a tap near the mean core position follows the vortex size. Correlation coefficients between the vortex size and the pressures at the highest suction taps were between 0.90 and 0.95. The pressure time series at a tap further from the leading edge is also shown. As with the turbulent flow, such taps have a negative correlation, since suction will decrease far from the leading edge if the core gets small enough (see for example Fig. 1.16 from frame 150 to frame 250). The loss of suction incidents seen in Fig. 1.5, and in Fig. 1.16 in frames 30 through 110, are associated with the largest vortices.

1.4 Concluding comments

A facility has been successfully developed to enable the comparison of simultaneously recorded images of a rooftop corner vortex and the pressures beneath this vortex. The initial results confirm that the peak suction lies beneath the vortex core, and moves with the vortex. For smooth flow, the magnitude of this suction peak increases linearly with decreasing vortex size.

Changes in vortex size and position have been characterized. The vortex is found to grow larger and move away from the roof edge as the wind angle increases. Turbulence moves the mean vortex core position closer to the leading edge. Considerable motion about the mean position is seen for both smooth and turbulent flow. The combined effects of this motion and the consistent asymmetry of the pressure profile beneath the vortex accounts for the nature of the $C\sigma_p$ and $C_{\overline{p}}$ roof surface pressure patterns.

1.5 References

Cochran, L. S. (1992), *Wind tunnel modelling of low-rise structures*, Ph. D., Civil Engineering, Colorado State University, Fort Collins, Co.

Greenwell, D. I., and Wood, N. J. (1992), "Determination of vortex location on delta wings from surface pressure measurements", *AIAA Journal*, **30**(11), 2736-2739.

Ham, H. J., and Bienkiewicz, B. (1998), "Wind tunnel simulation of TTU flow and building roof pressure", *J. Wind Eng. Ind. Aerodyn.*, **77 & 78**, 119-133.

Kawai, H. (1997), "Structure of conical vortices related with suction fluctuation on a flat roof in oblique smooth and turbulent flows", *J. Wind Eng. Ind. Aerodyn.*, **69-71**, 579-588.

Kawai, H., and Nishimura, G. (1996), "Characteristics of fluctuating suction and conical vortices on a flat roof in oblique flow", *J. Wind Eng. Ind. Aerodyn*, **60**, 211-225.

Letchford, C. W., and Marwood, R. (1997), "On the influence of v & w component turbulence on roof pressures beneath conical vortices", *J. Wind Eng. Ind. Aerodyn.*, **69-71**, 567-577.

Letchford, C. W., and Mehta, K. C. (1993), "The distribution and correlation of fluctuating pressures on the Texas Tech building", *J. Wind Eng. Ind. Aerodyn.*, **50**, 225-234.

Lin, J.-X., Surry, D., and Tieleman, H. W. (1995), "The distribution of pressure near roof corners of flat roof buildings", *J. Wind Eng. Ind. Aerodyn.*, **56**, 235-265.

Marwood, R. (1996), *An investigation of conical roof edge vortices*, Ph.D. thesis, Lincoln College, University of Oxford, Oxford, UK.

Marwood, R., and Wood, C. J. (1997), "Conical vortex movement and its effect on roof pressures", *J. Wind Eng. Ind. Aerodyn.*, **69-71**, 589-595.

Sarkar, P. P., Zhao, Z., and Mehta, K. C. (1997), "Flow visualization and measurement on the roof of the Texas Tech Building", *J. Wind Eng. Ind. Aerodyn.*, **69-71**, 597-606.

Sun, Y. (1993), *Wind loading on loose-laid roofing paver systems*, Ph. D. thesis, Department of Civil Engineering, University of Colorado, Fort Collins.

Tieleman, H. W., Surry, D., and Lin, J.-X. (1994), "Characteristics of mean and fluctuating pressure coefficients under corner (delta wing) vortices", *J. Wind Eng. Ind. Aerodyn,* **42**, 263-275.

Tieleman, H. W., Surry, D., and Mehta, K. C. (1996), "Full/model scale comparison of surface pressured on the Texas Tech experimental building", *J. Wind Eng. Ind. Aerodyn.*, **61**, 1-23.

Visser, K. D., and Nelson, R. C. (1993), "Measurements of Circulation and Vorticity in the Leading-Edge Vortex of a Delta Wing", *AIAA Journal*, **31**(1), 104-111.

Zhao, Z. (1997), *Wind flow characteristics and their effects on low-rise buildings*, Ph.D. dissertation, Civil Engineering, Texas Tech University, Lubbock, Texas.

1.6 Figures

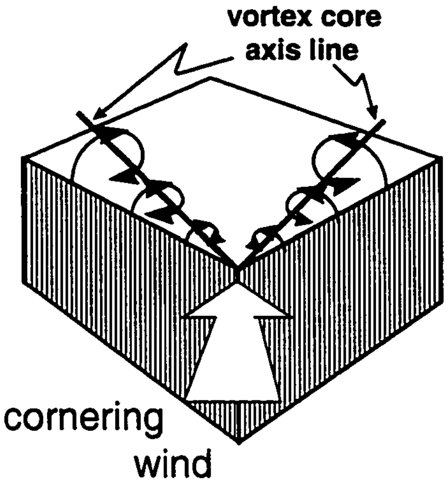

Figure 1.1: Conical "delta-wing" corner vortices

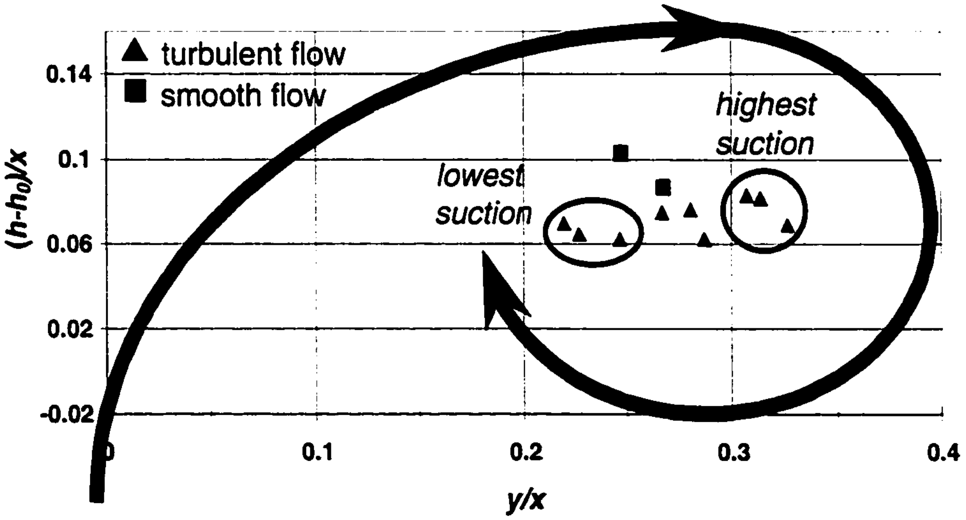

Figure 1.2: Suction vs. core position (adapted from Ref. [9])

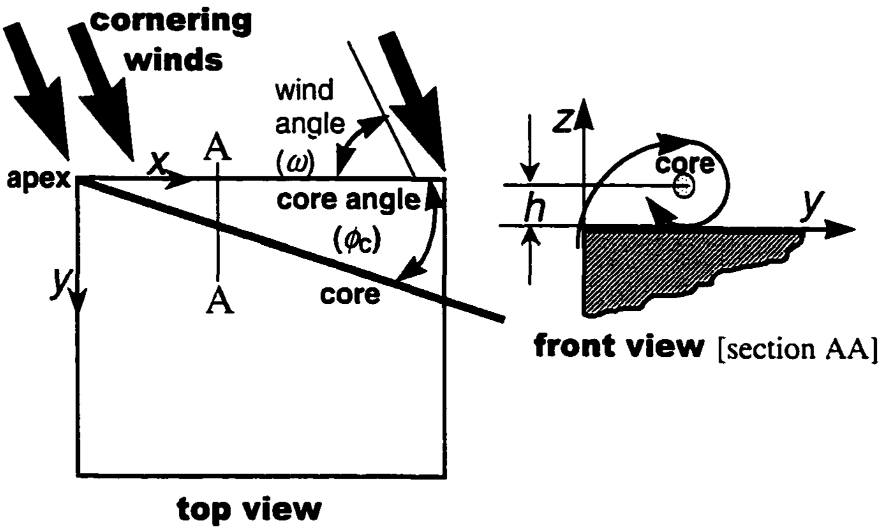

Figure 1.3: Vortex position nomenclature

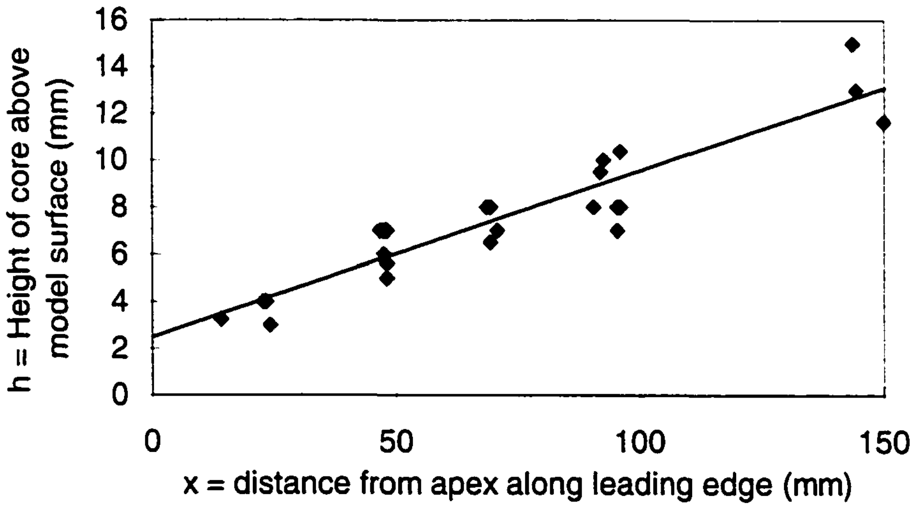

Figure 1.4: Finite displacement of vortex core above apex (Based upon data from CSU and References 9, 11, and 12)

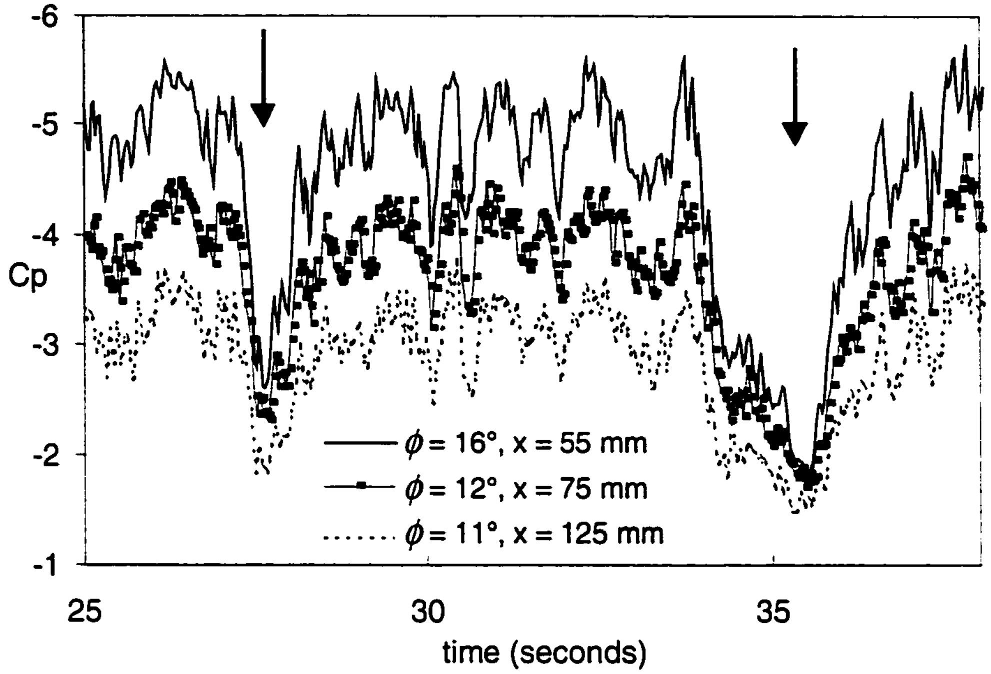

Figure 1.5: Pressure time series excerpt showing two low suction excursions. The data is for a 450 mm surface mounted cube in 10 m/s smooth flow with $\omega = 55°$. Tap positions are given in the legend.

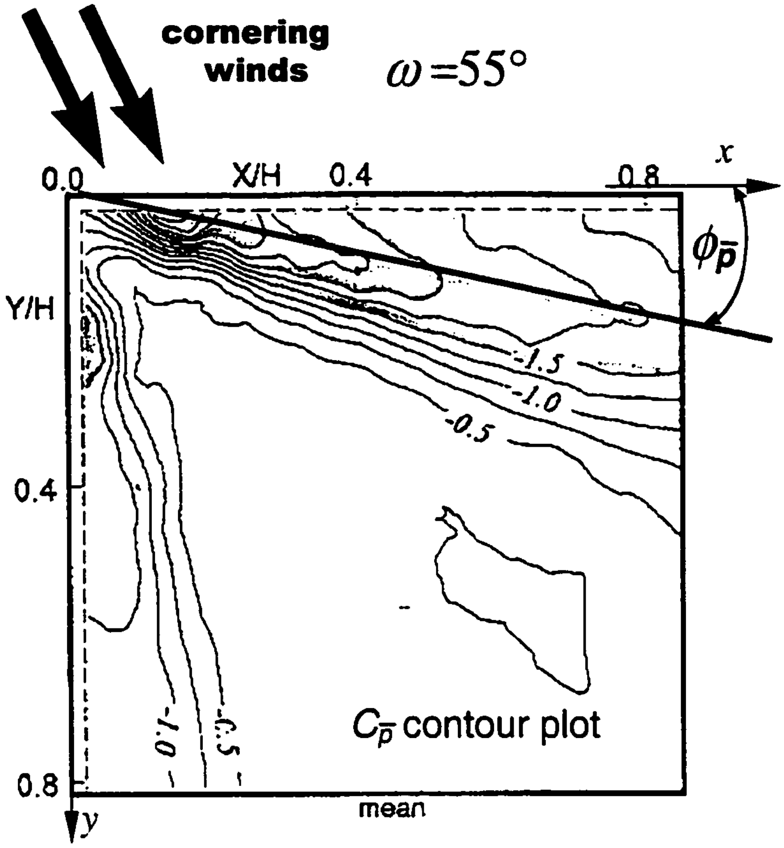

Figure 1.6: Angle of maximum mean C_p

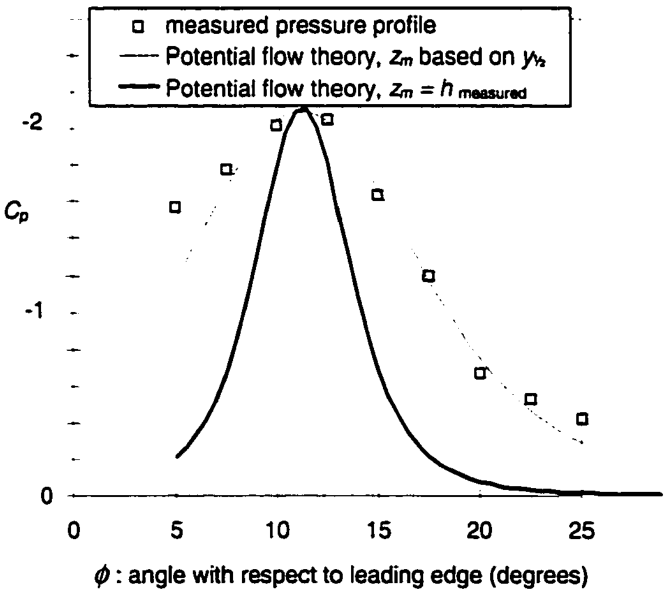

Figure 1.7: Pressure profiles, $\omega = 45°$

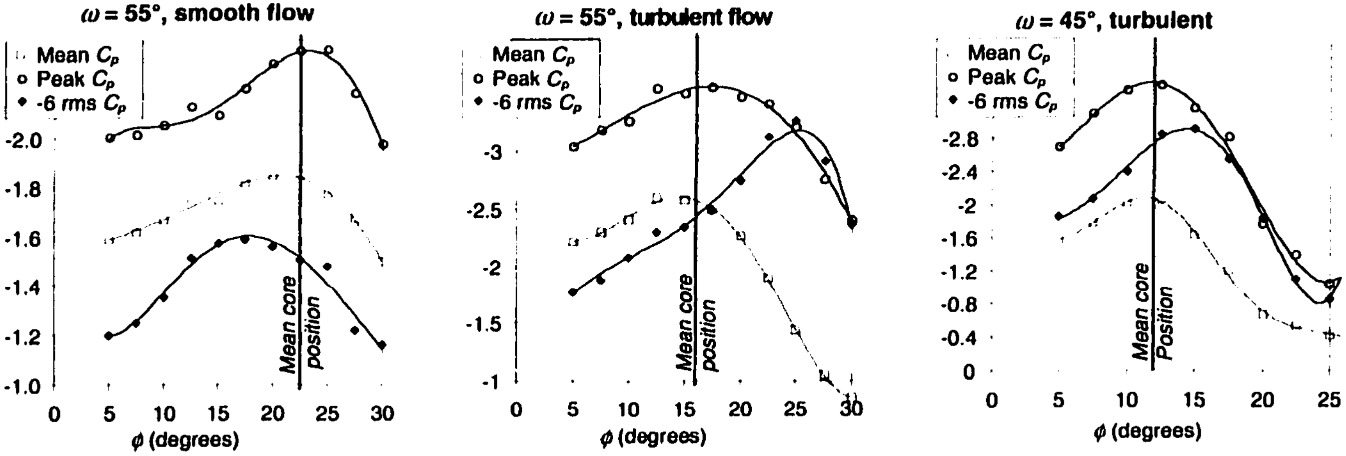

$\phi_{\bar{p}} = 21°$	$\phi_{\bar{p}} = 15°$	$\phi_{\bar{p}} = 11.3°$
$\phi_{\check{p}} = 23.5°$	$\phi_{\check{p}} = 17.5°$	$\phi_{\check{p}} = 11.8°$
$\phi_{\sigma_p} = 18°$	$\phi_{\sigma_p} = 25°$	$\phi_{\sigma_p} = 14.4°$
$\phi_{\bar{c}} = 22.5°$	$\phi_{\bar{c}} = 16°$	$\phi_{\bar{c}} = 12.0°$

Figure 1.8: Pressure profiles under various flow conditions, showing relative location of ϕ values.

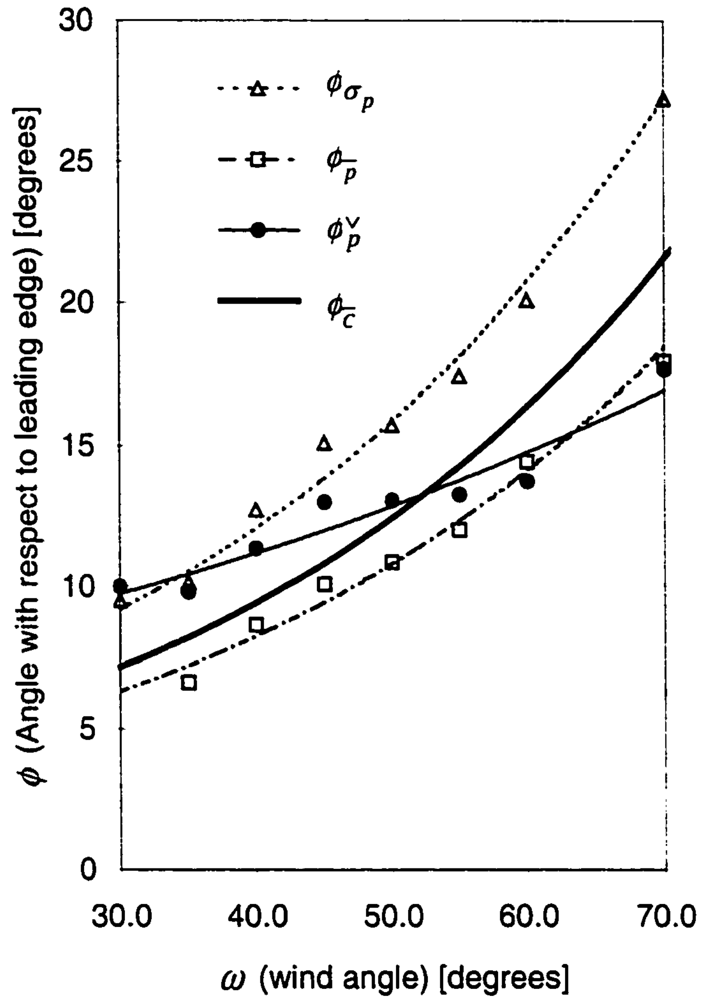

Figure 1.9: Relative position of maximum C_p rays and vortex core. Data is from ABL flow. Lines are a second order polynomial fit.

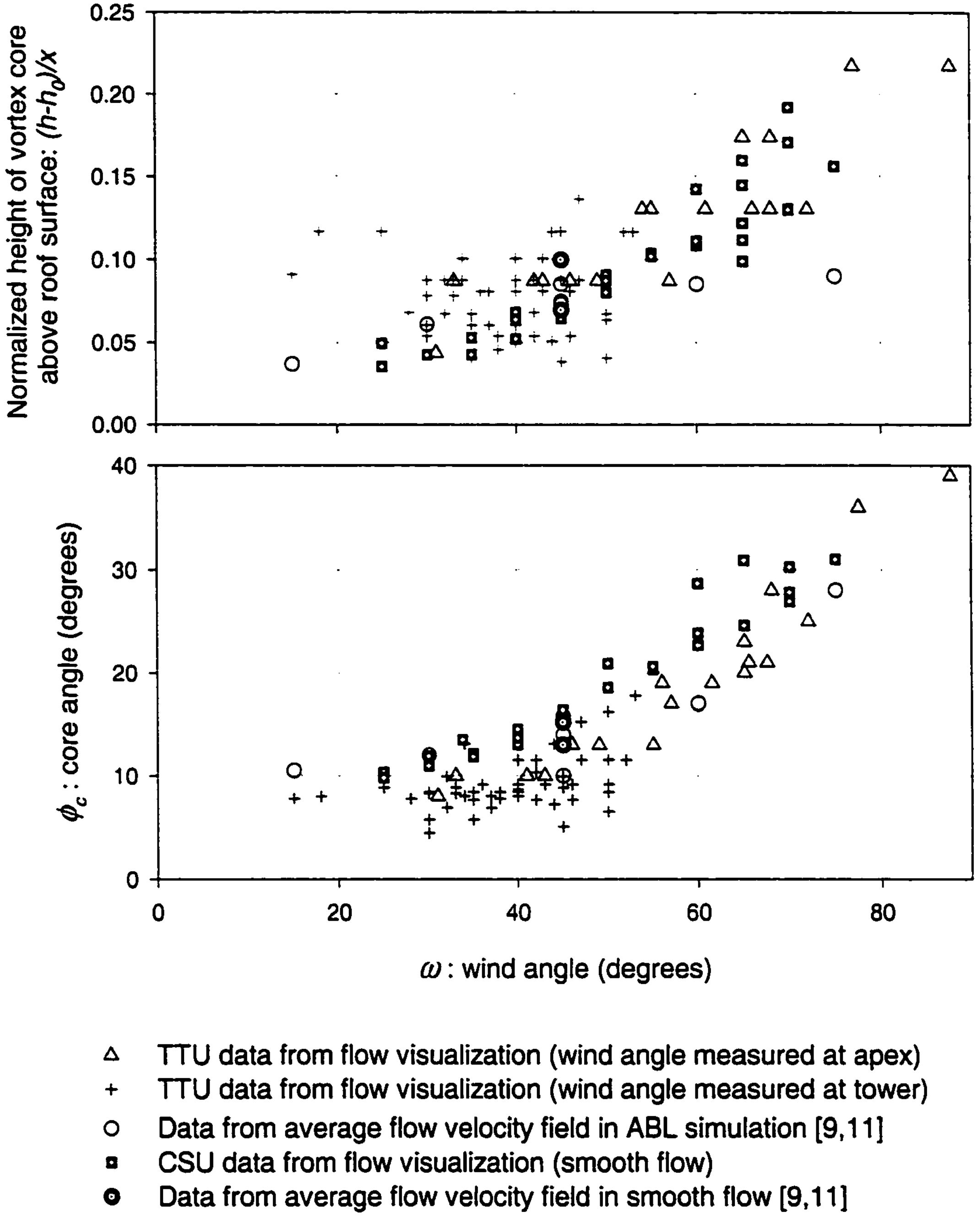

Figure 1.10: Vortex core position as a function of wind angle

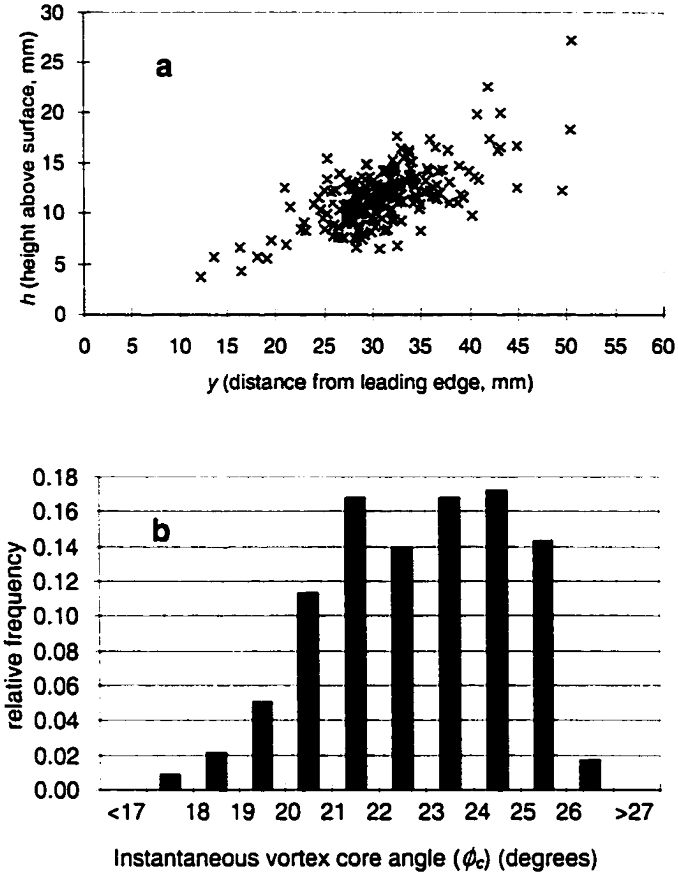

Figure 1.11: Vortex core movement during a 4 second long wind tunnel test a) Turbulent flow, $\omega = 45°$ b) Smooth flow, $\omega = 55°$

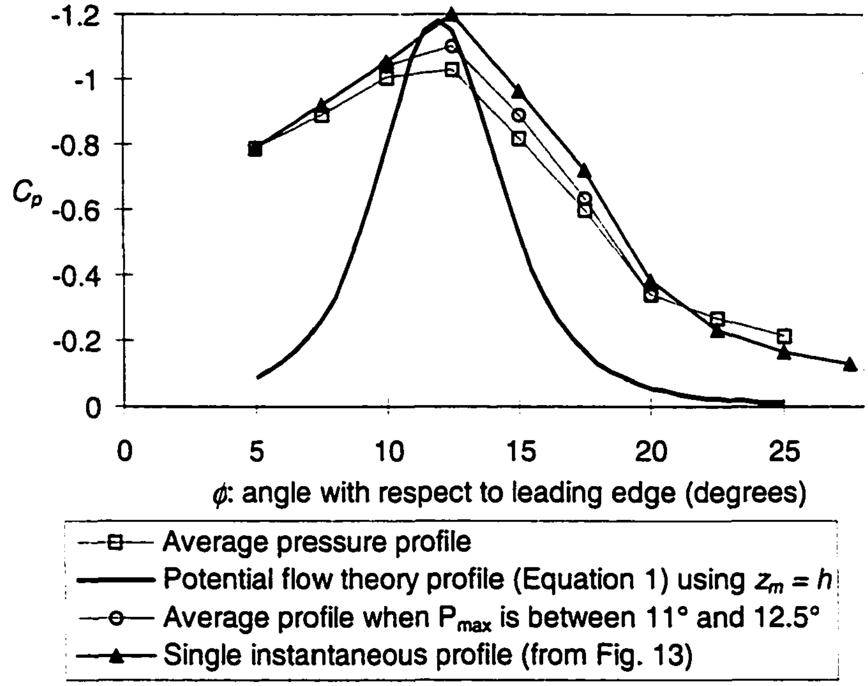

Figure 1.12: surface pressure profiles, $\omega = 45°$

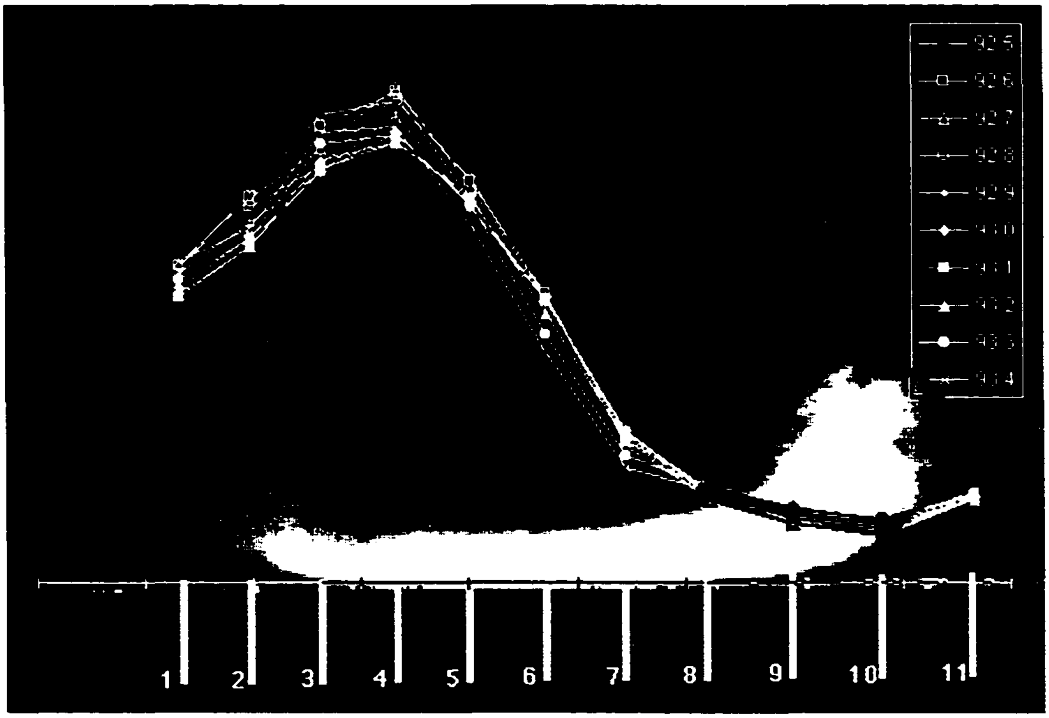

Figure 1.13: Vortex image for $\omega = 45°$. The building corner is dark gray, and the pressure taps locations are indicated in white. The 10 surface pressure profiles measured during the image's exposure are superimposed upon the image. $Cp = 0$ at the roof surface. The core is above tap #4 in this picture.

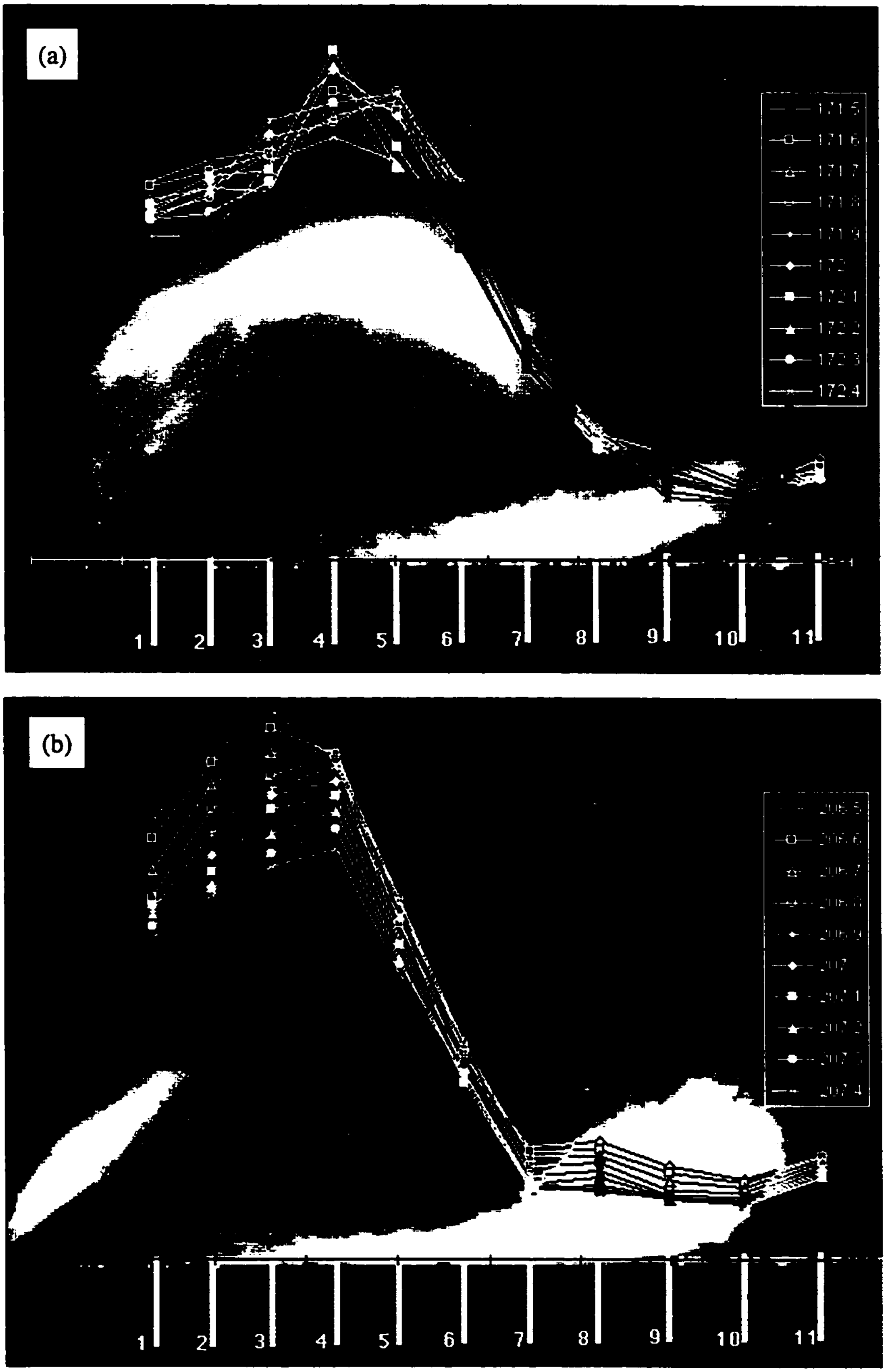

Figure 14: Vortex images for $\omega = 45°$, with simultaneous pressure profiles.

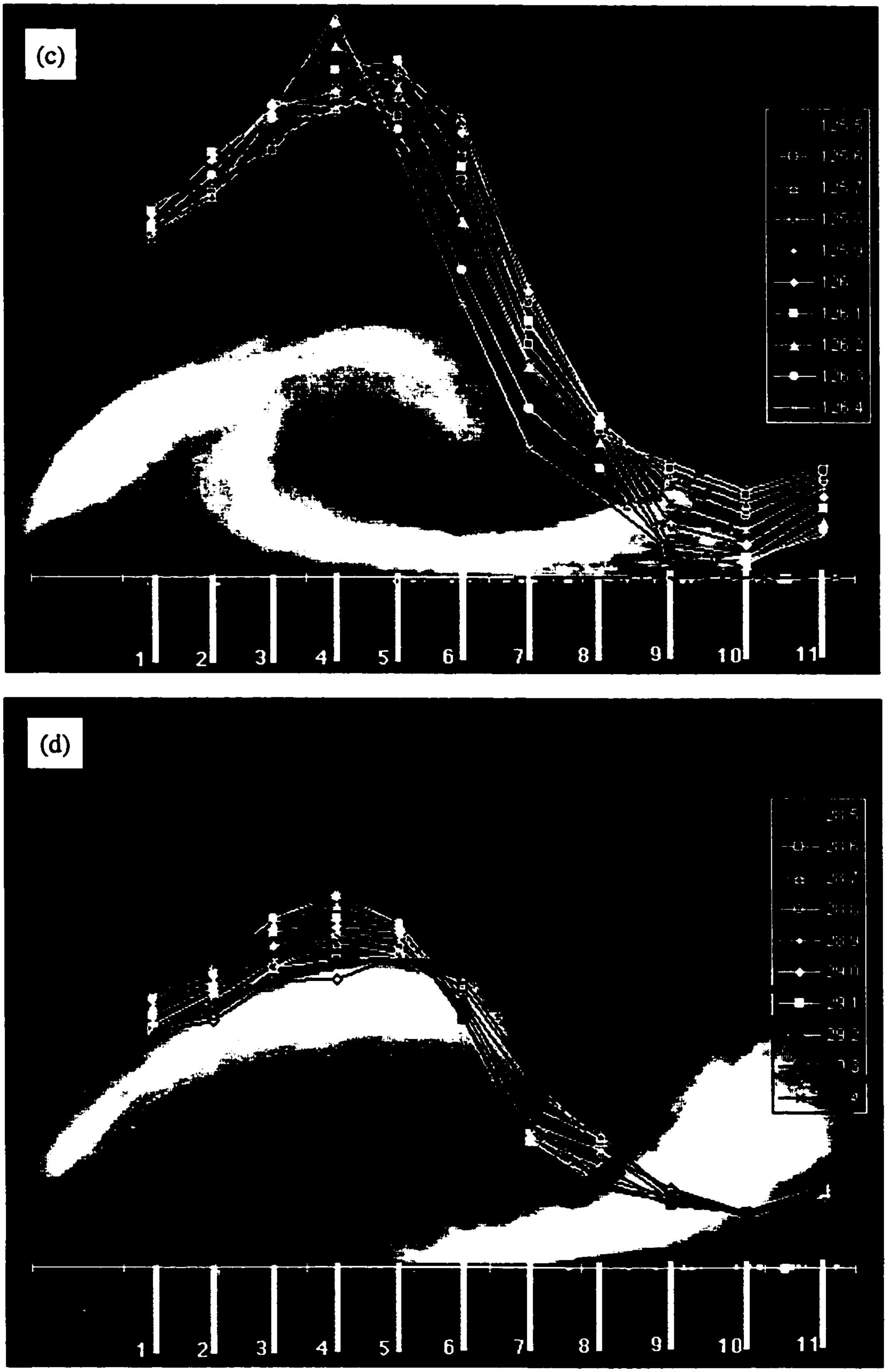

Figure 14 Continued

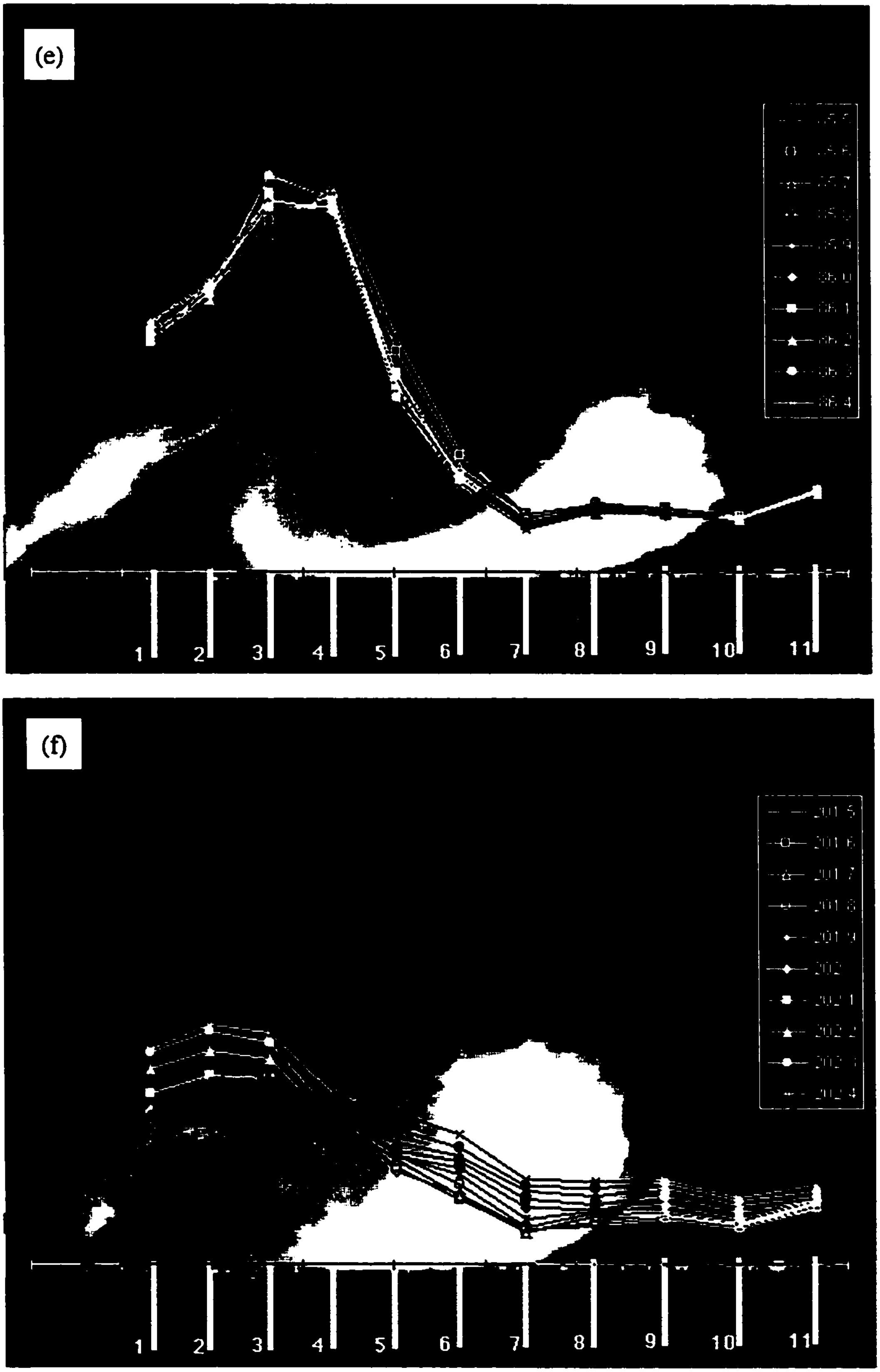

Figure 14 Continued

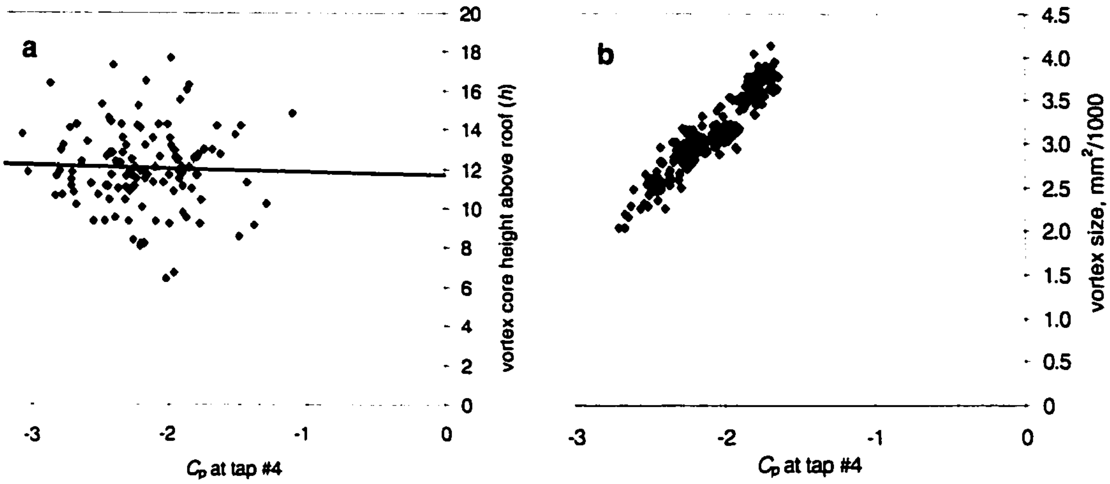

Figure 1.15: Dependence of suction on vortex size. a) turbulent flow, $\omega = 45°$ (line indicates least squares linear curve fit) b) smooth flow, $\omega = 55°$

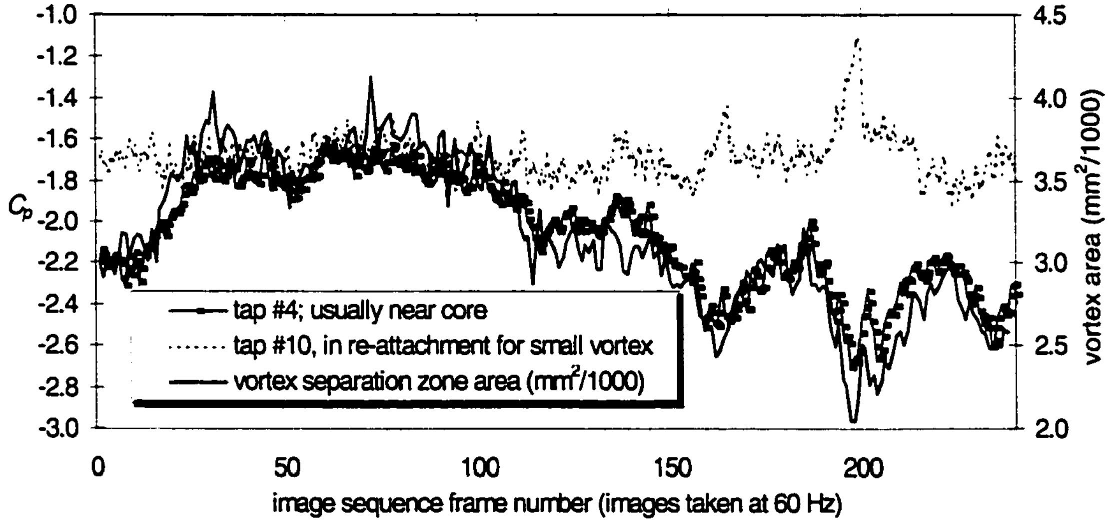

Figure 1.16: Pressure coefficient time series (smooth flow, $\omega = 55°$)

CHAPTER 2: A MODEL OF ROOF-TOP SURFACE PRESSURES PRODUCED BY CONICAL VORTICES

Most of the material in Chapter 2 has been submitted to "Wind and Structures", an international wind engineering journal. Much of this material also appears in abbreviated form in the proceedings of the 10th International Conference on Wind Engineering, which took place in Copenhagen in June 1999. (pg 1097-1104, Ed. Larsen, Larose, Livesey)

2.1 Introduction

The evidence in Chapter 1 that the vortex position changes with wind direction provides some explanation not only for the mean and rms pressure patterns on the roof, but also for one of the established connections between upstream flow and surface pressure. Recall that Kawai and Nishimura (1996) concluded that the dual conical vortices sway in unison, and in concert with low frequency lateral turbulence. Low frequency lateral turbulence is the same as a change in wind direction, which would cause both vortices to move to new positions- one closer to the edge, and the other farther from it – hence, swaying in unison.

This connection between incident large scale/low frequency lateral turbulence and suction beneath the separated flow was also confirmed through the use of frequency domain analyses (Hajj, et al. 1997) and wavelet analysis on full-scale data from TTU (Jordan, et al. 1997). However, neither of these studies supplied substantiation of the connection between upstream small-scale lateral turbulence and surface pressure fluctuations which has been proposed in other papers (Tieleman, et al. 1998, Tieleman, et al. 1994).

One issue in performing an analysis which connects upstream flow conditions with surface pressure is the position upstream at which the velocity measurements are recorded. Simultaneous upstream laser doppler anemometer (LDA) measurements of u-v-w velocity fluctuations were compared with model surface pressures by Letchford and Marwood (1997). These flow velocity measurements were taken quite close to the building, at distances upstream from 2H to 0.1H, where H is building height. Conditional sampling was used to isolate the effects of instantaneous wind direction on Cp values. Their conclusion was that extremes in pressures were associated with large excursions in lateral velocity, specifically excursions toward a flow normal to the wall. Most significantly, this was only true for velocities measured less than 0.5H upstream. Even 2H is too far upstream for a good correlation between wind direction and surface pressure.

The goal of this dissertation is to provide a better understanding of the mechanism by which the vortex generates extreme rooftop suction. Given that the correlation between velocity and pressure increases dramatically with proximity of flow measurement to the roof edge, it seems appropriate to focus on the manner in which the vortex transfers local velocity variations into surface pressure fluctuations. This can be facilitated experimentally by adding velocity measurement probes to the facilities described in section 1.2.

Several studies have already been performed to examine the flow field near the roof's leading edge. Velocities within the conical vortex have been measured using hot-wire probes, and the mean velocity fields documented (Kawai 1997). Marwood and Wood (1997) made LDA measurements of velocities within the vortex and simultaneously sampled the surface pressure beneath the mean core position in smooth and turbulent flow. At each measurement location the velocities associated with the most negative 2.5% of the recorded Cp's were extracted and averaged, creating a mean low Cp velocity field in a process called conditional sampling.

The vortex size and core position can be determined from the centre of velocity field rotation. The results indicated that for $\overline{\omega} = 45°$, larger than average vortices produced the greatest surface suction (Fig. 1.2). These conditional sampling results are somewhat prejudiced by the use of a single pressure tap placed farther from the edge than the mean core position for $\overline{\omega} = 45°$. As a result, the lowest suction would tend to occur when the vortex core is directly above the tap, which requires a larger than average vortex. Nonetheless, the comparison of mean vortex position with mean and peak roof-pressure contours shows that larger than average vortices do provide greater suction for $\overline{\omega} = 45°$. However, this only holds true for mean wind angles below 55°. For wind angles above 60°, smaller-than-average vortices produce the peak suction (see Fig. 1.9). This is because the wind angle range known to produce the lowest mean Cp's is $55° < \omega < 60°$ (Lin *et al.*, 1995), and as mentioned above, vortex size increases with wind angle. This indicates that the vortices producing the peaks tend to be similar in size to those found for $\omega = 60°$, and that peak suctions for all wind angles could simply be due to momentary wind direction shifts toward that range. This is essentially what the quasi-steady theory assumes.

The Q-S theory combines information about upstream flow conditions with measured mean pressure coefficients to predict peak pressures via the equation (Cook 1990):

$$Cp(t) = \left(\frac{U_{ref}(t)}{\overline{U}_{ref}} \right)^2 \cdot \overline{Cp}(\omega(t)) \tag{2.1}$$

As will be shown in Chapter 4, there is considerable evidence that this relationship is not valid under the vortices. There are also studies indicating that it does a reasonably good job of predicting Cp(*t*). What is not indicated is whether or not Eq. (2.1) *ought* to apply under zones of separated flow.

Similar questions arise when one examines other empirical results, such as those of Chapter 1 or the work of Letchford and Marwood (1997). Why *should* smaller vortices cause greater suction? How would a large momentary excursion towards flow normal to the wall cause extreme suction? Without some theoretical framework, it is difficult to either interpret the experimental results or design further experimental tests.

The objective here is to better understand the mechanism linking vortex structure, the local flow velocity and the surface pressure. I believe that inferences made regarding this mechanism, such as those regarding the effect of vortex size, can be improved if they are made in the context of a simple flow model. I also believe that experimental design decisions, such as where and how to measure the flow velocity, can also benefit from the insight provided by the framework of a flow model. To that end, a model of the instantaneous link between flow in and around the recirculation area and the surface pressure beneath the vortex is developed in this chapter.

2.2 Existing surface pressure profile models

2.2.1 Point vortices in potential flow

Several groups (Kawai and Nishimura 1996, Marwood 1996), have compared the predictions of 2-D potential flow theory to the actual surface pressure profile along a line normal to the conical vortex axis. The results generally appear favourable in that the theoretical curve shape follows the data reasonably well.

These theoretical roof surface pressure profiles are based upon the flow field induced in potential flow theory by the placement of two counter-rotating vortices a distance $2h$ apart. The flat streamline between them is considered to be the roof surface (Fig. 2.1). The resulting surface flow velocity is given by

$$U(\xi)\big|_{z=0} = \frac{\Gamma h}{\xi^2 + h^2} \tag{2.2}$$

where Γ = circulation or strength of each vortex and $\xi = 0$ directly between the vortices. (Wilcox (1997) provides a good derivation of this formula.)

In order to apply potential flow theory, the flow must be incompressible ($\vec{\nabla}\cdot\vec{u} = 0$) and irrotational ($\vec{\nabla}\times\vec{u} = 0$, which implies $\vec{u} = \vec{\nabla}\cdot\phi$; it also implies inviscid flow). If the flow is also steady, the steady form of Bernoulli's equation can be used to predict the surface pressure along the ξ axis:

$$P = P_\infty - \tfrac{1}{2}\rho U^2(\xi)\,, \tag{2.3}$$

where P_∞ is the static pressure when the flow stops, in the limit as $\xi \to \infty$ and $U \to 0$.

Let $\Delta P \equiv P - P_\infty = -\frac{1}{2}\rho\left(\frac{\Gamma\cdot h}{\xi^2 + h^2}\right)^2$, so that at $\xi = 0$ $\Delta P = \Delta P_{\min} = -\frac{1}{2}\rho\left(\Gamma/h\right)^2$.

The pressure distribution is now normalized by $\Delta P_{\min}$ to get

$$\frac{\Delta P}{\Delta P_{\min}} = \left(\frac{h^2}{\xi^2 + h^2}\right)^2 = \left(\frac{1}{\left(\xi/h\right)^2 + 1}\right)^2 \tag{2.4}$$

The vortex core height above the surface (h), has been measured from the flow visualization images, and used in Eq. (2.4). This procedure provides a reasonably good curve fit to aerospace data for swept delta wings with included angles less than 40° and tested at angles of attack above 20° (Greenwell and Wood 1992). For a building's square corner, with an included angle of 90° and an effective angle of attack I estimate at around 10° (depending on building height), the agreement is not as good. As noted in Chapter 1, when actual values of h for roof-top vortex cores are used, it badly under-predicts the half width of the surface pressure profile.

To overcome this problem, a virtual core height is inferred from the pressure profile's half width: The half-height point on the $\Delta P/\Delta P_{\min}$ curve is selected, so that $\xi = \xi_{1/2}$ when $\Delta P/\Delta P_{\min} = 0.5$. By substituting $\Delta P/\Delta P_{\min} = 0.5$ and $\xi = \xi_{1/2}$ into Eq. (2.4), we get $h = 1.55\xi_{1/2}$. This virtual core height is often twice the actual core height.

In many implementations of Eq. (2.4), Cp is substituted for ΔP, so that $\xi = \xi_{1/2}$ at $Cp/Cp_{\min} = 0.5$, where $Cp_{\min}$ is the minimum Cp (i.e. the maximum suction) for a given x = constant line. This is not strictly correct, since

$$\frac{\Delta P}{\Delta P_{\max}} = \left(\frac{P - P_{ref} - \frac{1}{2}\rho U_{ref}^2}{P_{\max} - P_{ref} - \frac{1}{2}\rho U_{ref}^2} \right) = \left(\frac{Cp - 1}{Cp_{\max} - 1} \right), \qquad (2.5)$$

where Cp is defined as $Cp \equiv \dfrac{P - P_{ref}}{q}$.

The reason why Cp can be used in the place of ΔP in Eq. (2.4) is discussed in the next section.

The value of $Cp_{\min}$, rather than being calculated from vortex circulation, is, like the virtual height, extracted from the data. Hence, both input parameters (h and $Cp_{\min}$) are estimated from the data, and the model becomes essentially a curve fit to surface pressure data.

2.2.2 Rankine vortex based pressure profile

Cook's designer's guide provides a similar curve fit, based on the pressure profile through the core of a Rankine vortex (Cook 1990). A Rankine vortex features a fully viscous vortex core rotating as a solid body, surrounded by and irrotational, inviscid vortex (Fig. 2.2). The pressure coefficients for this flow are given by

$$Cp_{inner} = Cp_o + \frac{U^2(r)}{U_{ref}^2} \quad \text{(from the integration of } \frac{dP}{dr} = \frac{\rho U^2}{r}\text{)}$$

$$Cp_{outer} = 1 - \frac{U^2(r)}{U_{ref}^2} \quad \text{(from Bernoulli's equation)}$$

Matching the pressure coefficients at R gives

$$Cp_{inner}(R) = Cp_{outer}(R) = Cp_o + \frac{U_R^2}{U_{ref}^2} = 1 - \frac{U_R^2}{U_{ref}^2} \text{ so that } Cp_o = 1 - 2\frac{U_R^2}{U_{ref}^2}.$$

Since $U_{outer}(r) = k/r$, $U_R = k/R$ and $U_{inner}(r) = kr/R^2$, where k is a constant, the Cp(r) formulae are

$$Cp_{outer} = 1 - \left(\frac{k}{r \cdot U_{ref}}\right)^2, Cp_o = 1 - 2\left(\frac{k}{R \cdot U_{ref}}\right)^2, \text{ and}$$

$$Cp_{inner} = 1 - 2\left(\frac{k}{R \cdot U_{ref}}\right)^2 + \left(\frac{k \cdot r}{R^2 \cdot U_{ref}}\right)^2$$

This profile is then assumed to exist at the roof surface, so that Cp_{min} becomes Cp_o and r becomes ξ. As $\xi \to \infty$, $U(\xi) \to 0$, so that $Cp_{outer} \to 1$ and Cp/Cp_{min} approaches $1/Cp_{min}$. The same is true for the potential flow/point vortex model, since $\Delta P/\Delta P_{min} \to 0$ as $\xi \to \infty$, which from Eq. (2.5) implies that Cp → 1. However, the data measured in this study and elsewhere suggest that Cp = 0 or Cp = -0.2 is a more appropriate asymptote.

The measured Cp values do not approach +1 when the flow appears to "stagnate" within the separation zone, as at the point of re-attachment. This is perhaps in part because the flow is really 3-dimensional, so that there is not a true stagnation, since $U_{axial} \approx U_{ref}$ at the point of reattachment (Marwood 1996). It could also be the result of the overall flow acceleration and curvature above the building, which reduces pressures over the whole roof as well as on the back wall.

Whatever the reason, the use of Cp($\xi \rightarrow \infty$) = 0 as the asymptote simplifies the Rankine-based equations. If the value of Cp along the roof surface is considered to be reduced for all ξ by 1.0, then $Cp_{outer} = 0$ when $\xi \rightarrow \infty = 0$, since

$$Cp_{outer} = \left(\frac{k}{\xi \cdot U_{ref}}\right)^2, Cp_{\min} = -2\left(\frac{k}{R \cdot U_{ref}}\right)^2 \text{ and } \quad Cp_{inner} = -2\left(\frac{k}{R \cdot U_{ref}}\right)^2 \cdot \left(1 - \tfrac{1}{2}\frac{\xi^2}{R^2}\right)$$

so that

$$\left(\frac{Cp_{inner}}{Cp_{\min}}\right) = 1 - \tfrac{1}{2}\left(\xi / R\right)^2 \text{ and } \left(\frac{Cp_{outer}}{Cp_{\min}}\right) = \tfrac{1}{2}\left(R / \xi\right)^2$$

The model given in Appendix M of Cook's designer's guide approximates this relationship with the equation

$$\frac{Cp}{Cp_{\min}} = \frac{1}{(1+A^2)} \text{ where } A = \xi/R \text{ and } \xi_{1/2} \text{ can be used for R.} \qquad (2.6)$$

In Fig 2.3, the curves from Eqs. (2.4) and (2.6) are compared to mean data taken at CSU on a 1:50 model of the TTU Wind Engineering Research Field Laboratory (WERFL) building (Levitan and Mehta 1992) and on a larger 45cm x 45cm cubic model. The agreement is good in the region between the pressure peak and the roof centre, while the measured pressures remain significantly greater between the pressure peak and the leading edge.

2.2.3 Weaknesses of the surface pressure profile models

These models are simply symmetrical curve fits to the surface pressure data, and the asymmetric shape of the surface pressure profile can perhaps be better approximated with a polynomial curve fit.

These models also offer little insight into the manner in which the vortex controls suction on the roof surface. While the Rankine based model infers a surface profile similar to that through the vortex core, it does not attempt to describe the flow field. The potential flow model does describe the flow field, but it is actually misleading. The tangential velocity is predicted to increase infinitely (with $1/r$) as the vortex core is approached, and surface pressures are assumed to simply follow the Bernoulli equation. For a mean Cp of -2.5, this requires a mean total velocity at the roof surface beneath the vortex of 1.9 times the mean upstream flow velocity at roof height (U_{ref}). Measurements taken for this study and elsewhere (Marwood 1996) indicate that the total velocity just above the surface in this case is usually quite close to U_{ref} (though much more turbulent, with more energy at higher frequencies).

Tap number 50501 on the TTU WERFL site roof is located at a normalized distance from the corner of $x/H = 0.36$, and at an angle with respect to the wall edge of $\phi = 14°$. Pressures measured at this tap are known to be quite low when it is beneath a conical vortex, with a mean Cp of –2.5 for $\omega = 60°$. Peak Cp's for tap 50501 for a test lasting 15 minutes are often around -11 (Cochran and Cermak 1992). This would require wind speeds of $U_S(t) = 3.5$ times $\overline{U}_{ref}$. Note that this implies winds speeds of over Mach

0.5 during a hurricane. This also implies a local gust of 1.85 times the mean local velocity, or 4.25 σ_U above the mean for a turbulence intensity of $\sigma_U/U = 20\%$. The model which is developed in the following section demonstrates how Cp's of -11 can be achieved with wind speeds of only 2.4 times $\overline{U}_{ref}$, and gusts of only 1.6 times the mean local velocity (or $3\sigma_U$ above the mean for $\sigma_U/U = 20\%$).

2.3 The vortex model

This section presents a model that emphasizes the interaction of the flow velocity above the vortex and the streamline curvature within the vortex in producing the low surface pressures. The model will be used to examine changes in *Cp* as a function of wind angle, distance from the apex, and local flow speed.

The nomenclature and overall flow pattern for the model are shown in Fig 2.4. Instead of envisioning a flow field driven by a vortex, as in the potential flow model, we imagine the vortex to be like a wheel, being spun by the free stream at the point M. At the centre of the flow field model is a vortex similar to the Rankine vortex. The velocity profile associated with a Rankine vortex, shown in Figs. 2.2 and 2.5, is unrealistic, since the velocity will not change so abruptly as the circulating flow gradually changes from constant vorticity to zero vorticity. Instead, there will be a transition zone above the vortex in the shear layer, also shown in Fig. 2.5. In between the transition region and the core, experimental measurements (Marwood 1996) and numerical solutions (full Navier Stokes above a delta wing (Rizzi and Muller 1989)) show that the velocities within the real core are expected to follow a profile somewhat akin to the law of the wall. The velocity here is approximated by a power law profile. The viscous inner region is probably reduced to a very small area near the core ($r/h < \sim 0.2$). Above the transition region, the rotating flow merges with the free stream, so that U approaches U_{ref} instead of 0.

The pressure changes which occur towards the core (the point O) and the surface (the point S) are associated with centrifugal accelerations, $-mU^2/r$; hence, the local governing equation is

$$\frac{dP}{dn} = \frac{\rho U^2}{R_c} \tag{2.7}$$

where n is the unit normal to the curvature, R_c is the radius of curvature, and U is the fluid speed in the direction of vortex rotation.

2.3.1 Radius of curvature

Near the core, $R_c = r$ and $dr = dn$, so Eq. (2.7) is identical to that for circular flow. As the flow beneath the vortex approaches the roof, however, the radius of curvature must become infinite, since it will be parallel to the flat roof at the surface. Letting $a = (\zeta / h)$, I model $Rc / h = a/(1 + a)$ between the core and the roof ($-1 < a < 0$). This satisfies these limits, since $R_c \rightarrow -\infty$ as $a \rightarrow -1$ and $R_c/h \rightarrow a$ as $a \rightarrow 0$. The flow will also straighten out above the vortex, eventually merging with the flow curvature associated with the overall flow around the building. A curve-fit to the R_c values calculated for flow above a 2-D surface mounted prism by the CFD code FLUENT yields a relationship of the type $R_c^{upward} / h = a + Ba^C$, where B = 0.5 and C = 3. Flow visualization also gives $R_c^{upward} / h = 2a$ at $\zeta \approx 1.25h$.

2.3.2 Velocity profile

The velocity profile shown in Fig. 2.5 for $0.25 < a < 1$ is exponential:

$$\frac{U}{U_{a=+1}} = a^{\gamma} \text{ where } \gamma = \tfrac{1}{2}. \qquad (2.8)$$

This equation is based upon a curve fit to the velocity profile presented in Rizzi's numerical solution of the complete Navier-Stokes equations for a 65° sweep delta-wing at a 10° angle of attack at x/c_R=0.7 and M_∞=0.85 (Rizzi and Muller 1989). The fit is shown in Fig. 2.6a. A similar curve fit is performed with Marwood's rooftop LDV data in Fig. 2.6b, where U_{max} is not known, so the data is normalized by $U(h/2)$. A power law curve fit was chosen in part because if $U = C_1\sqrt{a}$ is substituted into Eq. (2.7), the pressure is seen to vary linearly with a, $P = \rho C_1^2 a$. This linear variation agrees well with data reported in several numerical simulations, adapted for Fig. 2.7. (The pressure values decrease less rapidly beneath the core because the radius of curvature increases more quickly towards the roof surface, as noted above)

Near enough to the core, viscosity is expected to dominate, so the flow must rotate as a solid body, as in the Rankine vortex, with $U \propto r$.

In the potential flow region, both the Bernoulli equation and Eq. (2.7) must be obeyed. Using the assumed radius of curvature $R_c(\zeta)$, the velocity profile can be calculated:

$$P = P_\infty - \tfrac{1}{2}\rho U^2 \quad \therefore \frac{dP}{dn} = -\tfrac{1}{2}\rho\frac{dU^2}{dn}.$$

Substitute this into Eq. (2.7) to get

$$-\tfrac{1}{2}\rho\frac{dU^2}{dn'} = \frac{\rho U^2}{(R_c/h)} \text{ where } n' = n/h.$$

Isolate the variables and integrate each side to get

$$\int_{a_3}^{a} \frac{1}{U^2} dU^2 = \int_{a_3}^{a} \frac{-2}{(R_c / h)} dn'$$

where a_3 is the normalized radial distance from the core centre to the start of the potential flow region (assumed to be $2h$). Solving the integral gives

$$\ln(U^2) - \ln(U_3^2) = \int_{a_3}^{a} \frac{-2}{(R_c / h)} dn' \quad \text{or} \quad \frac{U}{U_3} = \sqrt{e^{\left(\int_{a3}^{a} \frac{-2}{(R_c/h)} dn\right)}}$$

In the transition region, a curve has been chosen with a maximum at $a_{max} = (a_2+a_3)/2$, where a_2 borders the vortex region. This curve's slope attempts to match those of the neighbouring regions at a_2 and a_3. The full set of velocity profile equations is given in Table 1.

2.3.3 The vortex as pressure drop amplifier

The pressure drop to the surface is calculated through the integration of Eq. (2.7) from the point M towards the vortex centre, along the ζ axis:

$$\int_{M}^{S} dP = \int_{M}^{S} \frac{\rho U^2}{(R_c/h)} da .$$

Normalizing by the reference flow head gives

$$Cp_S - Cp_M = 2\int_{M}^{S} \frac{U^2(a)}{U_{ref}^2 \cdot (R_c/h)(a)} da$$

Normalizing the cross-vortex velocity profile by U_M instead of U_{ref} gives

$$Cp_S = Cp_M - \frac{U_M^2}{U_{ref}^2} \left[2\int_{S}^{M} \frac{U^2(a)}{U_M^2 \cdot (R_c/h)(a)} da \right]$$

where the integral is reversed to give a positive value. Cp_M can be calculated from the velocity at M using the Bernouilli equation, $P_M - P_{ref} = \frac{1}{2}\rho(U_{ref}^2 - U_M^2)$ since M is in the potential flow region:

$$Cp_M = \frac{P_M - P_{ref}}{\frac{1}{2}\rho U_{ref}^2} = 1 - \frac{U_M^2}{U_{ref}^2}.$$

Substituting into the equation for Cp_S yields

$$Cp_S = 1 - \frac{U_M^2}{U_{ref}^2}\left[1 + 2\int_S^M \left(\frac{U}{U_M}(a)\right)^2 \cdot \left(\frac{R_c}{h}(a)\right)^{-1} da\right] \tag{2.9}$$

Let $\Delta Cp = 1 - Cp$. At the point M, this is equivalent to the pressure coefficient change due to the increased flow velocity, since $\Delta Cp_M = (U_M/U_{ref})^2$. Letting g = the integral in the square brackets gives $\Delta Cp_S = (1+g)\cdot\Delta Cp_M$. This implies that the vortex can be simply viewed as an amplifier of the velocity related pressure drop at M.

The $g(a)$ profile calculated along the ζ-axis using these $R_c(a)$ and $U(a)$ functions is plotted in Fig. 2.8, along with the $g(a)$ for circular flow around a Rankine vortex. The figure shows that the total amplification has been reduced (relative to the Rankine pressure drop) by the decrease in curvature (especially in the transition region). An asymmetric "leak" of high amplification from the core to the surface is also evident, since $g(-1) > g(1)$. The leak transfers about half of the vortex core pressure drop (i.e. the drop from $a = 1$ to $a = 0$) to the surface. The pressure loss across the vortex (from $a = 1$ to $a = -1$) can be seen to be roughly equivalent to that across the transition region.

2.3.4 Effect of wind angle on Cp

The flow model depicted in Fig. 2.4 is for a 2-d plane normal to the leading edge, so that only a component of the total velocity at M, $U_M\cdot\sin(\alpha)$ is acting to rotate the vortex. The angle α is the wind angle at the point M with respect to the vortex core; it is illustrated in Fig. 2.9. Experimental measurements show that the wind changes direction as it passes over the leading edge of the roof, shifting to become roughly 10° to 20° more normal to the roof's edge. Since the vortex core is displaced from the leading edge by an angle ϕ_C which is also usually between 10° and 20°, the net effect is that α follows ω fairly closely, as shown in Fig. 2.10.

Using the full 3-d velocity to calculate the pressure drop at point M, Eq. (2.9) becomes

$$Cp_S = 1 - \frac{U_M^2}{U_{ref}^2}\left[1 + \sin^2(\alpha) \cdot g_S\right] \tag{2.10}$$

where g_S is the value of $g(a)$ at the point S and α is a function of ω, as noted above. Eq. (2.10) can be used to calculate the Cp(a) profile along the ζ-axis by using $g(a)$ from Fig. 2.8. A final comparison with aerospace delta-wing numerical simulation results is shown in Fig. 2.11, and good agreement is seen between the profile shapes.

2.3.5 Incorporating time dependence

2.3.5.1 A quasi-steady approximation

Visualization of the vortex indicates that for any wind angle, the vortex rapidly and erratically changes its position and size. However, the shape of the vortex is generally self-similar (circular), so provided that the vortex is not "washed out" (absent), it is reasonable to assume that g_S will not depend upon the wind direction. If this is the case, the model's surface pressure predictions can be compared to a measured Cp$_S$ time series by using Eq. (2.10) to calculate $\overline{\mathrm{Cp}}(\omega(t))$ for Eq. (2.1):

$$Cp_S(t) = \left(\frac{U_{ref}(t)}{\overline{U}_{ref}}\right)^2 \left(1 - \frac{\overline{U}_M^2}{\overline{U}_{ref}^2}\left[1 + \sin^2(\alpha(t))\cdot g_S\right]\right) \tag{2.11}$$

where U_{ref} must be measured at a point near the roof edge, as noted in the introduction. The points M and C have both proven suitable for this purpose.

2.3.5.2 The Intermittency Factor

Visualization tests have shown that as the wind angle is increased, the vortex becomes increasingly unstable, and disappears and reappears erratically. To account for this, an "intermittent vortex factor", $I(t)$, can be introduced to the amplification factor :

$$g(t) = g_S \cdot I(t)$$

where $g_S = 1.5$ from Fig. 2.8 and the mean value of $I(t)$ is expected to be close to 1 for $\omega < 55°$, and to decrease to almost 0 at $\omega = 90°$. It was initially expected that $I(t)$ would function as a delta function; if the vortex were present, $I_\delta = 1$, otherwise, $I_\delta = 0$. Since the vortex continues to appear sporadically even at $\omega = 90°$[1], I_δ could be unity for any wind angle. Data to be presented in Chapter 3 will show that there is more of a continuum of $g(t)$ values, with a mean and distribution that depends upon the wind angle. The resulting prediction for the surface pressure time series beneath the vortex core is

$$Cp_S(t) = \left(\frac{U_{spin}(t)}{\overline{U}_{spin}}\right)^2 \left(1 - \frac{\overline{U}_M^2}{\overline{U}_{ref}^2}\left[1 + \sin^2(\alpha(t))\cdot g(t)\right]\right) \tag{2.12a}$$

where U_{spin} emphasizes that the local flow speed must be used for U_{ref} if Eq. (2.11) is to be valid. It can be measured at points such as C or M. The mean value becomes

---

[1] Experimental results indicate that the flow in this apparently two dimensional case is actually very three dimensional, with circulating flows, or small, unstable vortices, being shed from the leading edge erratically. These flow structures cause the greatest surface suctions within the bubble, confirming results

$$\overline{Cp}_S = \left(1 - \frac{\overline{U}_M^2}{\overline{U}_{ref}^2}\left[1 + \sin^2(\overline{\alpha})\cdot g(\overline{\omega})\right]\right). \tag{2.12b}$$

2.4 Discussion

The "speed-up ratio" as flow passes over the downwind separation bubble at the ridge of a steep escarpment is of the order 1.6 (Cook 1985). The speed-up ratio in this case is defined as the ratio of flow speed above the separation bubble (U_C) to that along the same streamline in the undisturbed upstream flow (U_a) (see Fig. 2.12). If U_a is measured at a height of H/3 and an exponential open country velocity distribution (α = .14) is assumed, then U_C/U_{ref} is roughly

$$\frac{U_C}{U_{ref}} = \frac{U_C}{U_a}\cdot\frac{U_a}{U_{ref}} = 1.6\cdot\left(\frac{z_a}{z_{ref}}\right)^{.14} = 1.4$$

Measurements taken for this experiment and described in Chapter 3 confirm this estimate, giving U_M/U_{ref} = 1.42 for x/H = 0.38. It is also shown in Chapter 3 that while g > 1.5 for a strongly re-attaching vortex, weaker re-attachment can lower g considerably. This is not too surprising, since g should be 0 if there is no reattachment and no vortex. Using $\overline{g} = 0.9$ and $\overline{\alpha} = 60°$ in Eq. (2.12a) gives

$$\overline{Cp}_S = \left(1 - (1.42)^2\left[1 + \sin^2(60°)\cdot 0.9\right]\right) = -2.5$$

which, as noted in section 2.3, is the mean Cp for tap 50501 at $\omega = 60°$. If we assume that peak suctions of Cp = -11 coincide with a strong vortex ($g(t)$ = 1.7) and a momentary shift in wind direction to $\alpha(t) = 80°$, then Eq. (2.12a) gives

---

reported by Saathoff and Melbourne (1989). They generally travel away from the leading edge, but can also move laterally in either direction.

$$\left(\frac{U_{spin}(t)}{\overline{U}_{spin}}\right)^2 = \frac{-11}{1-(1.42)^2\left[1+\sin^2(80°)\cdot 1.7\right]} = 1.6 .$$

Gusts of this size become increasingly likely as σ_U/U increases, so the likelihood of large negative peak pressures ought to increase as well. This has been observed: peak Cp's below −10 at tap 50501 are seldom seen when $\sigma_U/U < 20\%$, but are relatively common for $\sigma_U/U > 20\%$ (Tieleman, et al. 1996).

As noted in section 2.3, a 20% turbulence intensity at roof height implies that $U_{ref}(t) > 1.6\overline{U}_{ref}$ for gusts of $U(t) > U + 3\sigma_U$, a condition which occurs over 10 times per 15 minute run (when sampled at 10Hz). Cp's below −11 are not this common because these large gusts must coincide with a shift in wind direction toward flow normal to the wall, and $\alpha(t)$ is greater than 75° less that 7% of the time for $\overline{\omega} = 60°$. They must also coincide with the presence of a strong vortex and solid re-attachment, a condition which is increasingly rare as $\overline{\omega} \rightarrow 90°$. As a result, peaks of this size are only seen every few runs, rather than several times per run.

Finally, section 2.3 also indicated that $U_S(t)$ would have to exceed 3.5 times the reference flow velocity to achieve a Cp of −11 if the point vortex model and its direct application of Bernoulli's equation were to apply, a condition which seems intuitively unlikely, and has not been observed experimentally. In contrast, The model embodied in Eq. (2.12a) requires a maximum velocity of only $2.4U_{ref}$ for such an event: Since $U_{max} \approx 1.05\ U_M$ (Fig 2.5), the ratio can be calculated as

$$\frac{U_{\max}(t)}{\overline{U}_{ref}} \approx \frac{U_{\max}}{U_M}\cdot\frac{U_M}{U_{ref}}\cdot\frac{U_{ref}(t)}{\overline{U}_{ref}} = 1.05\times 1.42\times 1.6 = 2.4 .$$

2.5 Conclusions

Existing conical vortex flow and surface pressure models are shown to provide bell-shaped curve fits to the surface pressure profiles. To provide greater insight into the connection between upstream flow and surface pressures beneath the conical vortices, a model of the mechanism by which the roof-top conical vortices create large suctions on the roof surface has been developed.

The model describes how the curving vortex flow causes extremely low pressures at the vortex core. The flattening of the flow beneath the vortex due to the presence of the roof surface causes some of this low pressure to act on the roof surface. The faster the vortex spins, the lower the core pressure and the lower the surface pressure. In this sense, the vortex can be seen as an amplifier of the local pressure drop due to wind gusts.

The model connects surface pressures to the upstream flow in three ways. First, the speed of the vortex spin is determined by the flow velocity component normal to the roof edge, so that the presence of lateral velocity fluctuations will affect the surface pressure through $\alpha(t)$. Second, regardless of wind angle, the pressure above the vortex will be controlled by the speed of gusts passing over the roof corner ($U_{spin}(t)$); the nature of these gusts will clearly be a function of the upstream flow. Finally, the model includes a parameter (g) which describes the quality or strength of the vortex. The value of g could be related to the nature of the re-attachment, which is in turn affected by the presence of small-scale turbulence (on the order of the width of the shear layer, < H/10).

2.6 References

Cochran, L. S., and Cermak, J. E. (1992), "Full- and model-scale cladding pressures on the Texas Tech University experimental building", *J. Wind Eng Ind. Aerodyn.*, **41-44**, 1589-1600.

Cook, N. J. (1985), *The designer's guide to wind loading of building structures, part 1.*, Building Research Establishment, Garston, UK

Cook, N. J. (1990), *The designer's guide to wind loading of building structures, part 2: static structures*, Building Research Establishment Report, Garston, UK

Ekaterinaris, J. A., and Schiff, L. B. (1994), "Numerical Simulation of Incidence and Sweep Effects on Delta Wing Vortex Breakdown", *Journal of Aircraft*, **31**(5), 1043-1049.

Greenwell, D. I., and Wood, N. J. (1992), "Determination of vortex location on delta wings from surface pressure measurements", *AIAA Journal*, **30**(11), 2736-2739.

Hajj, M. R., Janajreh, I. M., Tieleman, H. W., and Reinhold, T. A. (1997), "On frequency-domain analysis of the relation between incident turbulence and fluctuating pressures", *J. Wind Eng. Ind. Aerodyn.*, **69-71**, 539-545.

Jordan, D. A., Hajj, M. R., and Tieleman, H. W. (1997), "Wavelet analysis of the relation between atmospheric wind and pressure fluctuations on a low-rise building", *J. Wind Eng Ind. Aerodyn.*, **69-71**, 647-655.

Kandil, O. A., and Chuang, H. A. (1990), "Computation of Vortex-Dominated Flow for a Delta Wing Undergoing Pitching Oscillation", *AIAA Journal*, **28**(9), 1589-1595.

Kawai, H. (1997), "Structure of conical vortices related with suction fluctuation on a flat roof in oblique smooth and turbulent flows", *J. Wind Eng Ind. Aerodyn.*, **69-71**, 579-588.

Kawai, H., and Nishimura, G. (1996), "Characteristics of fluctuating suction and conical vortices on a flat roof in oblique flow", *J. Wind Eng. Ind. Aerodyn*, **60**, 211-225.

Kind, R. J. (1986), "Worst suctions near edges of flat rooftops on low-rise buildings", *J. Wind Eng Ind. Aerodyn.*, **25**, 31-47.

Letchford, C. W., Iverson, R. E., and McDonald, J. R. (1993), "The application of the Quasi-Steady theory to full scale measurements on the Texas Tech Building", *J. Wind Eng Ind. Aerodyn.*, **48**, 111-132.

Letchford, C. W., and Marwood, R. (1997), "On the influence of v & w component turbulence on roof pressures beneath conical vortices", *J. Wind Eng Ind. Aerodyn.*, **69-71**, 567-577.

Levitan, M. L., and Mehta, K. C. (1992), "Texas Tech field experiments for wind loads part 1: building and pressure measuring system", *J. Wind Eng Ind. Aerodyn.*, **41-44**, 1565-1576.

Lin, J.-X., Surry, D., and Tieleman, H. W. (1995), "The distribution of pressure near roof corners of flat roof buildings", *J. Wind Eng. Ind. Aerodyn.*, **56**, 235-265.

Marwood, R. (1996), *An investigation of conical roof edge vortices*, Ph.D.thesis, Lincoln College, University of Oxford, Oxford, UK.

Marwood, R., and Wood, C. J. (1997), "Conical vortex movement and its effect on roof pressures", *J. Wind Eng Ind. Aerodyn.*, **69-71**, 589-595.

Melbourne, W. H. (1993), "Turbulence and the Leading Edge Phenomena", *J. Wind Eng Ind. Aerodyn.*, **49**, 45-64.

Rizzi, A., and Muller, B. (1989), "Large-Scale Viscous Simulation of Laminar Vortex Flow Over a Delta Wing", *AIAA Journal*, **27**(7), 833-840.

Saathoff, P. J., and Melbourne, W. H. (1989), "The generation of peak pressures in separated/ reattaching flows", *J. Wind Eng Ind. Aerodyn.*, **32**, 121-134.

Tieleman, H. W., and Hajj, M. R. (1995), "Pressures on a flat Roof- application of Quasi-Steady Theory", *1995 ASCE Engineering mechanics conference*, Boulder, Co.

Tieleman, H. W., Hajj, M. R., and Reinhold, T. A. (1998), "Wind tunnel simulation requirements to assess wind loads on low-rise buildings", *J. Wind Eng Ind. Aerodyn.*, **74-76**, 675-685.

Tieleman, H. W., Surry, D., and Lin, J.-X. (1994), "Characteristics of mean and fluctuating pressure coefficients under corner (delta wing) vortices", *J. Wind Eng. Ind. Aerodyn*, **42**, 263-275.

Tieleman, H. W., Surry, D., and Mehta, K. C. (1996), "Full/model scale comparison of surface pressured on the Texas Tech experimental building", *J. Wind Eng. Ind. Aerodyn.*, **61**, 1-23.

Wilcox, D. C. (1997), *Basic Fluid Mechanics*, DCW Industries, Inc., La Canada, California

Zhao, Z., Sarkar, P. P., and Mehta, K. C. (2000), "Wind flow characteristics and their loading effects on low-rise building roofs", *(submitted to) Journal of Wind and Structures.*

2.7 Tables

R_c	Range	Description	Velocity equation
$-\infty$	$a = -1$	Roof surface	$U = 0$
$a/(1+a)$	$-a_2 < a < -a_1$	Between roof and vortex core	$U(a) = -U_{vortex}(a) = -U_{a_2} \cdot \sqrt{a/-a_2}$
a	$\lvert a\rvert < a_1$	Viscous vortex core	$U(a) = U_{core}(a) = U_{a_1} \cdot a/a_1$
$a+a^3/2$	$a_1 < a < a_2$	Vortex, above the core	$U(a) = U_{vortex}(a) = U_{a_2} \cdot \sqrt{a/a_2}$
$a+a^3/2$	$a_2 < a < a_3$	Transition region	$U(a) = U_{transition}(a) = \frac{U_{\max} \cdot 2 \cdot (a/a_{\max})}{1+(a/a_{\max})^2}$
$a+a^3/2$	$a_3 < a$	Potential flow region	$U(a) = U_{potflow}(a) = U_{a_3}\sqrt{e^{\int_{a_3}^{a}\frac{-2}{(Rc/h)}dn'}}$

Table 1: Equations used to draw the composite velocity profile in Figure 2.5, where the parameters were estimated to be $a_1 = 0.2$, $a_2 = 1$, $a_3 = 2$, $a_{max} = 1.5$ and $U_{max} = 1.05\ U_M$. $U_{a_2} = U_{transition}(a_2)$, $U_{a_3} = U_{transition}(a_3)$, and $U_{a_1} = U_{vortex}(a_1)$.

2.8 Figures

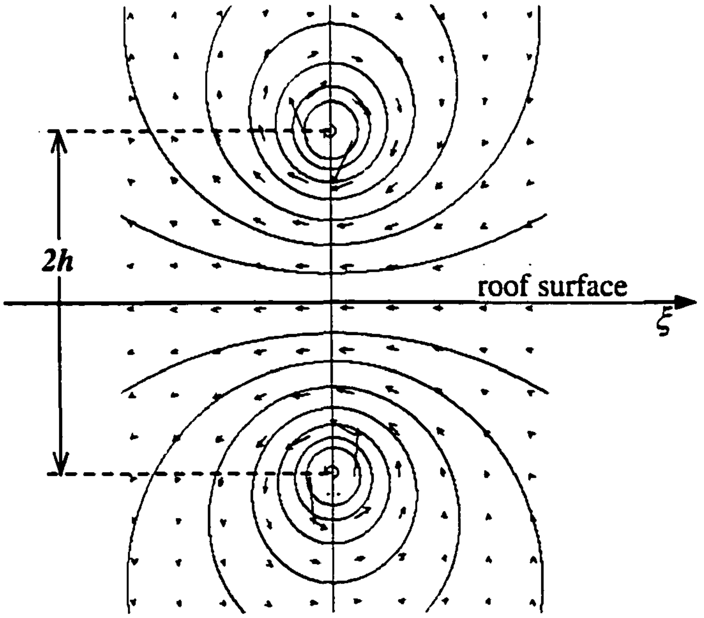

Figure 2.1: Counter rotating vortices in 2-D potential flow, showing streamlines and velocity vectors. The flat streamline is taken to be the roof surface in this model.

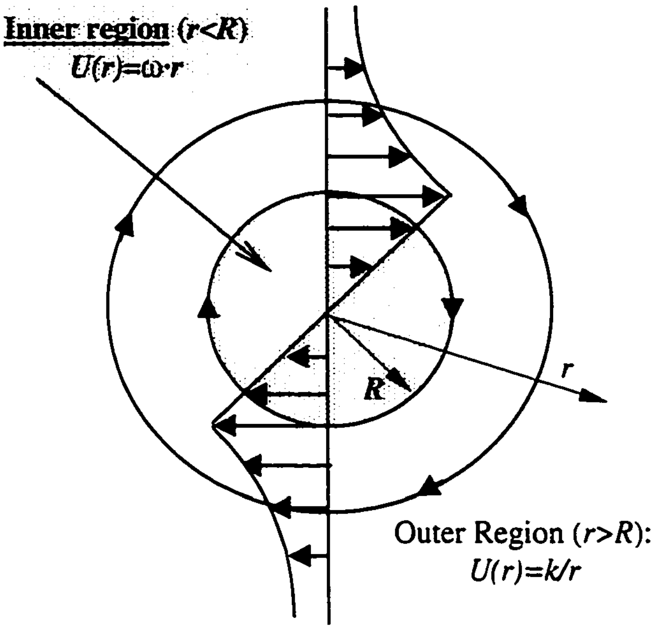

Figure 2.2: Rankine vortex showing velocity profile through core

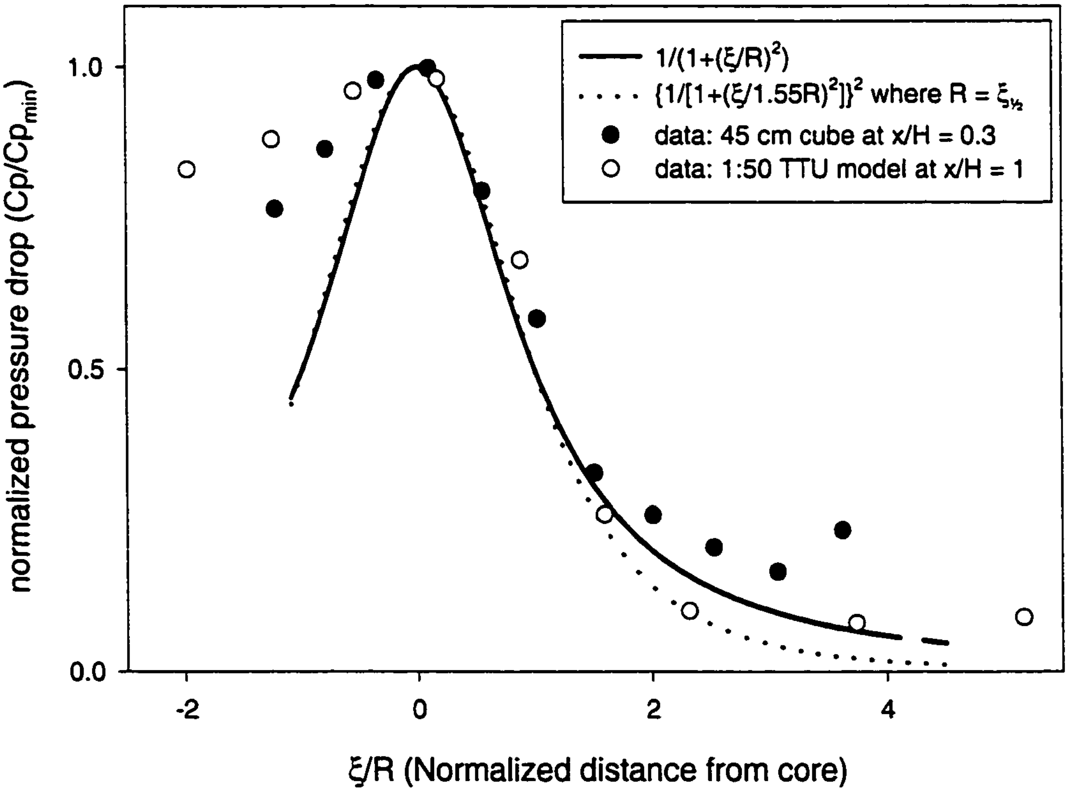

Figure 2.3: Normalized Cp distributions under the vortex, normal to the roof edge.

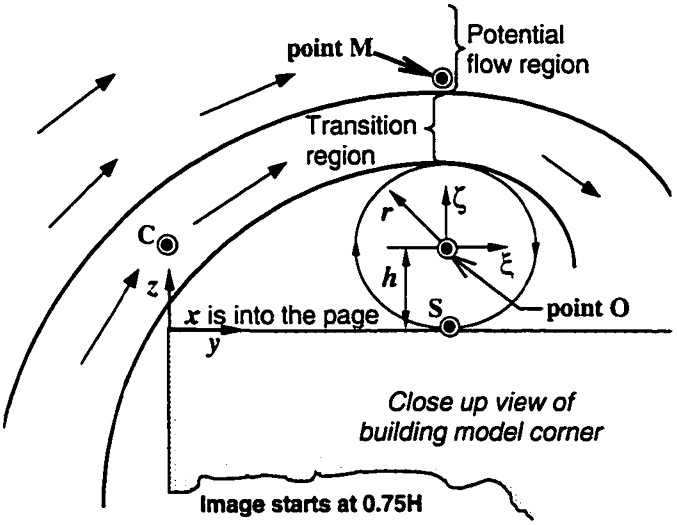

Figure 2.4: Two-dimensional depiction of vortex flow model

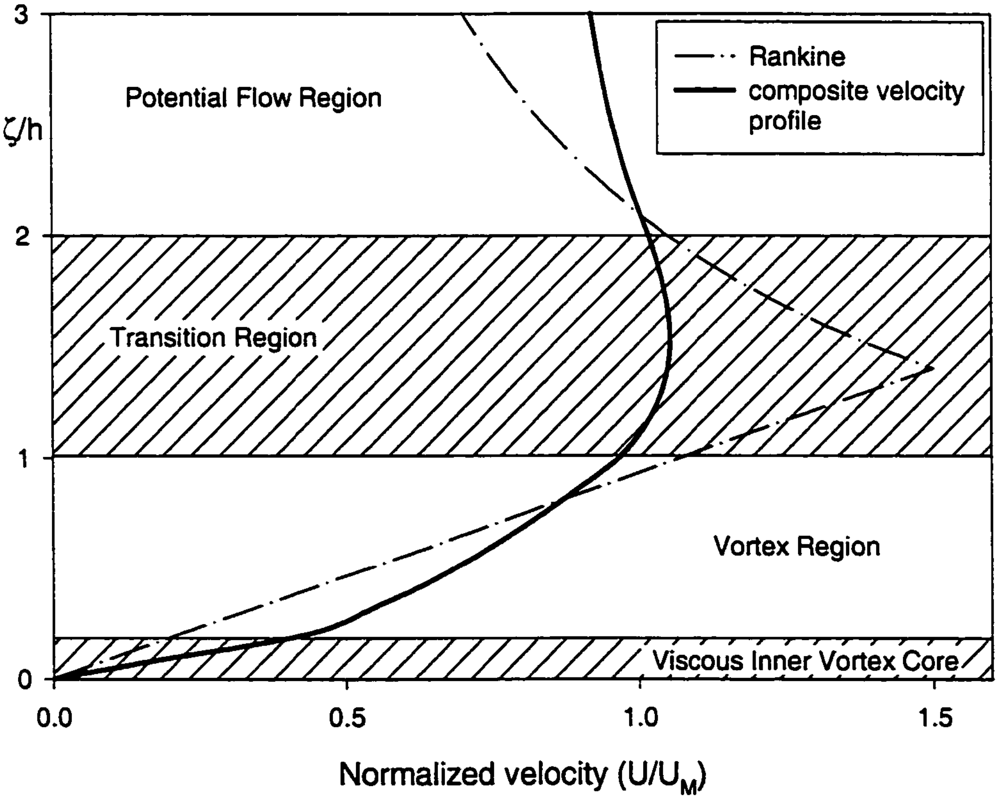

Figure 2.5: Velocity profile directly above vortex core through the points O and M

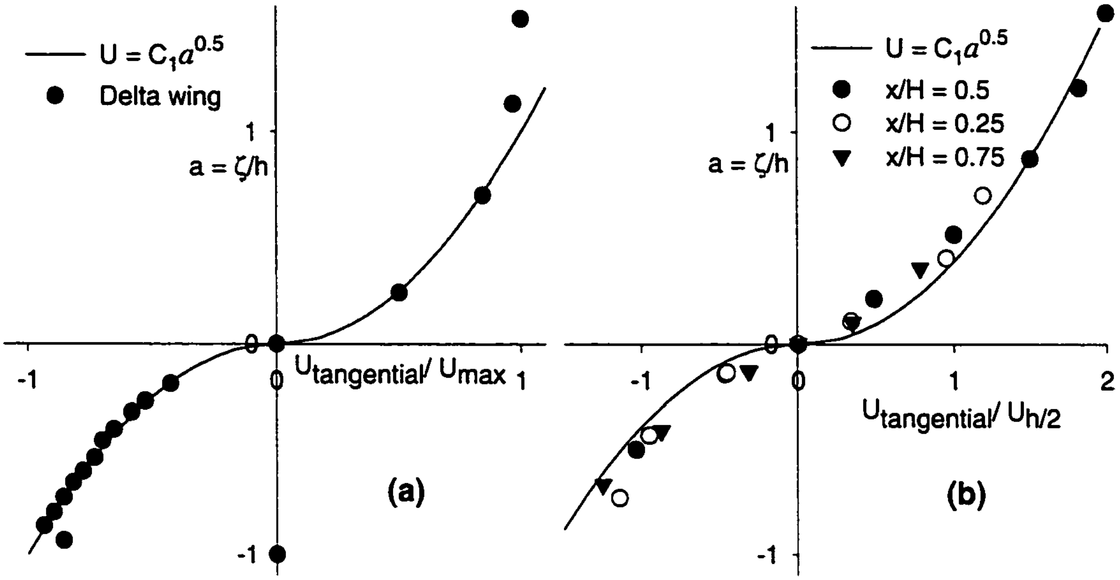

Figure 2.6: Mean velocity profiles from surface up through vortex core, with exponential curve fit, for: (a) 65°-sweep delta wing at 10° angle of attack (Rizzi, 1989) (b) several planes along a low-rise building model (Marwood, 1996)

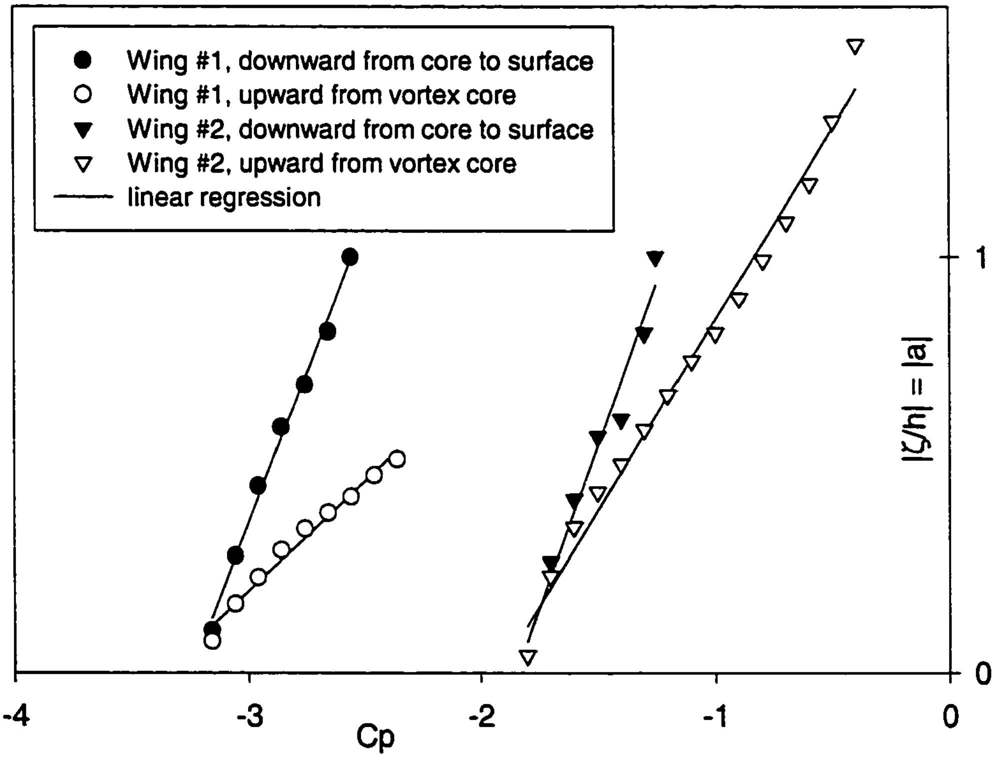

Figure 2.7: The nearly linear relationship between pressure drop and distance from the vortex core. Note differing pressure drop rates above and below the core. Data was taken along the line S-M through pressure contours from numerical simulations of delta wing vortices. Wing #1: Sweep = 75°, angle of attack = 50°, distance along chord = 60% (from Ekaterinaris and Schiff, 1994). Wing # 2: Sweep = 76°, angle of attack = 20.5°, distance along chord = 81% (from Kandil and Chuang, 1990).

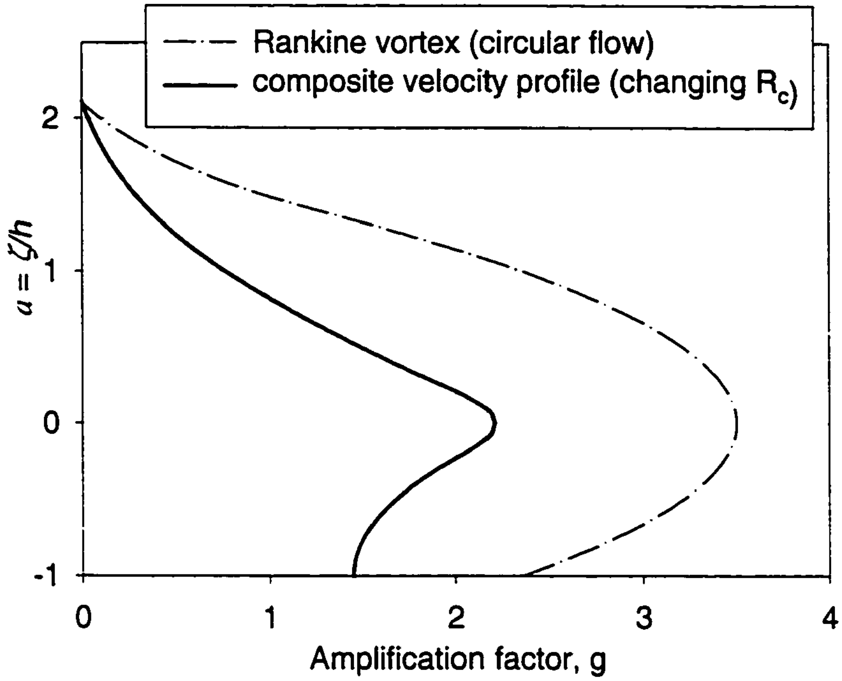

Figure 2.8: Vortex amplification factors, showing the effect of reduced curvature.

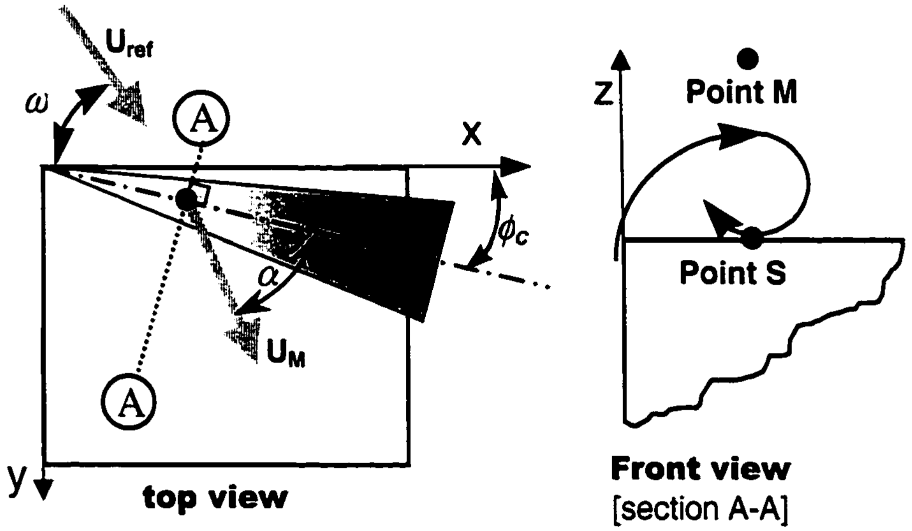

- Single conical vortex shown as shaded triangle (Second vortex not shown)
- Dashed line indicates the position of the vortex core's axis
- ω = wind angle of reference wind relative to the roof's leading edge
- α = wind angle relative to vortex core axis at the point M
- ϕ_C = vortex core angle with respect to the roof's leading edge
- the point S is on the roof surface directly beneath the vortex core
- the point M is above the shear layer, directly above the vortex core

Figure 2.9: Nomenclature for model of vortex mechanism. Note that the flow direction changes by an amount $\Delta\omega \approx \phi_C$ as it passed over the roof edge, so that $\omega \approx \alpha$.

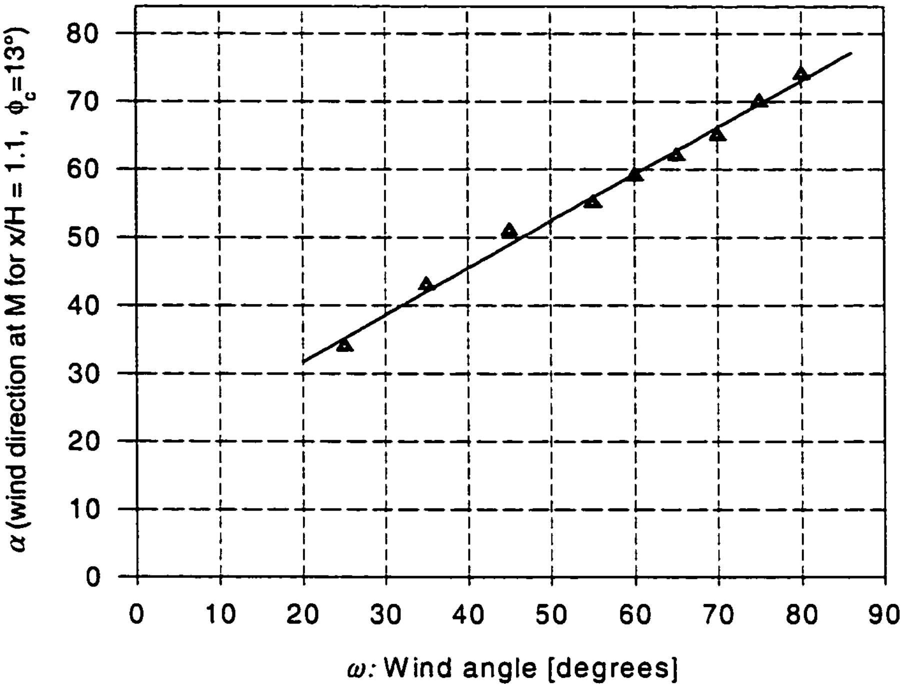

Figure 2.10: Wind direction above vortex core, relative to vortex core axis

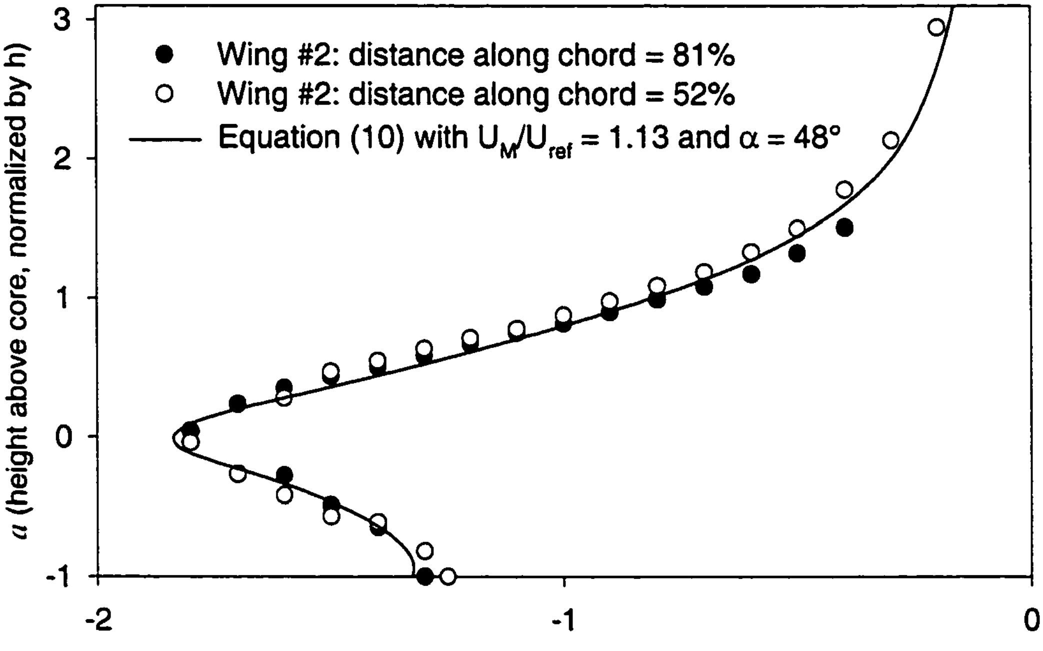

Figure 2.11: A comparision of the Cp(*a*) profiles predicted by Equation (10) and those for wing #2, a steady-state solution to the Euler equations for a 76° sweep delta wing at an angle of attack of 20.5° (from Kandil and Chuang, 1990)

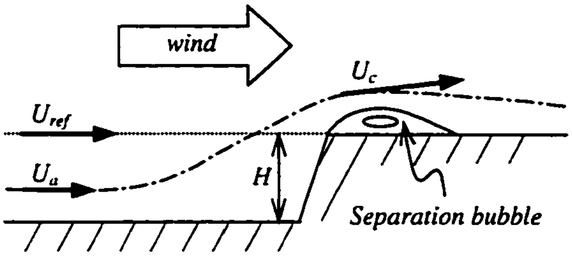

Figure 2.12: Flow over a steep escarpment

CHAPTER 3 EVALUATION AND IMPLICATIONS OF THE VORTEX MECHANISM MODEL

Most of the material in Chapter 3 has been submitted to "Wind and Structures", an international wind engineering journal. Some of this material also appears in abbreviated form in the proceedings of the 10th International Conference on Wind Engineering, which took place in Copenhagen in June 1999. (pg 1097-1104, Ed. Larsen, Larose, Livesey)

3.1 Introduction

This chapter uses experimental measurements to evaluate the vortex flow mechanism model developed in Chapter 2 and embodied in the Eqs. (2.12a) and (2.12b), which are reproduced here for simplicity. Many of the terms are illustrated in Fig. 3.1.

$$Cp_S(t) = \left(\frac{U_{spin}(t)}{\overline{U}_{spin}}\right)^2 \left(1 - \frac{\overline{U}_M^2}{\overline{U}_{ref}^2}\left[1 + \sin^2(\alpha(t)) \cdot g(t)\right]\right) \tag{3.1a}$$

$$\overline{Cp}_S = \left(1 - \frac{\overline{U}_M^2}{\overline{U}_{ref}^2}\left[1 + \sin^2(\overline{\alpha}) \cdot g(\overline{\omega})\right]\right). \tag{3.1b}$$

The quantity U_{spin} is the speed at which the vortex rotates, and is considered to be linked directly to the flow speed directly outside of the separated flow zone, such as at the points M or C.

The reasoning behind this model can be summarized as follows:

- Cp_M is assumed to be determined uniquely by the flow velocity at the point M,

$$\overline{Cp}_M = 1 - \frac{\overline{U}_M^2}{\overline{U}_{ref}^2}$$

- The pressure minimum at the vortex core can be calculated from the radius of curvature and the tangential velocity through the vortex using the equation

  $\frac{dP}{dn} = \frac{\rho U^2}{R_c}$ where *n* in a unit normal to the curving flow streamlines.

- The mechanism by which the high suction at the core is partially transferred to the roof surface is as follows: The radius of curvature increases much more rapidly beneath the core than above it, because the roof forces the streamlines beneath the vortex to flatten out quickly. As a result, some of the very low pressure at the core is passed on to the surface. This mechanism is quantified in the calculation of *g*, which is reviewed briefly later in this chapter.
- The faster the component of wind normal to the vortex core ($U_M \cdot \sin(\alpha)$), the faster the vortex spins, so the greater the pressure drop to the core and to the surface for a given value of *g*:

$$C\overline{p}_M - C\overline{p}_S = \frac{\overline{U}_M^2}{\overline{U}_{ref}^2} \cdot \sin^2(\overline{\alpha}) \cdot g(\overline{\omega})$$

Since the flow speed at M controls both Cp_M and the lower value of Cp_S simultaneously, the vortex can be seen as an amplifier of the velocity related pressure drop at M. For this reason, the term '*g*' is referred to as the amplification factor.

The experiments used to assess how well this model explains known vortex behaviour are described below.

3.2 Experimental procedures

3.2.1 Configuration of Apparatus

Simultaneous measurement of surface pressures and flow velocities was performed in the CSU Meteorological Wind Tunnel. In some instances, flow images were recorded concurrently.

This flow visualization was performed using a laser light sheet and digital image acquisition as described in Chapter 1.

A 1:50 scale model of the TTU field site low-rise building was used for tests in the simulated ABL developed by Ham and Bienkiewicz (1998). The pressure tap layout for the 1:50 model is given in Fig. 3.2. In order to provide a suitably large vortex during the visualization, the light sheet was positioned at x = 137mm. This corresponds to x/H = 1.72, where x is the distance along the leading edge from the apex, and H is the building model's height.

Following the work presented in Chapter 2, the pressure transducer system was upgraded to allow for more simultaneous pressure taps. The 0.5mm diameter taps on the WERFL model were connected to a 48-channel Pressure Systems Inc. (PSI) "ESP48" pressure sensor transducer unit mounted inside the model. The restrictor tubes were redesigned for use with the PSI transducers, and provided a linear phase shift and a gain of 1.0 +/- 0.1 out to 200 Hz. A restrictor cut-off at 200 Hz was chosen in this case because the pressures can be recorded at a maximum frequency of 480Hz per tap because of the transducer settling time. Since all 48 signals exit the transducer on the same line, there was no possibility of low-pass filtering the signals electronically.

Velocities were measured using model 1210 single wire and model 1241 x-wire hot-film probes from Thermal Systems Inc. (TSI) connected to TSI model 1050 constant temperature anemometers. A typical arrangement was to place an x-wire upstream and another x-wire either above the leading edge (the point C) or directly above a selected pressure tap. All probes were aligned with the local mean flow vector. Tests were performed to ensure that the glycerine smoke used for visualization did not affect the mean or rms velocity measurements.

Time series of 50 seconds in duration (≈ 42 minutes at full scale) were typically recorded for the pressure/velocity data. When images were also recorded, the data sequences were still limited to 6 seconds in duration due to the considerable memory requirements of real-time image storage.

The wind tunnel free stream velocity was typically set at 8 m/s at building height. This provided an adequate pressure signal, while still leaving enough smoke in the visualization plane for flow structures to be discerned in the digital images.

A single TTL switch triggered not only data acquisition, but also a precisely timed LED sequencer placed inside the Plexiglas mode. This was used to ensure synchronization between images and pressures. The restrictor tubing and the analog filters also introduce delays which were measured and corrected for during post processing.

3.2.2 Conditional Sampling

One of the main conclusions from examining the vortex image sequences is that the vortex changes position and size rapidly and considerably in turbulent flow. A good deal of this motion is attributable to changes in the local wind direction, because the vortex core angle (ϕ_c) is a function of ω (recall Fig 1.10). As will be shown in Chapter 4; there is also random scatter in ϕ_c about the mean for any given instantaneous wind direction (Fig 4.4). Eq. (3.1b) predicts the surface pressure at a point beneath the moving vortex core, based on the flow velocity directly above the moving vortex core. To validate this equation, simultaneous flow velocity and surface pressure measurements are required along the ζ-axis. Since ϕ_c moves somewhat randomly, so does the ζ-axis, which makes it impossible to take measurements at the points M and S with a single stationary probe or tap.

This problem was overcome by using conditional sampling. By simultaneously measuring the pressures at every tap in a given row, the location of the vortex could be ascertained, since the core is always above the location of maximum suction. The x-wire probe was positioned above a target tap, one with a high likelihood of having the peak suction. By selecting only those pressure and velocity measurements in the time series when the target tap had the lowest pressure in the row, a discontinuous time series of U_M and Cp_S was extracted from the full time series. Such conditionally sampled time series were used to generate all of the plots in this chapter.

3.2.3 Selection of the point M

The correlation between the flow speed along the ζ-axis above a target tap and the pressures measured by that target tap reaches a maximum just above 3 times the mean core height, $z = 3\bar{h}$ (Fig. 3.3). Since the correlation drops off quickly for $z < 3\bar{h}$, the $U_M(t)$ velocity measurements used to assess the validity of Eq. (3.1a) were taken at $z \approx 3.5\bar{h}$, where the correlation coefficient is typically 0.8. Another reason to place the probe at $z > 3\bar{h}$ is that the probe was observed to alter the location of the vortex core when placed at $z < 2.5\bar{h}$, moving the mean vortex position closer to the roof edge.

This shift in mean vortex position due to probe interference does not explain the loss of correlation for $z_M < 3\bar{h}$, however, because the conditional sampling process ensures that the vortex core is above the target tap and below the hot film for the data used in Fig. 3.3. One possible explanation is that the loss of correlation between U_M and Cps is due to changes in the vortex core height. It is known that the vortex height for a given ϕ_c can vary as much as 50% from the mean (Fig. 1.11a). If the velocity is being measured, for example, at twice the mean core height, then a larger than average value of $h(t)$ will produce a considerable drop in the measured velocity (see Fig. 3.4). Without some knowledge of $h(t)$, this drop in velocity is indistinguishable from a decrease in local velocity. (The point 'M', when located at $z = 3.5\bar{h}$ as shown in Fig. 3.4, will likewise suffer some inaccuracy in U_M as a result of changes in $h(t)$, but it is expected to be less severe than for $z < 3\bar{h}$.) This uncertainty about $h(t)$ imposes on the velocity signal random fluctuations that are unrelated to the overall flow speed at the roof edge, resulting in a loss of correlation.

3.3 Results

3.3.1 Velocity and curvature profiles.

The quantity g is defined in Chapter 2 as $g(t) = g_s \cdot I_\delta(t)$, where I_δ is a delta function which is 0 when the vortex is absent, and g_s can be calculated by the equation

$$g_s = 2\int_S^M \left(\frac{U}{U_M}(a)\right)^2 \cdot \left(\frac{R_C}{h}(a)\right)^{-1} da \qquad (3.2)$$

where $a = \zeta/h = (z-h)/h$ and R_c is the radius of curvature. In Chapter 2, the functions $U(a)/U_M$ and $R_c(a)/h$ were estimated from the results of numerical delta wing vortex studies and heuristic arguments, and a value for g_s of 1.5 was determined.

The mean velocity profile could not be reliably measured for $z < 1.5\bar{h}$ using the above facilities, since the hot-film probes cannot detect a flow reversal. The conditionally sampled mean velocity profiles do show reasonable agreement with the general shape of the estimated function for $z > 1.5\bar{h}$, however, as shown in Fig. 3.5. The sensitivity of Eq. (3.2) to variations in the velocity profile near the core was assessed, and showed that while the pressure at the vortex core depends greatly on the velocity profile, the surface pressure is less affected because of the expected relative symmetry of $U(a)$ above and below the core.

In the potential flow zone, values of $R_c(a)$ can be calculated from the velocity profiles since the flow is assumed to obey Bernoulli's equation. Since the pressure drop across the curved streamlines is prescribed by

$$\frac{dP}{dz} = \frac{\rho U^2}{R_c}, \text{ the radius of curvature can be estimated as } R_c \approx \frac{-2\cdot\Delta z\cdot U^2}{\Delta(U^2)}.$$

These calculations indicate that R_c can only be normalized by h close to the vortex core (perhaps only for $z < 3\bar{h}$), because outside of this region the local curvature is determined by the overall flow over the building regardless of the vortex size (see Fig. 3.6). Fig. 3.6 also indicates that R_c above the core increases roughly with z^3.

In and around the transition region, the radius of curvature has been estimated from flow visualization images. A sample image is provided in Fig. 3.7, where the simultaneously measured pressure profiles have been superimposed during post-processing. The building model is the black rectangle in the lower left, upon which the location of the pressure taps in row #5, illustrated by 11 vertical white lines, has also been superimposed. The roof of the model represents Cp = 0, and the bottom of the image corresponds to Cp = -2.4, as indicated. The order in which each of the coloured Cp profiles occurred is given by the correspondingly coloured numbering in the lower left of the image. (Also in the lower left is image number, in this case 168; the sequence includes a total of 240 images.)

By selecting points that follow the flow, such as those indicated by the dotted line in Fig. 3.7, and fitting a curve to those points, the curvature could be calculated and normalized by the vortex core height. Data points derived by this technique are shown in Fig. 3.8. The points can be fit by a curve of the form $R_c/h = B \cdot a^{1.5}$, but a fit of the form $R_c/h = a + B \cdot a^3$ has been used in Eq. (3.2) so that R_c approaches z in the limit as $a \rightarrow 0$ and varies with z^3 as a becomes large.

By varying the value of B, the sensitivity of g_s in Eq. (3.2) to variations in $R_c(a)/h$ was assessed, using the velocity profile depicted in Figs. 3.1, 3.4 and 3.5. Some results are presented in Fig. 3.9, showing that higher relative curvature (lower R_c/h) should produce greater values of g_s, and hence lower rooftop suction. The influence of curvature above the vortex will again be discussed once values of g, which have been indirectly measured using Eq. (3.1), have been presented.

3.3.2 Cp as a function of distance from the corner

A comparison of the data series for the different rows of taps in Fig. 3.5 also indicates that U_M increases with decreasing x. This trend is supported by LDA measurements above a 200mm cube, where it was reported that velocities in the conical vortex increase as the apex is approached (Minson and Wood 1992). The U_M vs. x relationship was quantified by further measurements taken between $z = 2h$ and $z = 3h$ at several x positions for $\omega = 55°$. Measurements were also taken at x = 15mm and x = 10 mm, using tap #10 as the target tap to determine vortex position. The results are shown in Fig. 3.10a. For x < 15mm, the vortex becomes quite small (h < 2.5mm); hence, the peak velocity is probably slightly higher than what is measured, since when the measurement volume of the x-wire is comparable to h^3, the wire will average velocities over a range of $\pm h/2$.

Substituting these $U_M(x)$ values into Eq. (3.1b) produces Fig. 3.10(b), where g = 0.65 has been used. This compares favourably with the measured increase in $|Cp_S|$ towards the corner. (Cp_S is determined for a given x by extracting the minimum Cp from the row of taps at x for each point in time, and averaging this new time series.) The pressure coefficient beneath the vortex core is expected to decrease according to an equation of the form $Cp_s = -C_1(x/H)^{-0.5}$ (Lin *et al.*, 1995), and such a curve is also shown for comparison.

Why would the velocity increase towards the apex? One possibility is that while the normalized curvature at M might remain constant, the absolute value of the curvature must decrease as $x \rightarrow 0$, and the vortex gets linearly smaller. Since the flow speed increases inversely with R_c in a potential flow region, U_M/U_{ref} would be expected to increase near the leading corner, or apex. So the smaller vortices would induce a greater absolute curvature at M, leading to a lower Cp_M. This analysis is also corroborated by the observation of increased suction beneath smaller vortices in smooth flow in Chapter 1, even though these vortices had identical R_c/h values at $z = 2.2h$.

3.3.3 Cp as a function of wind direction

3.3.3.1 Velocity components as a function of wind direction

Velocity profiles above a target tap were also measured for a range of wind directions, and the results are shown in Fig. 3.11a. The velocity above the vortex increases dramatically as the nominal wind angle is increased from 15° to 60°, at which point it levels off and begins to decrease (Fig. 3.11b). This helps to explain the general pattern of $\mathrm{Cp_S}$ vs. wind direction, which has a widely accepted worst case wind angle range of $55° < \omega < 60°$. Fig. 3.12 illustrates the maximum in $\mathrm{Cp_S}$ at $\omega = 60°$ for row # 3 (x/H = 1.1). Also shown for comparison is the value of $|\mathrm{Cp}(\omega)|$ for tap #39, which is located at $\phi = 7°$. (This 'single tap Cp vs. ω' plot is a type more commonly found in literature). Even though the mean vortex position is above the tap #39 at $\omega = 35°$ (see Fig. 1.10), and peak suction is always beneath the vortex core, the suction continues to increase for $\omega > 35°$, reaching its peak suction at $\omega = 60°$. This continued increase is due to the $\alpha(\omega)$ and $U_M(\omega)$ terms in Eq. $(3.1)^2$.

Even with the value of U_M reaching a maximum at $\omega = 60°$, however, Eq. (3.1b) predicts that if g is a constant, then the suction should continue to increase as $\omega \rightarrow 90°$. The $\mathrm{Cp_S}(\omega)$ curve calculated using Eq. (3.1b), with $\alpha(\omega)$ given by $\alpha = 18° + 0.7\omega$ (Fig. 2.10), U_M as in Fig. 3.11, and $g = 0.65$ is also shown in Fig. 3.12.

However, if $\omega(t)$ is measured $0.1H$ upstream of the leading edge, and Cp is plotted against $\omega(t)$ instead of mean wind direction, then the maximum suction does occur at $80° < \omega < 90°$, as shown in Fig. 3.13 (Letchford and Marwood 1997). This suggests that

---

[2] It will be shown in Chapter 4 how Eq. (1) can be applied to a single tap by using a transfer function.

Cp_S does indeed vary with $\sin^2(\alpha(t))$ for $\omega > 60°$. The fact that Cp does not drop off for instantaneous changes in wind direction from 45° to 75°, but does for a similar shift in mean wind direction, is in part attributable to an error in the quasi-steady (Q-S) assumption underlying Eq. (3.1a). Q-S theory assumes that an instantaneous change in wind direction has the same effect on the vortex as a long-term change in wind direction between the same angles. As we will see in Chapter 4, this is not the case for $\alpha(t) > 60°$, since the vortex is much more stable at low mean wind directions, and this translates into higher values of Cp_S for $\omega > 60°$ when $\bar{\omega} < 60°$. This suggests that peak suction events are related to stable vortices at momentarily high local wind angles. The issue of the duration of a wind direction shift is explored further in the final section of this chapter.

3.3.3.2 Amplification factor (g) as a function of wind direction

The mean value of g is expected to decrease as $\bar{\omega}$ approaches 90°, because flow visualization has shown that the vortex becomes increasingly unstable and intermittent. This accounts for the discrepancy between the measured Cp_S and that calculated using a constant g in Fig. 3.12. A function $g(\omega)$ can be calculated from the measured and calculated Cp_S curves in Fig. 3.12, and it is shown in Fig. 3.14. If a value of $g = 1.5$ is associated with a stable vortex, then an intermittency function $I(\omega)$ can be calculated from $g(\omega) = 1.5 \cdot I(\omega)$; this function is also displayed in Fig. 3.14.

Up to this point, I have focused upon the mean value equation, Eq. (3.1b). However, since the x-wire at M can be used to measure $\alpha(t)$ and $U_M(t)$, and $U_M(t)$ can be used for $U_{spin}(t)$, we can calculated the value of $g(t)$ for each point in the time series using Eq. (3.1a). Since the point M is being used to measure the 'spin' velocity, and U_M is a function of ω, Eq. (3.1a) becomes

$$Cp_S(t) = \left(\frac{U_M(t)}{\overline{U}_M(\omega(t))}\right)^2 \left(1 - \frac{\overline{U}_M^2(\omega(t))}{\overline{U}_{ref}^2}\left[1 + \sin^2(\alpha(t))\cdot g(t)\right]\right) \tag{3.3}$$

The calculation of $g(t)$ from Eq. (3.3) requires a division by $\sin^2(\alpha)$, which for low $\alpha(t)$ values can lead to large values of $g(t)$. As a result, it has been found to be more revealing to plot $\Delta Cp^N(t)$ vs. $\alpha(t)$, where $\Delta Cp^N(t)$ is given by

$$\Delta Cp^N(t) = \left(1 - Cp_S^N(t)\right)\cdot\left(\frac{\overline{U}_{ref}^2}{\overline{U}_M^2(\omega(t))}\right) - 1 \text{ with } Cp_S^N(t) = Cp_S(t)\cdot\left(\frac{\overline{U}_M(\omega(t))}{U_M(t)}\right)^2 \tag{3.4}$$

Such plots can then be compared with curves for $\sin^2(\alpha)\cdot g$ for different values of g, as in Fig. 3.15, where tap #39 is the target tap. This curve is for a nominal wind direction (ω_{nom}) of 55°, where the value of ω_{nom} is determined by the rotation of the wind tunnel's test section turntable.

For the plotted average in Fig. 3.15, the $\Delta Cp^N(t)$ time series was sorted by $\alpha(t)$ and then grouped; each point on the curve represents an average of 100 data points. Similar grouped-average curves were calculated for data from a range of ω_{nom} data series, and the results are shown in Fig. 3.16. These curves illustrate the aforementioned inaccuracy of the quasi-steady theory. In a truly quasi-steady situation, all of the averaged $\Delta Cp^N(\omega)$ points would fall on a common curve, regardless of ω_{nom}. Instead, the curves run alongside each other, so that, for example, for $\alpha(t) = 50°$, ΔCp^N ranges from 0.75 for $\omega_{nom} = 25°$ to 0.5 for $\omega_{nom} = 0.65$. The general mean trend evident in each ω_{nom} curve is, however, consistent with the quasi-steady expectation that as α increases, g decreases. Looking at how ΔCp^N intercepts the g = constant lines for $\omega_{nom} = 55°$, for example, we see $g(t)$ decrease from 1.1 near $\alpha(t) = 40°$ to 0.6 at $\alpha(t) = 75°$.

The calculation of ΔCp^N ought to theoretically remove the influence of local velocity fluctuations on $Cp_S(t)$, allowing the influence of $\alpha(t)$ and $g(t)$ on Cp to become evident. This is true in a general sense: In Fig. 3.16, it is seen that for $\alpha < 40°$, the fact that $\sin^2(\alpha(t)) \rightarrow 0$ forces ΔCp^N towards 0, while it is the falling value of $g(t)$ as $\alpha \rightarrow 90°$ that keeps $\Delta Cp^N(t)$ below 0.5. However, the calculation of $Cp^N(t)$ involves the division of $Cp_S(t)$ by $U_M^2(t)$, and the resulting correlation coefficient between $Cp^N(t)$ and $U_M(t)$ is typically 0.30. As a result, $g(t)$ still varies somewhat with U_M, and since U_M is a function of the wind direction, a spurious correlation is introduced between g and α.

To ensure that higher g values were not simply the result of the residual influence of U_M, and so to better isolate the effect of g on Cp, selected data with $0.9 < U_M/\overline{U}_M < 1.1$, and α in the range $\overline{\alpha} \pm 8°$ were used to calculate g for several nominal wind directions. The resulting $g(t)$ values and their associated row #3 Cp profiles (usually around 1000 data points) were sorted by $g(t)$, and consecutive groups of 50 were averaged to produce Fig. 3.17. The results show that not only are $|Cp_S|$ values greater for higher values of g (as would be expected from Eq. (3.3)), but that the Cp profile shape changes with g. As g becomes smaller, the profile becomes flatter, while for large g values, the transition from peak suction to low suction is very sudden.

The flow structures associated with these Cp profiles can be examined though the simultaneously recorded flow velocities, surface pressures and flow images. Some sample images are shown in Fig. 3.18, which have a similar format to Fig. 3.7. Two hot-wire probes are evident, one along the roof and the other above the leading edge at the point C, and flow velocity vectors for the latter probe have been superimposed. Image exposure times were a 125th of a second for (a) and (b), and a 250th of a second for (c) and (d). Mean flow velocity at the point C was 11.4 m/s, and is indicated by the grey circle around the top hot wire probe. The nominal wind angle is 45°, and the reference flow velocity is 8 m/s at roof height.

Instantaneous concurrent flow velocities at C normalize the Cp values for each time step, so that the plots represent

$$Cp^N_{tap}(t) = Cp_{tap}(t) \cdot \left(\frac{\overline{U_C}}{U_C(t)} \right)^2$$

The $Cp^N = -1.0$ line is shown in grey, and is labeled "instantaneous Cp = -1.0". The rooftop corresponds to $Cp^N = 0$, and the bottom of the image corresponds to $Cp^N = -2.1$, as indicated. The square of the velocity ratio used to "correct" Cp(*t*) is indicated in the lower left corner, along with the image number and the mean flow velocity at C during the image. For row #5 and $\omega = 45°$, $Cp^N = -1$ corresponds roughly to $g = 0.4$, and $Cp^N = -2.1$ corresponds roughly to $g = 1.9$.

Images (b) and (d), with $g > 1.5$, clearly display vortices above the peak suction locations, while images (a) and (c), with $g < 0.5$, show little or no evidence of reattachment. In general, a high value of g and the associated rapid pressure recovery for $\phi > \phi_C$ is seen in images with a distinct vortex and a clear reattachment point. Low g values are observed when there is either no vortex, or when there is a poorly defined vortex with a gradual pressure recovery and a reduced value of Cp_S.

3.4 Discussion of some Implications of the model

The extremely high y-direction pressure gradient associated with the strongest vortices could be a cause for concern from a design perspective, since the low reattachment suction may pressurize the bottom surface of a roofing paver, while the top surface experiences the full suction of the worst-case high-g Cp_S. The high gradient may also cause an overturning moment for roof-mounted items.

The link between the highest suction vortices and a firm and immediate re-attachment also suggests that inhibiting the flow reattachment can mitigate the worst vortex induced rooftop suctions.

The changes in vortex reattachment occur very quickly ($fH/U > 25$), so that they are difficult to observe on a 1:50 scale model with a camera frame rate of $f = 60$Hz ($fH/U = 6$). Using a camera shutter speed of 250 Hz (fH/U=25) helps, but future tests should be conducted on a larger model to slow down the phenomenon.

A normalized frequency of $fH/U > 25$ implies a length scale smaller than the circumference of the vortex. Data recorded for bubble separation shows that for constant levels of turbulence intensity (ranging from 8% to 15%), increasing the integral scale (L_x) had no effect on mean suction until L_x exceeded the re-attachment length (Li and Melbourne 1995), which is approximately equal to the vortex circumference. At this point, the mean suction decreased. Melbourne has pointed out that the higher suction, smaller separation zones are instigated by small-scale turbulence, which increases the entrainment in the shear layer (Melbourne 1993). Turbulence or velocity fluctuations larger than the separation zone would be expected to increase the speed of the vortex rotation, rather than affect the entrainment. This would in turn increase the peak and rms suction, since each gust is amplified by the curving separated flow, but would reduce entrainment, and so reduce curvature, thus reducing the mean suction. This is in fact what has been observed (Li and Melbourne 1995).

As a result, the simulation of all scales of turbulence could be important in reproducing suction beneath the conical vortex. Vertical fluctuations of a size smaller than the vortex circumference are expected to influence entrainment, and so control the shape of the re-attachment zone, though some portion of turbulence at this scale is generated by the leading edge itself. Lateral fluctuations larger than the vortex circumference, but smaller than the building length, are expected to accelerate the vortex spin, without changing its position or size. (This would explain why "fast and large" wind direction changes (short duration, large angle change), in which the wind briefly flows normal to the leading edge, have been observed to produce suction peaks (Zhao, et al. 2000)). Lateral fluctuations larger than the building will cause the vortex to move its position, and vortex motion significantly affects rms Cp values near the vortex, especially at the point of flow re-attachment. Longitudinal or stream-wise gusts of all scales larger than the vortex circumference will influence vortex rotation speed. Larger scales could also be associated with the "washout" phenomena, where there is no reattachment and the vortex disappears momentarily.

Note that the vortex circumference increases with distance from the apex. This suggests that as the apex is approached, it becomes increasingly important to simulate smaller and smaller scales of turbulence in order to reproduce peak pressures. A fairly small gust in the *y* direction will last long enough to spin the vortex around faster and transfer a momentary low core suction to the surface.

3.5 Conclusions

A curvature based model for the relationship between local flow speed and roof surface pressure has been developed and evaluated. Measurements indicate that the increase in flow speed directly above the vortex at the point M accounts for the known increase in suction towards the roof corner, as x → 0.

The suction beneath the vortices is also known to reach a maximum near a wind angle of 60°. Three factors are shown to contribute to this peak:

- The flow speed at M reaches a maximum for a wind direction near 65°.
- The flow component normal to the vortex core at M increases as the wind becomes more normal to the roof's edge ($\omega \rightarrow 90°$); this is expected to spin the vortex more quickly.
- The likelihood of a solid vortex reattachment decreases as $\omega \rightarrow 90°$.

The presence of a solid reattachment is shown to be associated with a larger than average pressure drop across the vortex (which translates into a high value of the parameter g), and can be identified by a more sudden drop in suction between the vortex core and the reattachment point. The flow model predicts that high values of g are associated with greater curvature above the vortex, and this is confirmed by the flow visualization.

The value of g was estimated at 1.5 in Chapter 2 for a solid reattachment, based upon some assumptions about the curvature and velocity profiles across the vortex core. While the curvature and velocity profiles could only be directly verified above the vortex core, indirect measurements of g indicate that $g = 0$ for no reattachment and $g = 1.5$ for a solid reattachments are good estimates.

The flow model suggests that all scales of turbulence play a role in determining the suction beneath the vortex, either by controlling the nature of the flow reattachment or by determining the speed at which the vortex spins. In the context of this model, further study of the connection between the components of turbulence at the point M and the upstream flow conditions should provide additional insight into the manner in which upstream flow conditions can control suction beneath rooftop conical vortices.

3.6 References

Ginger, J. D., and Letchford, C. W. (1992), "Peak wind loads under delta wing vortices on canopy roofs", *J. Wind Eng Ind. Aerodyn.*, **41-44**, 1739-1750.

Ham, H. J., and Bienkiewicz, B. (1998), "Wind tunnel simulation of TTU flow and building roof pressure", *J. Wind Eng Ind. Aerodyn.*, **77 & 78**, 119-133.

Letchford, C. W., and Marwood, R. (1997), "On the influence of v & w component turbulence on roof pressures beneath conical vortices", *J. Wind Eng Ind. Aerodyn.*, **69-71**, 567-577.

Li, Q. S., and Melbourne, W. H. (1995), "An experimental investigation of the effects of free-stream turbulence on streamwise surface pressures in separated and reattaching flows", *J. Wind Eng. Ind Aerodyn.*, **54/55**, 313-323.

Lin, J.-X., Surry, D., and Tieleman, H. W. (1995), "The distribution of pressure near roof corners of flat roof buildings", *J. Wind Eng. Ind. Aerodyn.*, **56**, 235-265.

Marwood, R., and Wood, C. J. (1997), "Conical vortex movement and its effect on roof pressures", *J. Wind Eng Ind. Aerodyn.*, **69-71**, 589-595.

Melbourne, W. H. (1993), "Turbulence and the Leading Edge Phenomena", *J. Wind Eng Ind. Aerodyn.*, **49**, 45-64.

Minson, and Wood (1992), "Investigation of separation bubbles and inclined edge vortices above model buildings using laser doppler anemometry", *11th Australasian fluid Mechanics Conference*, University of Tasmania, Australia.

Saathoff, P. J., and Melbourne, W. H. (1989), "The generation of peak pressures in separated/ reattaching flows", *J. Wind Eng Ind. Aerodyn.*, **32**, 121-134.

Zhao, Z., Sarkar, P. P., and Mehta, K. C. (2000), "Wind flow characteristics and their loading effects on low-rise building roofs", *(submitted to) Journal of Wind and Structures.*

3.7 Figures

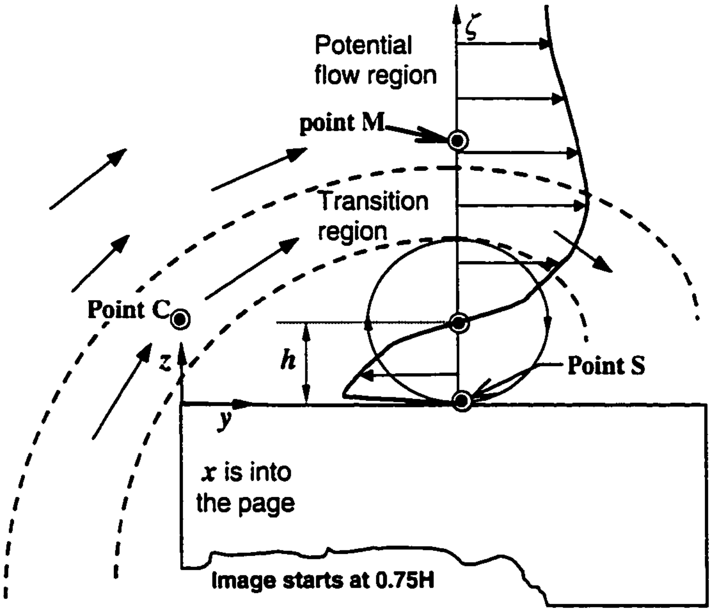

Figure 3.1: Illustration of the terms used in the flow model equations. Also shown is the expected velocity profile through the vortex core. $\zeta = 0$ at the vortex core.

row #1: x=30mm

tap#	y,mm	ϕ tap
9	8	14.9
10	11	20.1
11	14	25.0

row #2 x=60mm

tap#	y,mm	ϕ tap
12	8	7.6
13	11	10.4
14	14	13.1
15	17	15.8
16	20	18.4
17	25	22.6
18	30	26.6

row #3: x=87mm

tap#	y,mm	ϕ tap
38	5	3.3
39	10	6.6
40	15	9.8
41	20	12.9
42	25	16.0
43	30	19.0
44	35	21.9
45	45	27.3
46	55	32.3
47	65	36.8
48	85	44.3

row #4: x=112mm

tap#	y,mm	ϕ tap
32	5	2.6
33	10	5.1
34	15	7.6
35	20	10.1
36	25	12.6
37	30	15.0

row #5: x=137mm

tap#	y,mm	ϕ tap
19	5	2.1
20	10	4.2
21	15	6.2
22	20	8.3
23	25	10.3
24	30	12.4
25	35	14.3
26	45	18.2
27	55	21.9
28	65	25.4
29	85	31.8
30	135	44.6
31	175	51.9

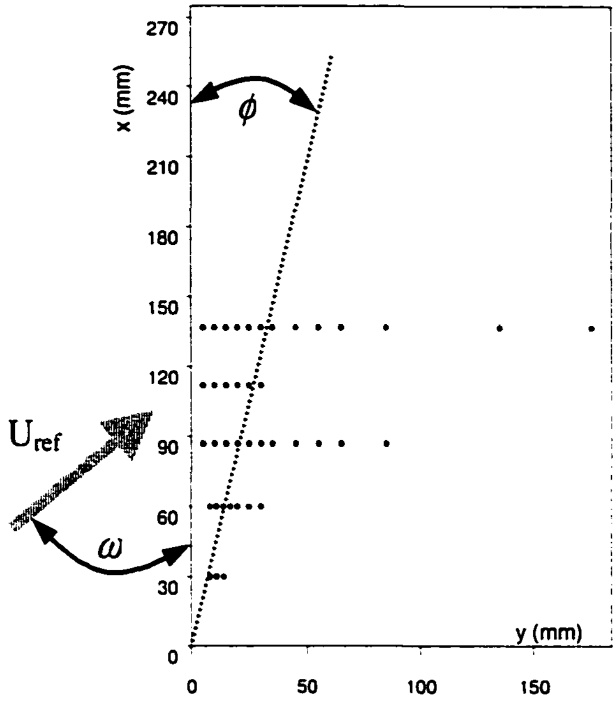

Figure 3.2: Top view of 1:50 model of TTU WERFL building showing position and numbering of roof-top pressure taps used in this experiment

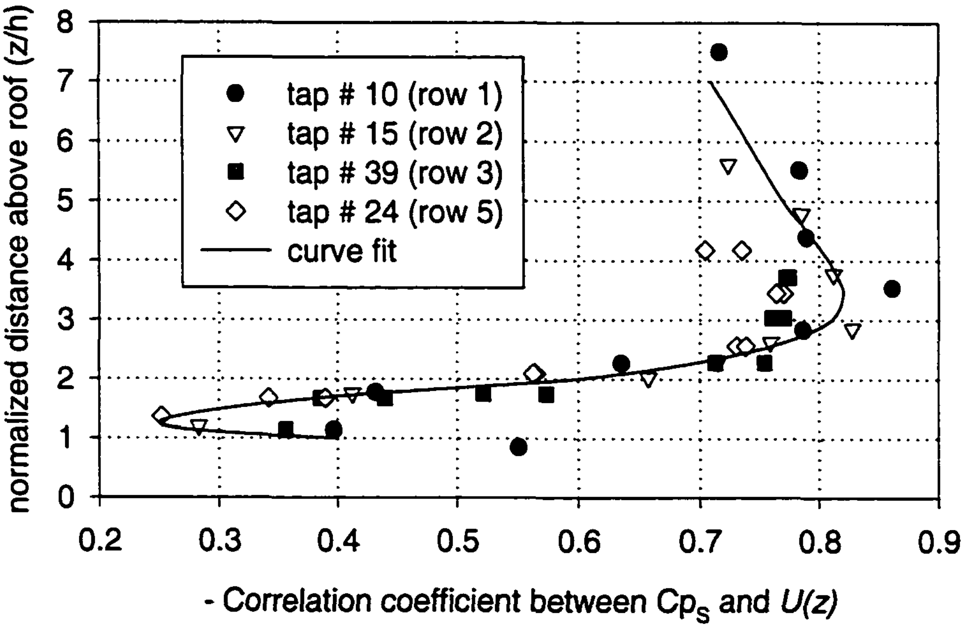

Figure 3.3: Correlation between surface pressure and flow velocity above various target taps for a wind angle of 55°.

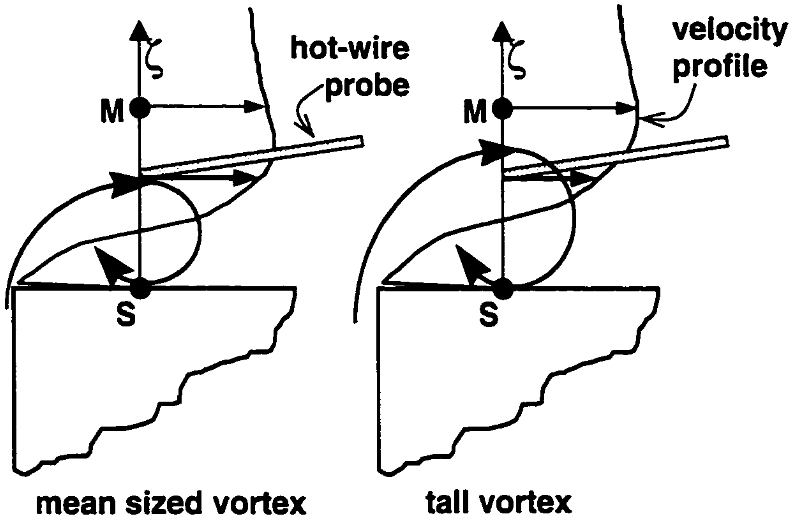

Figure 3.4: Effect of hot wire position on total velocity

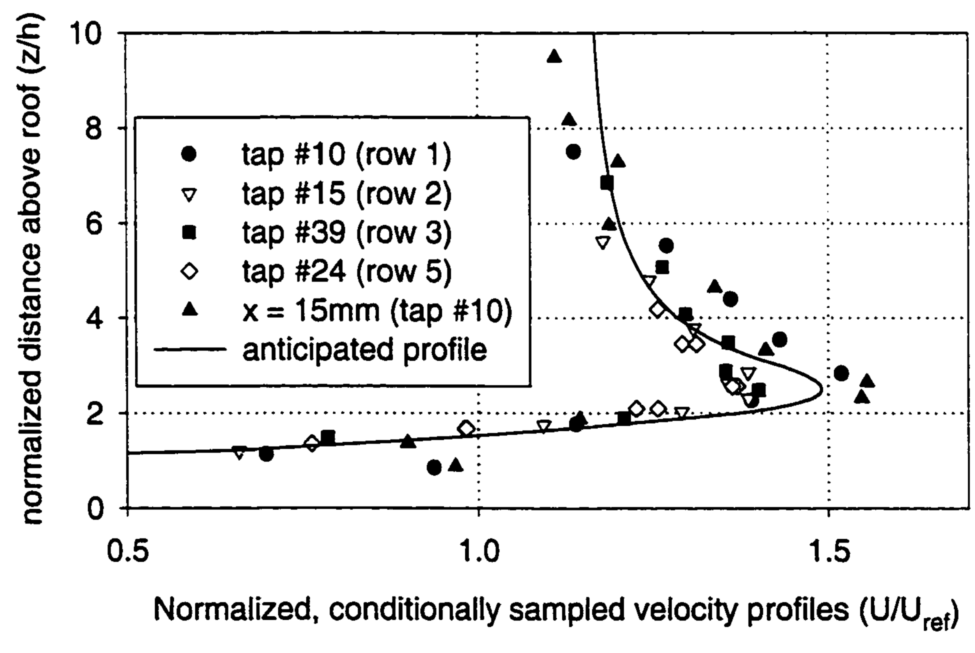

Figure 3.5: Normalized velocity profiles above various target taps for $\omega = 55°$.

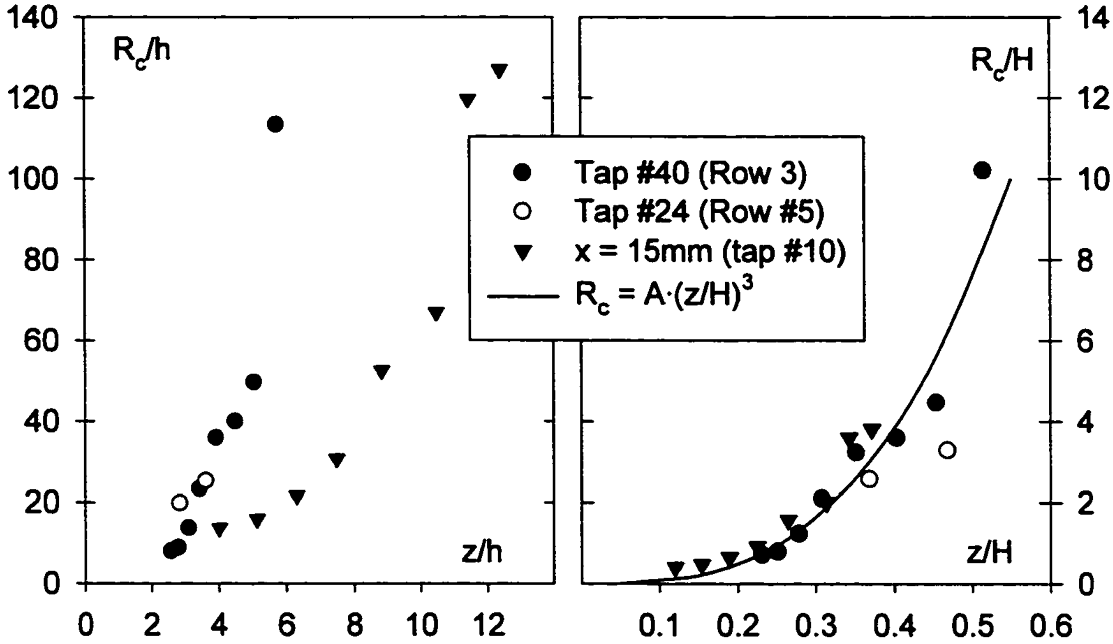

Figure 3.6: Radius of curvature (R_c) for several target taps, as a function of height above the roof. R_c was calculated from velocity profiles.

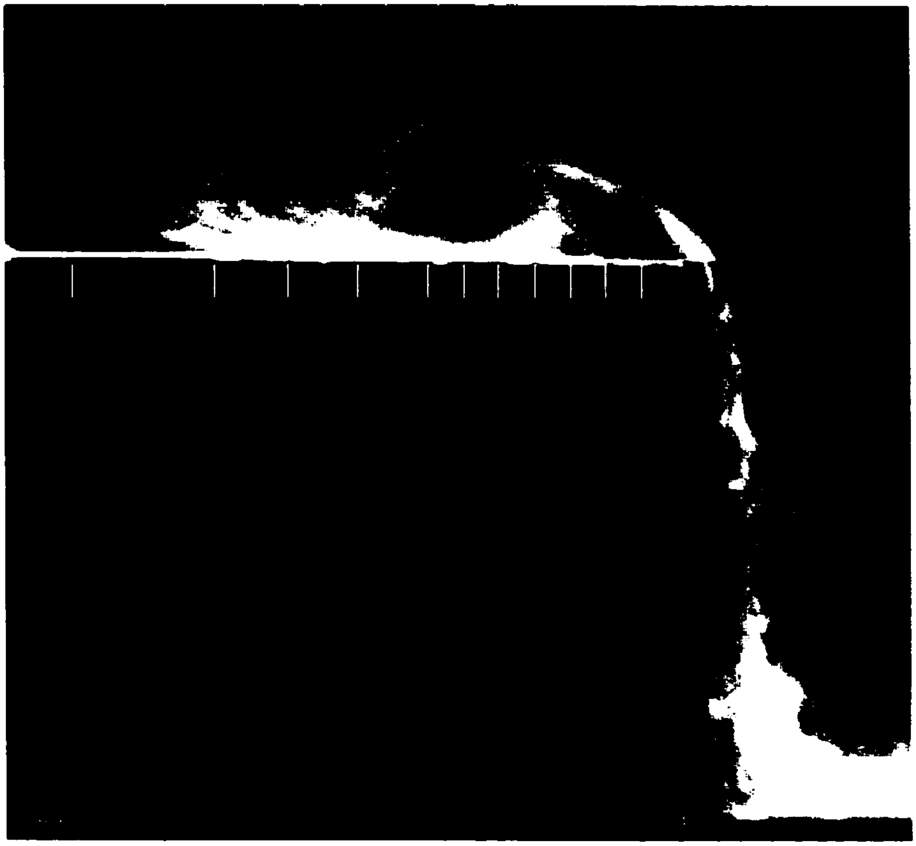

Figure 3.7: Vortex image in smooth flow for $\omega = 45°$, with tap locations and pressure profile superimposed. The dotted yellow line was used to calculate curvature.

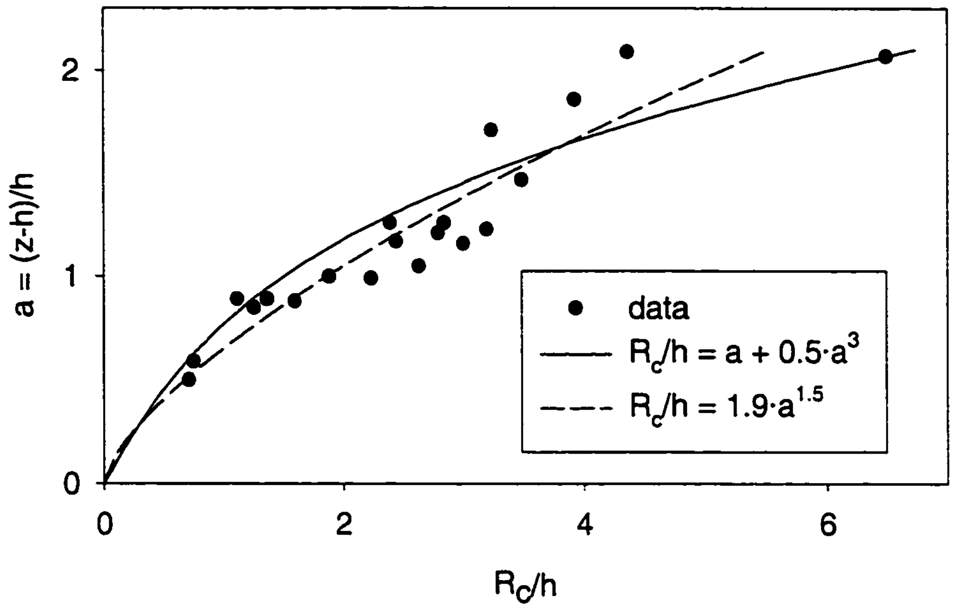

Figure 3.8: Radius of curvature in the transition region, as determined from flow visualization for smooth flow and turbulent flow when $1.0 < g_s < 1.5$

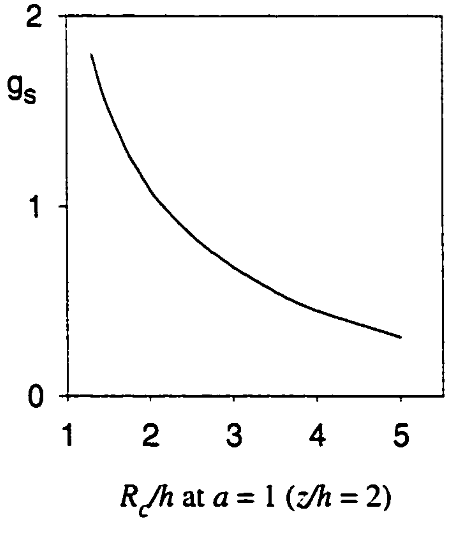

Figure 3.9: Change in vortex amplification factor with curvature above the core, as indicated by R_c/h at $a = 1$. Calculations are based on $R_c/h = a + B \cdot a^3$.

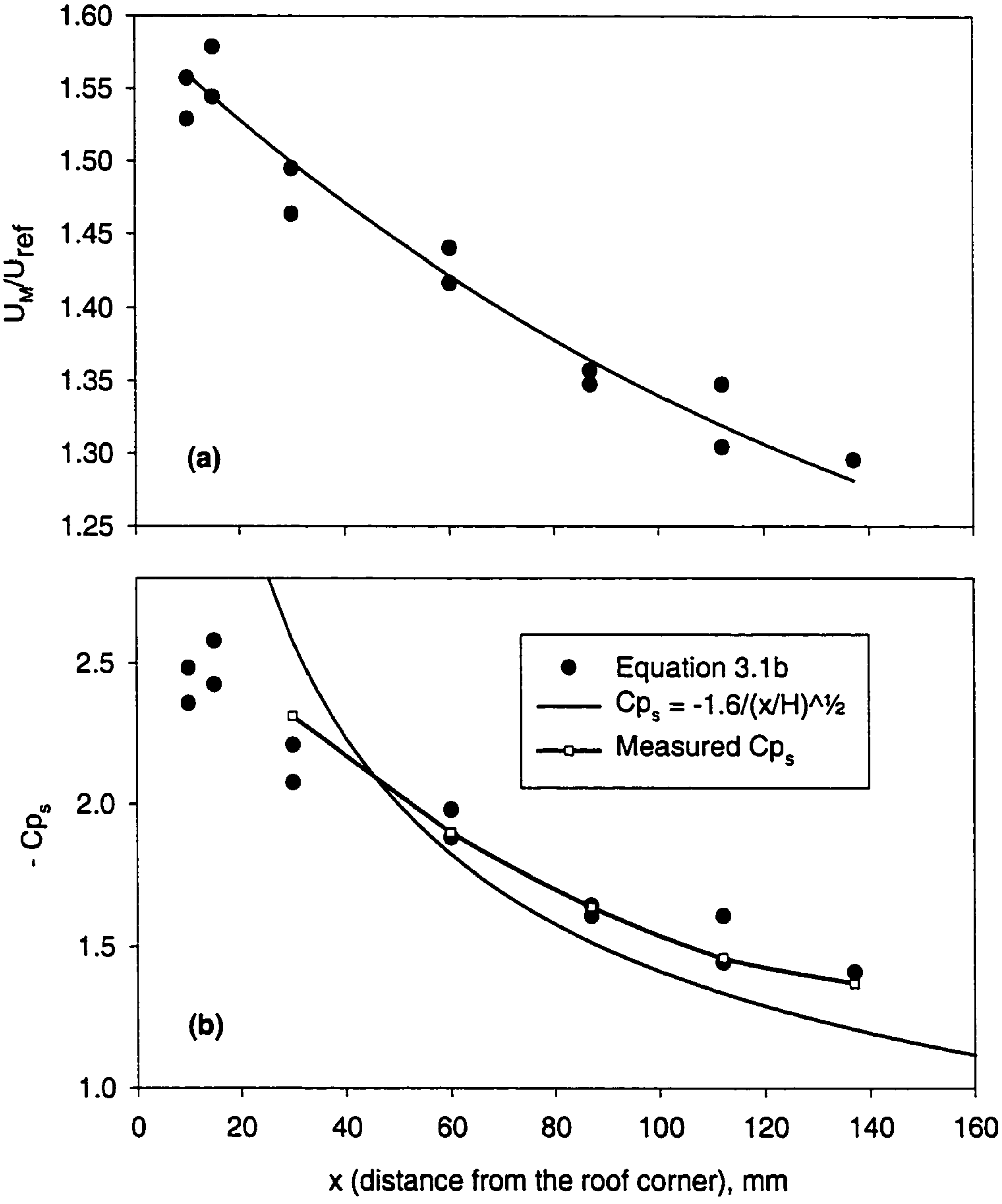

Figure 3.10: Increase in velocity and surface pressure coefficient towards the roof corner. U_M was measured at $z = 3h$ in this case. $\omega = 55°$.

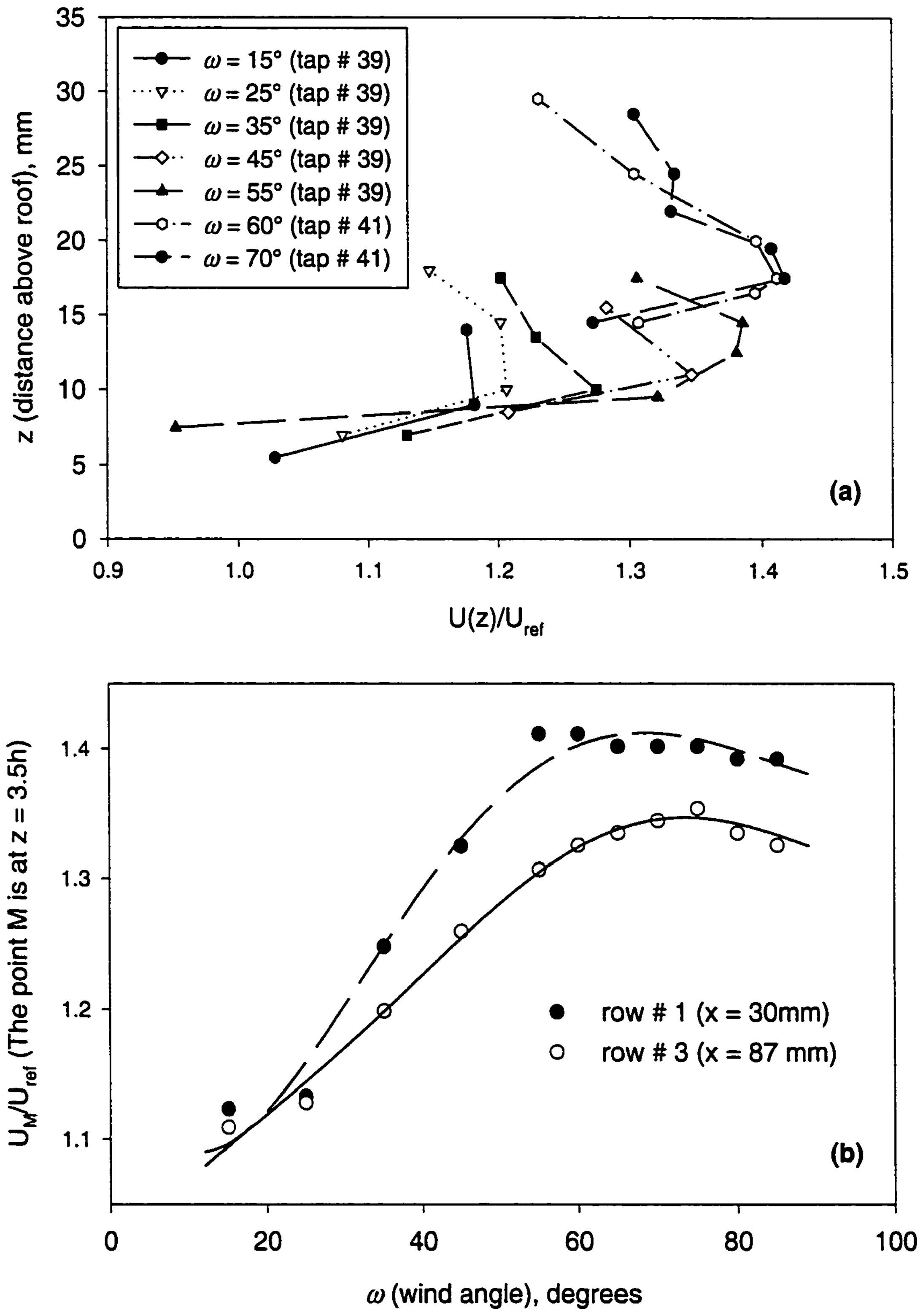

Figure 3.11: Effect of wind angle upon the velocity above the vortex

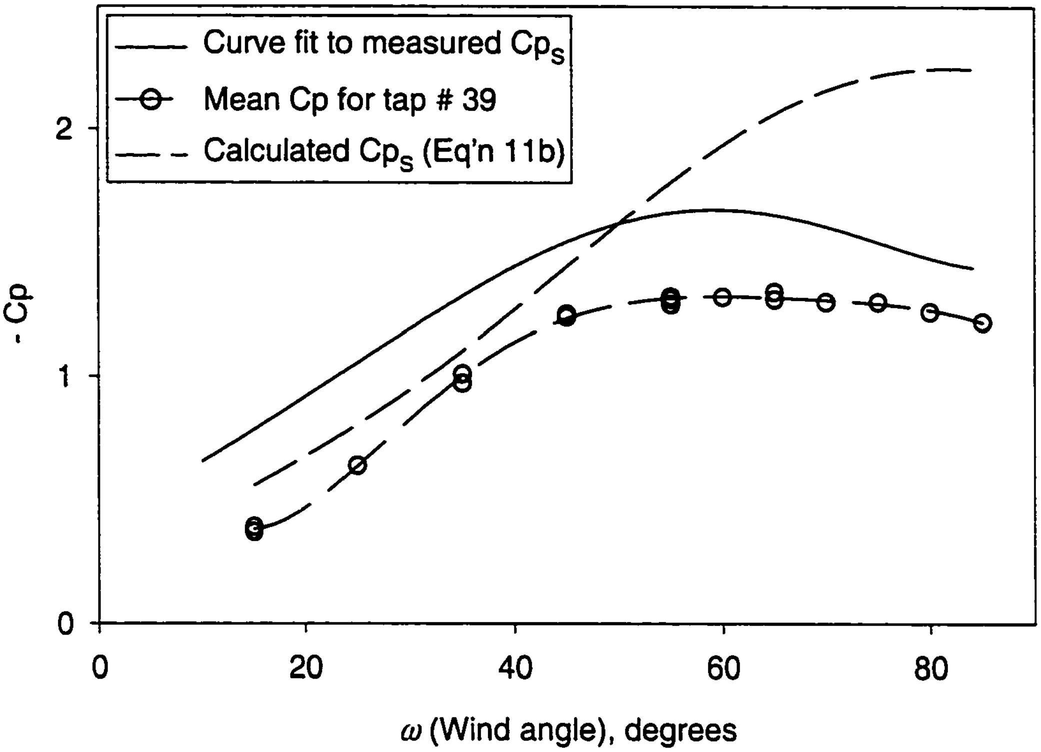

Figure 3.12: Mean Cp beneath the vortex for tap row #3

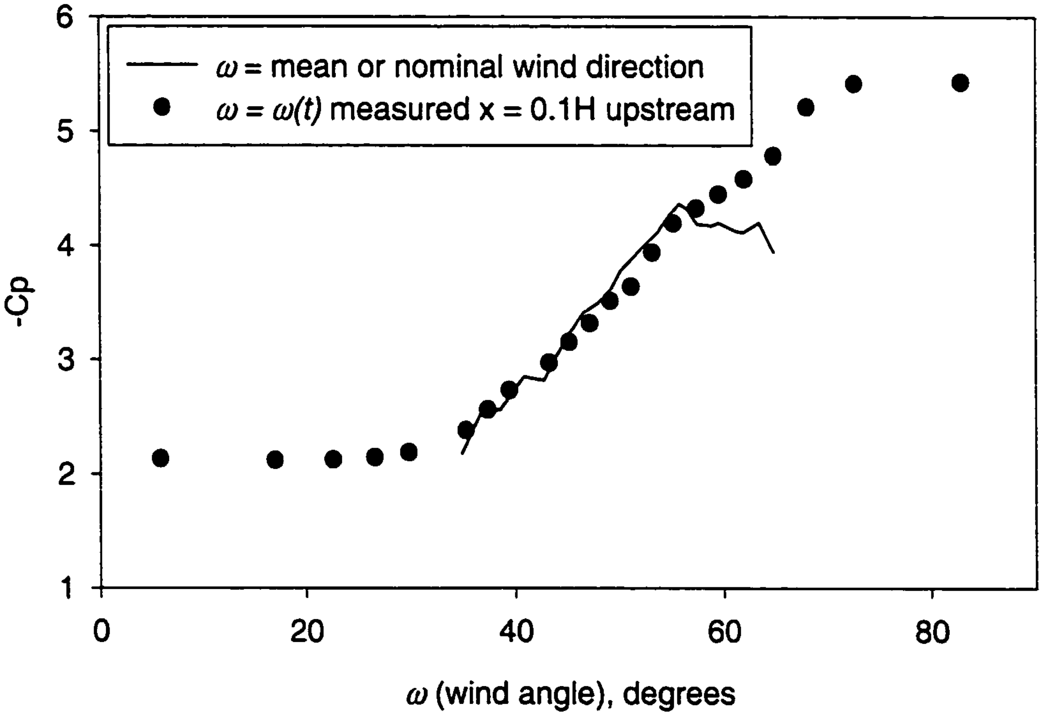

Figure 3.13 (Letchford and Marwood 1997): Cp vs. wind angle for a tap at $x = 0.05H$ and $\phi = 16°$. The $\omega(t)$ measurements were taken with a nominal wind direction of 45°.

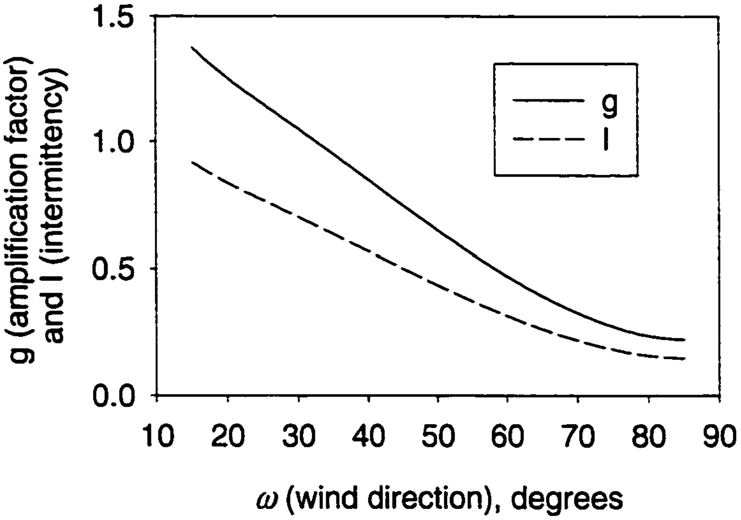

Figure 3.14: Mean $g(\omega)$ and $I(\omega)$ for tap row #3

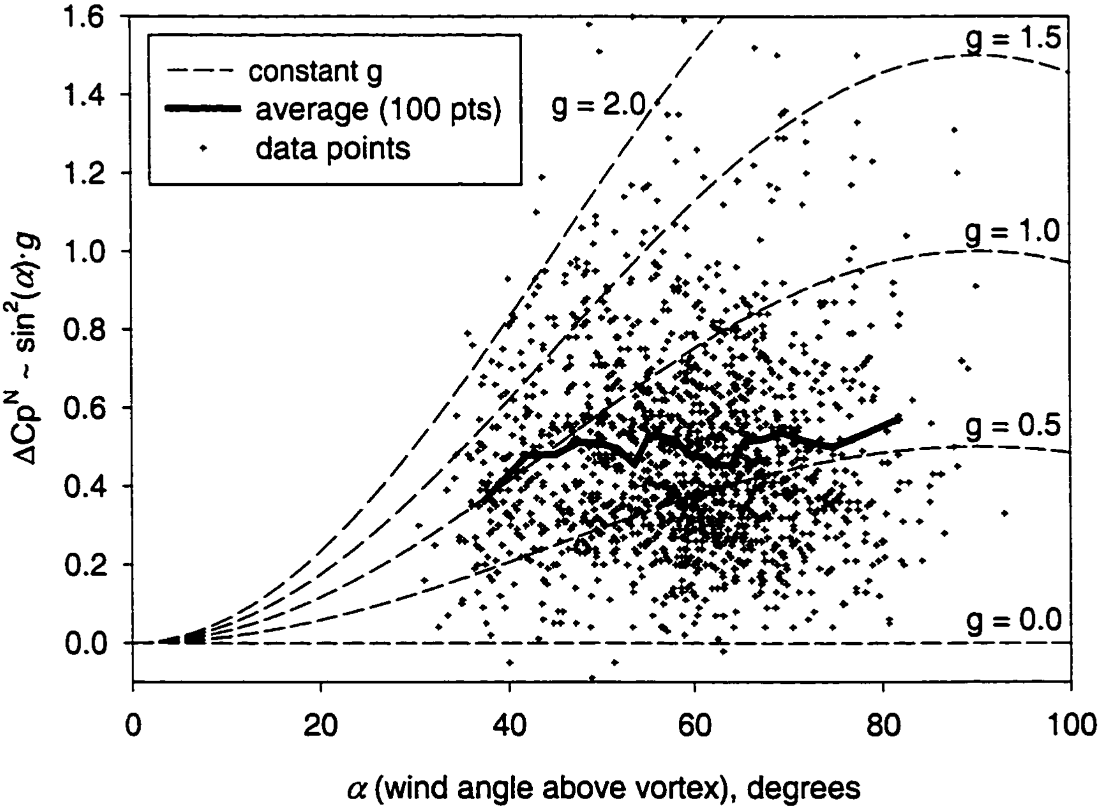

Figure 3.15: ΔCp^N data for $\omega_{nom} = 55°$. Target tap is tap #39

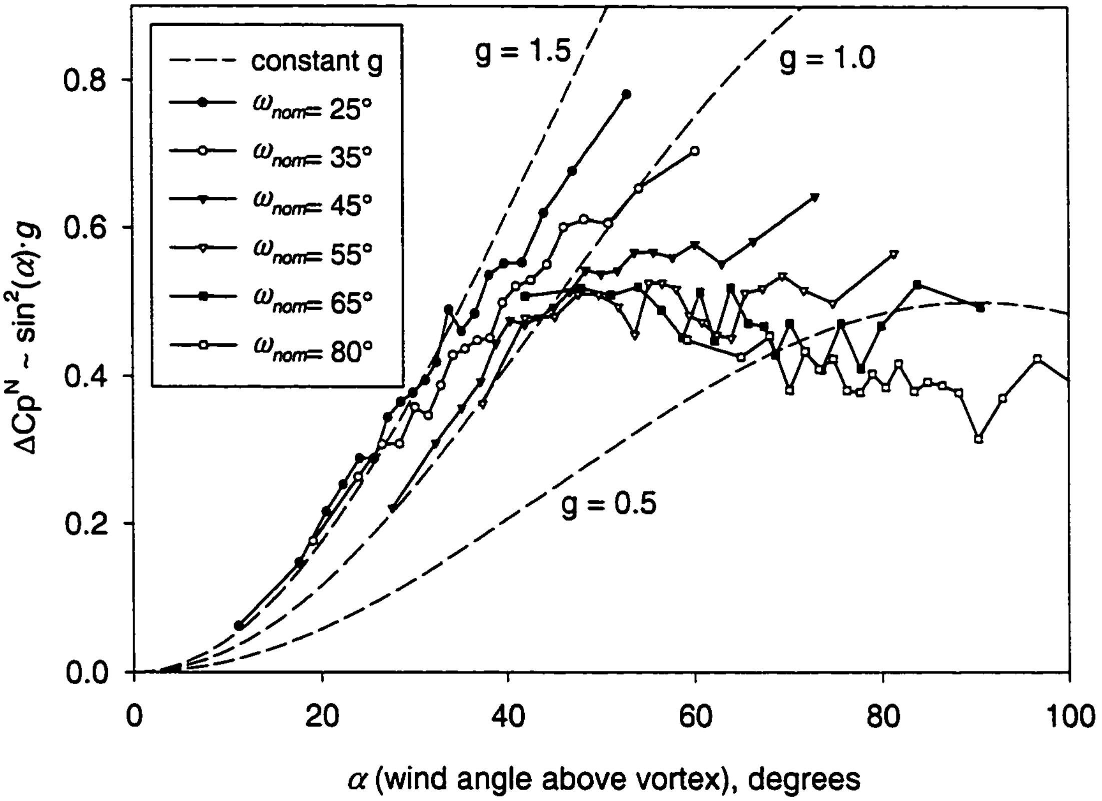

Figure 3.16: Group-averaged ΔCp^N curves for various nominal wind directions (tap #39)

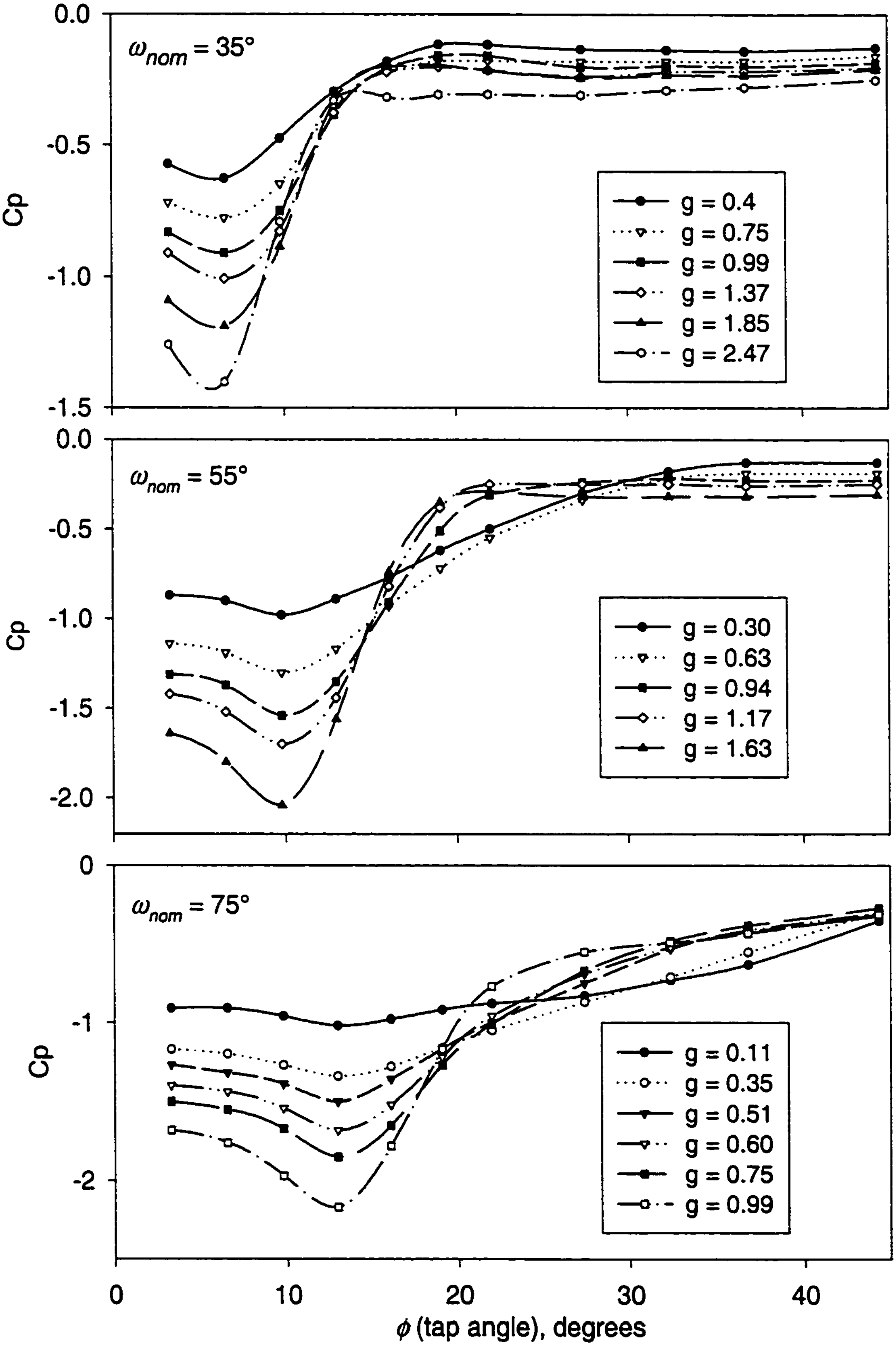

Figure 3.17: Pressure profiles beneath row #3, sorted by the value of *g*.

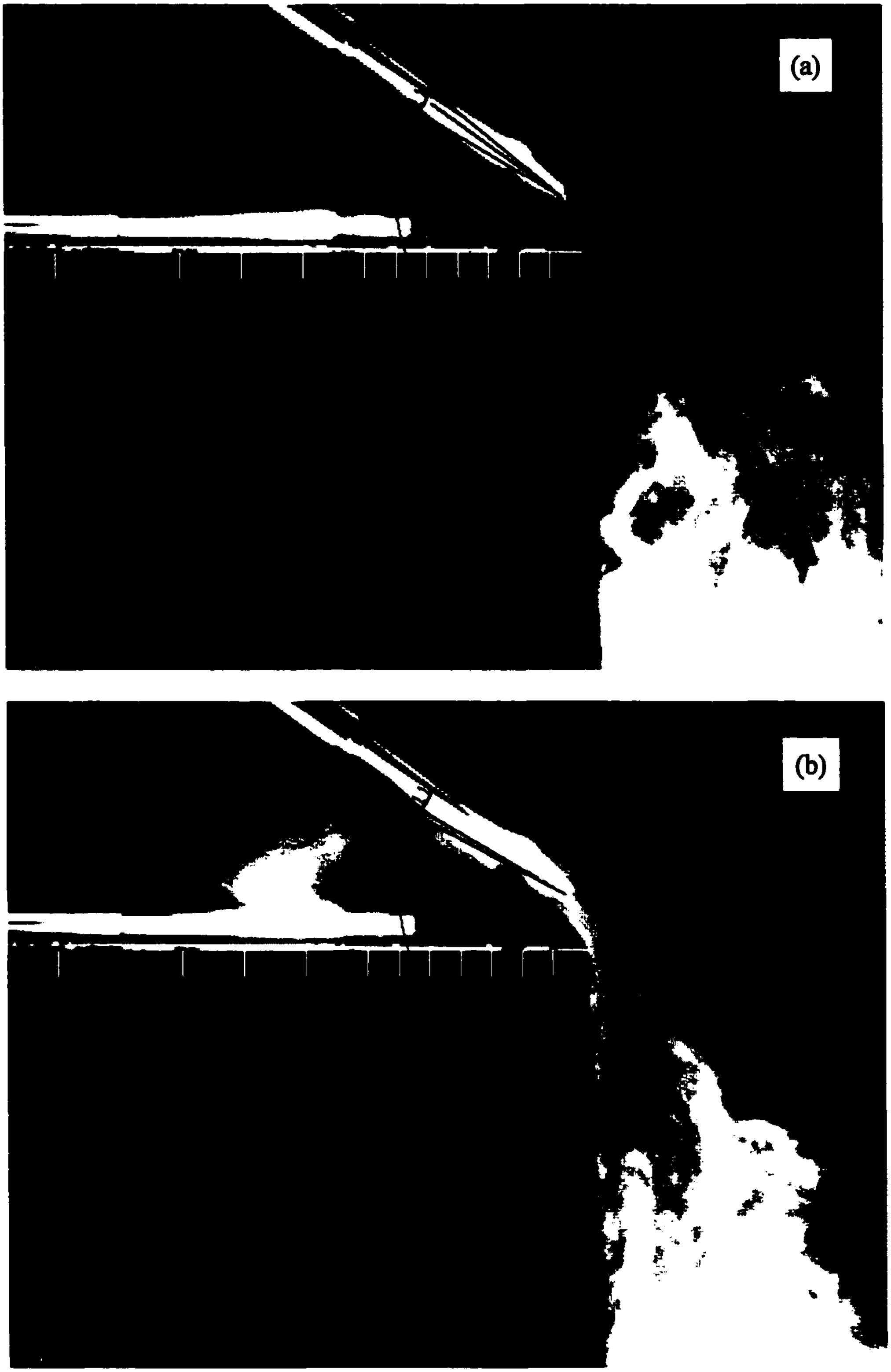

Figure 3.18: Images of flow above the roof edge, using a light sheet along tap row #5, and showing simultaneously measured pressure profiles and flow velocities. The images illustrate the difference between low *g* (a and c) and high *g* (b and d) flows.

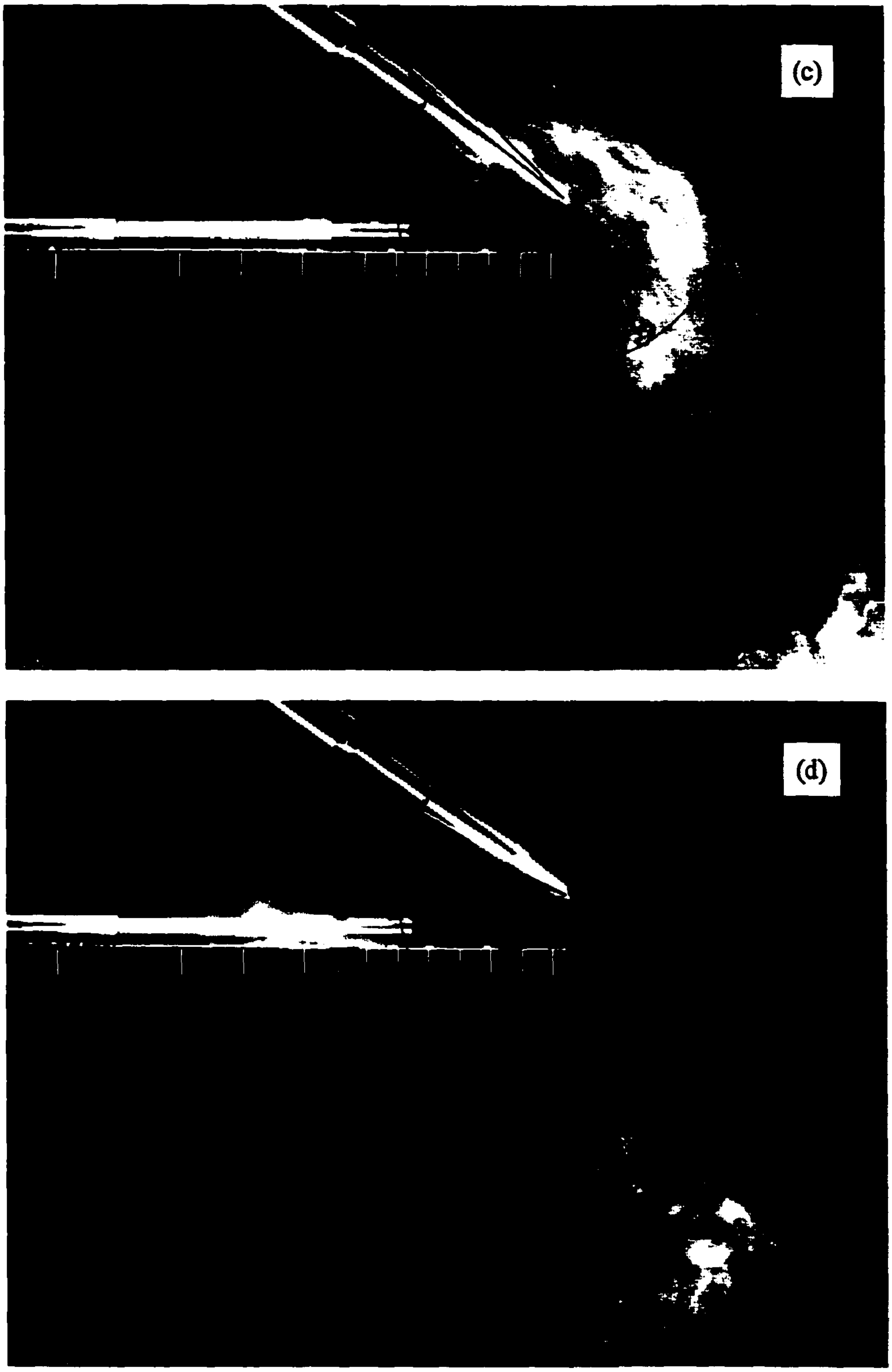

Figure 3.18 Continued

CHAPTER 4: THE APPLICABILITY OF QUASI-STEADY THEORY TO PRESSURE STATISTICS BENEATH ROOF-TOP VORTICES

Most of the material in Chapter 4 has been submitted to the Journal of Wind Engineering and Industrial Aerodynamics.

4.1 Introduction

The quasi-steady theory is a simple, practical model which links a building's surface pressure fluctuations directly to fluctuations in the local wind vector. The accuracy of the quasi-steady theory is important because it is the assumption embodied in many building codes (Cook 1990), where the design pressure is calculated using an equation of the form

$$p = q_z \cdot G \cdot \mathrm{Cp} \qquad \text{where } q_z = \text{flow head at height } z = \tfrac{1}{2}\rho\left(\overline{U}_z\right)^2 \tag{4.1}$$

G = expected gust factor

Cp = mean pressure coefficient

The Cp values are generally measured through wind tunnel studies, and the results are tabulated for various building types and atmospheric boundary layer conditions. If Eq. (4.1) is valid, then knowledge of the velocity time series at the roof height on the location where a building is to be constructed allows a prediction of the loads on the roof once the building is in place. Unfortunately, many studies have concluded that the quasi-steady theory fails to adequately predict pressures in separated flow, such as beneath the conical vortices (Calderone, et al. 1994, Letchford, et al. 1993, Tieleman and Hajj 1995, Uematsu and Isyumov 1998).

4.1.1 Review of quasi-steady theory

The quasi-steady equation can be derived from two assumptions:

1) The flow field is steady, inviscid, irrotational, and incompressible, and so obeys the Bernoulli equation, given by:

$$\tfrac{1}{2}\rho U_{ref}^{2}(t) + p_{ref}^{static}(t) = \tfrac{1}{2}\rho U_{M}^{2}(t) + p_{M}^{static}(t)$$

where the subscript *ref* indicates the position of reference measurement (usually upstream and to the side of the model), and the subscript *M* indicates a suitable measurement position anywhere in the flow field.

2) The steady condition can be extended to a quasi-steady regime where the entire flow field velocity changes simultaneously if the flow is Reynolds number independent, or $U_M(t) = k \cdot U_{ref}(t)$ where k = a constant.

Finally the pressure coefficient Cp is defined as

$$\mathrm{Cp}_{\mathrm{M}}(t) \equiv \frac{p_{M}^{static}(t) - p_{ref}^{static}(t)}{\tfrac{1}{2}\rho\left(\overline{U_{ref}}\right)^{2}}$$

Combining these three equations gives

$$\mathrm{Cp}_{\mathrm{M}}(t) = \frac{U_{ref}^{2}(t) - U_{M}^{2}(t)}{\left(\overline{U_{ref}}\right)^{2}} = \left(\frac{U_{ref}(t)}{\overline{U_{ref}}}\right)^{2} \cdot \left(1 - k^{2}\right) \tag{4.2a}$$

Time averaging $\mathrm{Cp_M}(t)$ gives $\overline{\mathrm{Cp}}_{\mathrm{M}} = \overline{\mathrm{Cp}_{\mathrm{M}}(t)} = \left(1 + I_U^{2}\right)\cdot\left(1 - k^{2}\right)$, since $\overline{\left(\frac{U(t)}{\overline{U}}\right)^{2}} = 1 + \mathrm{I}_{\mathrm{U}}^{2}$; hence

$$\mathrm{Cp}_{\mathrm{M}}(t) = \left(\frac{U_{ref}(t)}{\overline{U}_{ref}} \right)^2 \cdot \frac{\overline{Cp}_M}{1+I_U^2} \tag{4.2b}$$

If the value of $\overline{\mathrm{Cp}}_{\mathrm{M}}$ is dependent upon wind direction (θ) and pitch angle (β), a function $\overline{\mathrm{Cp}}_{\mathrm{M}}(6,\beta)$ can be used. The turbulence intensity term, $\mathrm{I_U}^2$, is often neglected. Assuming that this relationship applies to p_M^{static} measured on the surface of a building, one obtains the quasi-steady expression often used in wind engineering:

$$\mathrm{Cp}^{\mathrm{Q\text{-}S}}(t) = \left(\frac{U_{Htap}(t)}{\overline{U}_{Htap}} \right)^2 \overline{\mathrm{Cp}}\big(\theta_{Htap}(t), \beta_{Htap}(t)\big) \tag{4.3}$$

where the *Htap* subscript indicates properties that are evaluated from flow data at the height of the pressure tap, such as the horizontal wind direction (θ_{Htap}) and vertical wind pitch angle (β_{Htap}). Simultaneous velocity and surface pressure measurement has shown that pressures beneath the conical vortices are not sensitive to the vertical component of turbulence, so the influence of β_{Htap} can be neglected (Letchford and Marwood 1997).

For this study, pressures were measured beneath the separated flow zone near the edge of a flat roof low-rise building, so $U_{Htap}(t)$ and θ_{Htap} are the flow speed and direction measured at the building height, H, in the absence of the building. Of course, direct concurrent validation of Eq. (4.3) is not possible, since U_{Htap} cannot be measured with the building in place. However, since the reference velocity (U_{ref}), measured at building height some distance upstream and to the side of the building, is expected to have similar statistical properties to U_{Htap}, $\mathrm{Cp}^{\mathrm{Q\text{-}S}}(t)$ may be approximated by

$$\mathrm{Cp}^{\mathrm{Q\text{-}S}}(t) = \left(\frac{U_{ref}(t)}{\overline{U}_{ref}} \right)^2 \overline{\mathrm{Cp}}(\theta_{ref}(t)) \tag{4.4}$$

and the value should have the same statistical properties as $Cp^{Q\text{-}S}(t)$ obtained from Eq. (4.3). To validate quasi-steady theory, statistics from Eq. (4.4), such as mean Cp, Cp_{rms} (σ_{Cp}), the probability distribution function (pdf) and the power spectrum of $Cp^{Q\text{-}S}(t)$, can be compared to those of the measured pressure coefficients time series $Cp(t)$, defined earlier.

The function $C\overline{p}(6)$ that is used in Eq. (4.4) is typically produced from wind tunnel studies in which the model building is rotated through 360° at 5° or 10° increments. The mean pressure coefficient $\left(\overline{Cp(t)}\right)$ is calculated for each rotation position, and this is tabulated as the $C\overline{p}(6)$ value for the corresponding wind direction. Once compiled, these values produce the $Cp_{mean}(\theta)$ or $C\overline{p}(6)$ plot typically reported in wind engineering literature. I will refer to this function as the mean value of $Cp(t)$ for a nominal wind direction of θ, or $C\overline{p}^{\,nom\theta}(\theta)$. As Richards has demonstrated, $C\overline{p}^{\,nom\theta}(\bar{\theta})$ is not necessarily the same as the value of $\overline{Cp(t)}$ when the wind direction has an instantaneous value of $\theta(t) = \bar{\theta}$ (Richards, et al. 1995). This latter function I will refer to as $C\overline{p}^{\,inst\theta}(\theta)$. Since the quasi-steady theory purports to estimate the effects of instantaneous wind direction change, $C\overline{p}^{\,inst\theta}(\theta)$ is theoretically a more correct function for use in Eq. (4.4) than $C\overline{p}^{\,nom\theta}(\bar{\theta})$. As will be shown in section 5, $C\overline{p}^{\,nom\theta}(\bar{\theta})$ has lower peaks than $C\overline{p}^{\,inst\theta}(\theta)$.

4.1.2 Review of the Vortex Flow Mechanism

On buildings with flat roofs and sharp roof/wall edges, flow separation may take on two forms. For flow ± 20° about the normal to the roof edge, a condition called bubble separation dominates. In this situation, there is high suction between the roof edge and the point of reattachment. Peak suctions are generated when cylindrical vortices are formed along the roof edge and are convected through the separated flow zone towards the re-attachment point (Saathoff and Melbourne 1989).

For flow ± 25° from a cornering flow, dual conical vortices exist which are responsible for the largest suctions on the rooftop. The following equation for the surface pressure beneath the conical vortices was validated in Chapter 3:

$$\mathrm{Cp_S}(t) = \left(\frac{U_M(t)}{\overline{U}_M(\omega(t))}\right)^2 \left[1 - \left(\frac{\overline{U}_M(\omega(t))}{\overline{U}_{ref}}\right)^2 \left(1 + \sin^2(\alpha(t)) \cdot g(\omega(t), t)\right)\right], \tag{4.5}$$

Recall that the term g expresses the pressure drop across the vortex core from the point M to the point S, and is an indication of the quality of the vortex; $g = 0$ for no vortex, while $g \approx 1.5$ for a well formed vortex. The function g can be divided by separation of variables:

$$g(\omega(t), t) = \overline{g}(\omega) \cdot g'(t),$$

where $g'(t)$ is a nearly Gaussian random variable which accounts for random changes in the vortex quality, and $\overline{g}(\omega)$ decreases with increasing ω (Fig. 4.1), possibly as the result of the lack of axial flow destabilizing the conical vortex.

All of the original data presented and discussed in this chapter, such as the nature of $g'(t)$, was gathered using the experimental procedures described in Section 3.2.

4.2 Implications of the vortex flow mechanism for Q-S theory

In addition to the mean value of g, Fig. 4.1 shows the values of some of the variables for Eq. (4.5) measured using this configuration and the conditional sampling technique. As noted above, Cp_S does not correspond to the suction at a single tap, since the vortex core moves in response to changes in wind direction (see Fig. 4.2). However, the pressure at a single tap is still simply a function of the wind angle $\omega(t)$, since the position of the tap relative to the core dictates Cp_{tap} according to the equation:

$$C\overline{p}_{tap}(\omega) = \left(C\overline{p}_S(\omega) - Cp_a\right)\cdot\eta(\omega) + Cp_a$$

where Cp_a is the asymptotic value of $Cp(\phi)$ in the middle of the roof, beyond the influence of the vortex. The function η is explained in Fig. 4.3. It acts as a transfer function, using the mean $Cp(\phi)$ pressure profile shape and the location of the vortex core relative to the tap in question to convert the $Cp_S(\omega)$ function into a $Cp_{tap}(\omega)$ function.

The vortex core also moves randomly about its mean position for any given wind direction (Fig. 4.4), possibly due to changes in the very high frequency turbulence of the same scale as the shear layer (Melbourne 1993). (It is known that changes in turbulence intensity affect the mean reattachment position for bubble separation (Li and Melbourne 1995)). The effect of this motion on the time dependent value of Cp_{tap} can be given by

$$Cp_{tap}(t) = \left(Cp_S(t) - Cp_a\right)\cdot\eta\left(\omega\cdot(1+\omega')\right) + Cp_a$$

where ω' is a Gaussian random variable with a mean value of 0 which expresses the effect of the random core motion at any given wind angle.

The full equation for $Cp(t)$ at a tap under the region of vortex influence in now given by

$$\begin{aligned} Cp_{tap}(t) &= \left(\frac{U_M(t)}{\overline{U}_M\left(\omega(t)\right)}\right)^2 \cdot Cp_{tap}(\omega) \\ Cp_{tap}(\omega) &= \left[1 - \left(\frac{\overline{U}_M\left(\omega(t)\right)}{\overline{U}_{ref}}\right)^2 \left(1 + \sin^2\left(\alpha(t)\right)\cdot\overline{g}\left(\omega(t)\right)\cdot g'(t)\right) - Cp_a\right]\cdot\eta\left(\omega\cdot(1+\omega')\right) + Cp_a \end{aligned} \tag{4.6}$$

Since $\alpha(t)$ is essentially a function of $\omega(t)$, Eq. (4.6) has the same form as the quasi-steady equation, except for the influence of the $g'(t)$ and ω' terms, which is assessed in section 5.2. Since the conditionally sampled normalized velocity at M has similar characteristics to the normalized reference flow velocity (see Fig. 4.5), the Q-S theory should provide a reasonable estimate for pressure statistics beneath the vortex core, which contradicts the findings of the studies listed in section 4.1.

4.3 Aspects of quasi-steady theory validation

4.3.1 Statistics: Mean, standard deviation, and probability distribution

The studies which rejected the use of the quasi-steady theory in zones of flow separation generally used the following linear estimate for $\overline{Cp}(\theta)$ in Eq. (4.4):

$$\overline{Cp}(\theta) = \overline{Cp}(\bar{\theta}) + (\theta - \bar{\theta})\frac{\partial \overline{Cp}(\bar{\theta})}{\partial \theta} \tag{4.7}$$

This linear quasi-steady model is known to fail to adequately predict fluctuating pressures at the stagnation point on a circular tower (Maier-Erbacher and Plate 1991). As noted by Hoxey, the failure of the linear quasi-steady model to adequately predict measured σ_{Cp} values is largely attributable to the oversimplification in Eq. (4.7) (Hoxey, et al. 1995), and good σ_{Cp} agreement has been illustrated on windward facing taps and in separated flow zones when Eq. (4.4) is evaluated fully (Hoxey and Robertson 1994). The nature of the inaccuracy of Eq. (4.7) for estimating σ_{Cp} will be investigated in section 5.2 of this paper, as will the validity of Eq. (4.4) with respect to σ_{Cp} in general.

The use of σ_{Cp} to examine scatter and peak pressures is often too reductive, so I will also examine the implications of quasi-steady theory for the PDF of pressures under the conical vortices in section 5.3.

4.3.2 Frequency considerations: coherence and spectral analysis

The quasi-steady theory has been interpreted to imply that the coherence, cross-correlation (between taps) and spectrum of wind-induced pressures should be equal to those of the local wind velocity head. This has been shown to be invalid, as the surface pressure spectra attenuate faster than the velocity spectra (Geurts 1996, Geurts, et al. 1997), and the local pressure coherence and cross-correlation under the separated flow zones are greater than that of the incident flow (Sankaran and Jancauskas 1993).

The increased cross-correlation is simply the result of the existence of a coherent flow structure (the vortex), which is not present in the upstream flow. This is an essential consideration when calculating total loads.

Calculating the surface pressure spectrum associated with various incident flow spectra has been addressed successfully for taps on the windward wall through the use of an admittance function, which cuts off the incident flow turbulence at $fB/U \approx 0.2$, or gusts roughly five times the largest building plan dimension (B) (Kawai 1983). The discussion in section 3.4 of the effects of various gust sizes on the vortex suggests that a similar admittance can be used to describe the relationship between upstream flow and roof pressures beneath the conical vortices.

All gusts can be expected to directly influence the surface pressure through the $U_M(t)/\text{mean}(U_M)$ term; however, only those gusts large enough to spin the entire vortex faster ($fB/U < 10$) would have a full effect on Cp_S. Only lateral gusts (i.e., changes in $\omega(t)$) that are larger than the building ($fB/U < 1$) would be expected to move the vortices, causing them to "sway" from side to side. Since an increase in ω for one conical vortex implies a decrease in ω for the other, and Cp_S increases through the $\sin^2(\alpha)\cdot g(\omega)$ and

$U_{max}(\omega)$ terms as $\omega(t)$ approaches 60°, the vortex sway will also produce low frequency suction fluctuations which are correlated to low frequency upstream lateral turbulence. This has been observed through simultaneous pressure measurement over the whole roof surface (Kawai and Nishimura 1996). For many taps, especially those that are intermittently under the vortex and in the re-attachment zone, the vortex core position (as expressed by the $\eta(\omega)$ term) is the dominant influence on surface pressure. As a result, these taps will exhibit a strong correlation in suction with the lower frequency lateral turbulence that causes the mean vortex position to change.

The notion of an admittance is fundamental to the validation of the quasi-steady theory; it is clear that for low enough frequencies, the quasi-steady theory will hold true. For example, a wind direction change lasting over a minute at full scale ($fB/U \approx 0.03$) ought to have the same effect as a shift in mean wind direction, while a gust with $fB/U = 10$ would not be expected to affect the mean flow pattern around the building in any significant way. As long as gusts which are of sufficient size and duration to affect a structural element of interest are passed on to the building surface pressure in keeping with Eq. (4.4), then the quasi-steady model is, for practical purposes, valid for point pressures. In this context, the question is not so much one of the validity of the quasi-steady model, but rather one of its frequency limits. For this reason, the effects of data filtering will be addressed in section 5.1.

4.4 *Discussion of Results*

4.4.1 *Part 1: Mean pressures*

As noted in the introduction, the expected value of Cp(t) when the wind instantaneously comes from an angle θ_0, calculated as

$$\overline{\mathrm{Cp}}^{\mathrm{inst}\theta}(\theta_0) = \overline{\mathrm{Cp(t)}} \text{ when } \theta(t) = \theta_0,$$

is not the same as the measured or expected value of Cp(t) for a nominal or run-averaged wind direction of $\bar{\theta}$, which is calculated as

$$\overline{\mathrm{Cp}}^{\mathrm{nom}\theta}(\theta_0) = \overline{\mathrm{Cp(t)}} \text{ when } \overline{\theta(t)} = \theta_0 .$$

The expected value of $\overline{\mathrm{Cp}}^{\mathrm{nom}\theta}(\theta)$ for a given wind direction θ_0 can be calculated from $\overline{\mathrm{Cp}}^{\mathrm{inst}\theta}(\theta)$; since the wind direction is widely accepted to have a Gaussian distribution,

$$\overline{\mathrm{Cp}}^{\mathrm{nom}\theta}(\theta_0) = \frac{1}{\sqrt{2\pi}\sigma_\theta}\int_{-\infty}^{\infty}\overline{\mathrm{Cp}}^{\mathrm{inst}}(\theta)\exp(-(\theta-\theta_0)/2\sigma_\theta)^2 d\theta . \qquad (4.8)$$

The distribution of $\theta(t)$ causes $\overline{\mathrm{Cp}}^{\mathrm{inst}\theta}(\theta)$ to be averaged over a range of wind angles when calculating $\overline{\mathrm{Cp}}^{\mathrm{nom}\theta}(\theta_0)$. The result is that $\left|\overline{\mathrm{Cp}}^{\mathrm{nom}\theta}(\bar{\theta})\right|$ is less than $\left|\overline{\mathrm{Cp}}^{\mathrm{inst}\theta}(\theta)\right|$ for peak values, as shown in Fig. 4.6 for data on the front face of a circular cylinder (the data is adapted from a full scale study (Maier-Erbacher and Plate 1991)). (See section 5.3 for more details on the calculation of the $\mathrm{Cp}^{\mathrm{inst}}$ PDF). We see that the value of $\overline{\mathrm{Cp}}^{\mathrm{nom}\theta}(2°)$ is the weighted average of the surrounding $\overline{\mathrm{Cp}}^{\mathrm{inst}\theta}(\theta)$ values, which must be less than

$\overline{\mathrm{Cp}}^{\mathrm{inst}\theta}(2°)$, since this is a peak value. Eq. (4.8) was solved for $\overline{\mathrm{Cp}}^{\mathrm{inst}\theta}(\theta)$ by evaluating Eq. (4.8) numerically and iteratively minimizing the residual[3].

The underlying assumption for this type of calculation is that a universal function $\overline{\mathrm{Cp}}^{\mathrm{inst}\theta}(\theta)$ exists for this tap; or that regardless of the nominal wind direction $\bar{\theta}$, an instantaneous shift in wind direction to θ will produce the same surface pressure at that tap. This assumption has been tested at CSU using data from the experimental configuration described in Section 3, where $\theta(t)$ is measured at the point M. Fig. 4.7 shows data from tests where the x-wire was placed 24mm above tap #41. This point is about 3 times as far above the surface as the expected vortex core height at $\omega = 45°$, and is out of the separated flow, above the shear layer.

Each plot includes two $\overline{\mathrm{Cp}}^{\mathrm{inst}\theta}$ curves, calculated above from Eq. (4.8) using $\sigma_\omega = 8°$ and $\sigma_\omega = 10°$, and the $\overline{\mathrm{Cp}}^{\mathrm{nom}\theta}$ curve for tap #9 from which they are derived. These curves illustrate again how $|\overline{\mathrm{Cp}}^{\mathrm{inst}\theta}| > |\overline{\mathrm{Cp}}^{\mathrm{nom}\theta}|$ at pressure peaks like those at $\omega = 20°$ and $\omega = 60°$. Each individual plot shows the measured $\overline{\mathrm{Cp}}^{\mathrm{inst}\theta}(\omega)$ values for the given nominal wind angle $\left(\overline{\mathrm{Cp}}^{\mathrm{inst}\theta}_{\mathrm{meas}}(\omega(t), \omega_{nom})\right)$. The simultaneously recorded $\mathrm{Cp}(t)$ and $\omega(t)$ time series were sorted by ω, and successive groups of 500 data points were averaged for each filled circle data point. This procedure was repeated after the Cp and ω time series were filtered at 2 Hz (5th order Butterworth filter) to produce the open circle data points.

---

[3] Note that a relationship such as that expressed in Equation (8) can be approximated (Papoulis 1984) as $\overline{\mathrm{Cp}}^{\mathrm{inst}\theta}(\theta) \approx \overline{\mathrm{Cp}}^{\mathrm{nom}\theta}(\theta) - \frac{d^2\overline{\mathrm{Cp}}^{\mathrm{nom}\theta}(\theta)}{d\theta^2} \cdot \frac{\sigma_\theta^2}{2}$, which in the case of Fig. 4.6 agrees quite well with the full solution to Equation (7). This approximation is much less accurate for $\mathrm{Cp}(\theta)$ under a vortex.

The measured σ_ω for the unfiltered and filtered $\omega(t)$ time series was 10° and 8° respectively.

While the plots for ω_{nom}= 15° and ω_{nom}=25° confirm that the value of $\overline{\mathrm{Cp}}^{\mathrm{nom}\theta}$ does not necessarily lie on the $\overline{\mathrm{Cp}}^{\mathrm{inst}\theta}$ curve, the $\overline{\mathrm{Cp}}^{\mathrm{inst}\theta}_{\mathrm{meas}}$ curves do not follow the predicted $\overline{\mathrm{Cp}}^{\mathrm{inst}\theta}$ values very well, especially for $\omega(t) < 15°$. This indicates that the separation bubble on the other wall, which is responsible for the secondary negative peak at $\omega = 0°$, does not establish fully when the wind momentarily shifts to $\omega(t) = 0°$.

For $\omega_{nom} = 35°$ and $\omega_{nom} = 45°$, the measured and predicted $\overline{\mathrm{Cp}}^{\mathrm{inst}\theta}$ curves show good agreement as the conical vortex moves away from the leading edge and over the tap. Quasi-steady theory assumes that $\overline{\mathrm{Cp}}^{\mathrm{inst}\theta}_{\mathrm{meas}}$ will fall on the predicted $\overline{\mathrm{Cp}}^{\mathrm{inst}\theta}$ curve, so for these angles, quasi-steady theory can be expected to be accurate.

For $\omega_{nom} = 55°$ and $\omega_{nom} = 65°$, the unfiltered experimental data still follow the predicted $\overline{\mathrm{Cp}}^{\mathrm{inst}\theta}$ behaviour for $\omega < 60°$, but for $\omega > 60°$, these data stay at a higher suction than the predicted curve. I suspect that this is because the vortex is more likely to remain stable during a brief wind direction excursion of $\omega > 65°$ than for a longer duration wind direction change. This is confirmed by the fact that the data do follow the predicted $\overline{\mathrm{Cp}}^{\mathrm{inst}\theta}$ curves when low pass filtered.

At $\omega_{nom} = 75°$, even the 2 Hz filter fails to keep the measured data on the predicted $\overline{\mathrm{Cp}}^{\mathrm{inst}\theta}$ line, and at $\omega_{nom} = 85°$, the behaviour is completely inconsistent with that expected by quasi-steady theory. I believe that this is because momentary wind direction excursions to $\omega < 75°$ fail to re-establish the consistent conical vortex needed to attain the kind of mean suction seen for $\omega_{nom} = 60°$.

The general picture of the flow mechanism under the separated flow along the leading edge provided by these observations is one in which the flow structure exhibits a kind of hysteresis, where the value of $\overline{Cp}_{\text{meas}}^{\text{inst}\theta}$ is dependent upon the direction in which the wind has shifted; $\overline{Cp}_{\text{meas}}^{\text{inst}\theta}(45°)$ is quite different for $\omega_{nom} = 25°$ and $\omega_{nom} = 65°$. This hysteresis can be reduced or eliminated in some cases by low-pass filtering the data, since a wind direction change of long enough duration will permit the transition from separation bubble to conical vortex to take place. However, the cutoff frequency needed for such filtering to be effective is extremely low (T ~ 25 seconds at full scale), so that the quasi-steady theory is not expected to offer a reliable estimate of 3 second gust loads except when $35° < \omega_{nom} < 55°$. As will be shown in the next section, other factors not considered in Eq. (4.2) make the quasi-steady theory unreliable for predicted pressure fluctuations even for these mean wind directions.

4.4.2 Part 2: Rms pressures

One of the principal uses of the quasi-steady theory is to predict the surface pressure fluctuations ($Cp_{rms}(\theta)$, also written as $\sigma_{Cp}(\theta)$) based on flow velocity fluctuations. The underprediction of Cp_{rms} is also one of the more commonly cited examples of the failure of quasi-steady theory (Letchford, et al. 1993, Maier-Erbacher and Plate 1991). However, it has been shown that this underprediction is often due primarily to the use of the inaccurate linear approximation for $Cp(\theta)$ (Eq. (4.7)) (Richards, et al. 1995). Bearing in mind the limitations on the applicability of quasi-steady theory implied by the nonexistence of a single or unique $\overline{\mathrm{Cp}}^{\mathrm{inst}\theta}(\omega)$ function, this section will examine the application of quasi-steady theory to predict $\mathrm{Cp}_{\mathrm{rms}}(\theta)$.

The rms value of any function $R=R(x_1,x_2,\ldots x_n)$ can be estimated using the relation

$$\sigma_R^2 = \left(\overline{\frac{\partial R}{\partial x_1}}\cdot\sigma_{x_1}\right)^2 + \left(\overline{\frac{\partial R}{\partial x_2}}\cdot\sigma_{x_2}\right)^2 + \ldots\left(\overline{\frac{\partial R}{\partial x_n}}\cdot\sigma_{x_n}\right)^2 \qquad (4.9)$$

If the turbulence intensity term from Eq. (4.2b) is re-introduced into Eq. (4.4), the quasi-steady equation can be written as

$$\mathrm{Cp}^{\text{Q-S}}(t,\theta) = \left(\frac{U_{ref}(t)}{\overline{U}_{ref}}\right)^2 \frac{\overline{\mathrm{Cp}}(\theta)}{1+\mathrm{I}_{\mathrm{U}}^2} \qquad (4.10)$$

Note again that the function $\overline{\mathrm{Cp}}(\theta) \equiv \overline{\mathrm{Cp}}^{\mathrm{inst}\theta}(\theta)$ is the most accurate function to use in the quasi-steady equation, since it yields $\overline{\mathrm{Cp}(t,\theta(t)=\theta)} = \overline{\mathrm{Cp}}^{\mathrm{inst}\theta}(\theta)$ and $\overline{\mathrm{Cp}(t,\theta(t))} = \overline{\mathrm{Cp}}^{\mathrm{nom}\theta}(\theta)$ in Eq. (4.10). This implies that $\overline{\mathrm{Cp}}(\theta) = \overline{\mathrm{Cp}}^{\mathrm{inst}\theta}(\theta)/(1+I_U^2)$ should be used in the standard quasi-steady relation, Eq. (4.4).

Applying Eq. (4.9) to Eq. (4.10), where x_1 = the normalized velocity and x_2 = $\mathrm{Cp}(\theta)$, gives

$$\sigma^2_{\mathrm{Cp}(t)}(\theta) = \left(\frac{\overline{\mathrm{Cp}}^{\mathrm{nom}\theta}(\theta)}{(1+\mathrm{I}_{\mathrm{U}}^2)}\cdot 2\mathrm{I}_U\right)^2 + \sigma^2_{\overline{\mathrm{Cp}}(\theta)} \text{ since } \sigma_{\left(\frac{U(t)}{\overline{U}}\right)^2} = 2\mathrm{I}_U \qquad (4.11)$$

Richards provides a similar equation, as well as a method of solving for the expected value of $\mathrm{Cp}_{\mathrm{rms}}(\theta)$ (Richards, et al. 1995):

$$\begin{aligned}\sigma^2_{\overline{Cp}(\theta)}(\bar\theta) &= \mathrm{Cprms}_{\_\theta}(\theta) = \mathrm{E}[(\overline{\mathrm{Cp}}^{\mathrm{inst}\theta}(\theta) - \overline{\mathrm{Cp}}^{\mathrm{nom}\theta}(\bar\theta))^2] \\ &= \frac{1}{\sqrt{2\pi}\sigma_\theta}\int_{-\infty}^{\infty}\left(\overline{\mathrm{Cp}}^{\mathrm{inst}\theta}(\theta) - \overline{\mathrm{Cp}}^{\mathrm{nom}\theta}(\bar\theta)\right)^2 \exp\left(-(\theta-\bar\theta)/2\sigma_\theta\right)^2 d\theta\end{aligned} \qquad (4.12)$$

This integral has been solved using both the predicted $\overline{\mathrm{Cp}}^{\mathrm{inst}\theta}(\omega)$ curve, and for the actual measured $\left(\overline{\mathrm{Cp}}^{\mathrm{inst}\theta}_{\mathrm{meas}}(\omega(t),\overline{\omega}_{nom})\right)$ curves shown in Fig. 4.7.

If instead the linear approximation (Eq. (4.7)) is used to calculate $\sigma_{\overline{Cp}(\theta)}$, the result is

$$\sigma_{\overline{Cp}(\theta)} = \left|\frac{\partial \overline{\mathrm{Cp}}(\theta)}{\partial \theta}\right| \cdot \sigma_{\theta}, \tag{4.13}$$

where I_v (the lateral turbulence intensity) is commonly substituted for σ_θ (Letchford, et al. 1993, Tieleman and Hajj 1995). This linear approximation is only useful when the value of a linear fit to Cp(θ) is valid over a range of around $\pm 2\sigma_\theta$, which is seldom the case, especially for most crucial wind directions, near pressure peaks. Note also that the linear approximation is much more effective if σ_θ is small.

Fig. 4.8(a) illustrates the relative magnitude of the two terms in Eq. (4.11), as applied to the data shown in Fig. 4.7 for tap #9. The measured total $\mathrm{Cp}_{\mathrm{rms}}(\theta)$ is shown for comparison. The first term in Eq. (4.11) depends directly on the value of $\overline{\mathrm{Cp}}^{\mathrm{nom}\theta}(\omega)$ and the turbulence intensity (in these tests, T.I. = 20%). It is labelled $\mathrm{Cprms\_}_{\mathrm{TI}}$. The second term accounts for the effects of shifting wind direction, and has been calculated and plotted using 3 different $\overline{\mathrm{Cp}}(\omega)$ curves:

- $\mathrm{Cprms\_}_{\theta}^{\mathrm{inst}}$: Eq. (4.12), using the predicted $\overline{\mathrm{Cp}}^{\mathrm{inst}\theta}(\omega)$ curve,
- $\mathrm{Cprms\_}_{\theta}^{\mathrm{meas}}$: Eq. (4.12), using the unfiltered measured $\overline{\mathrm{Cp}}^{\mathrm{inst}\theta}_{\mathrm{meas}}(\omega(t),\omega_{nom})$ curves from Fig. 4.7. This should be considered the best estimate of the true $\sigma_{\overline{Cp}(\theta)}(\omega)$ values, and
- $\mathrm{Cprms\_}_{\theta}^{\mathrm{linear}}$: Eq. (4.13), using the measured $\overline{\mathrm{Cp}}^{\mathrm{nom}\theta}(\omega)$ curve.

As might be expected from the results in Fig. 4.7, $\mathrm{Cprms\_}_{\theta}^{\mathrm{inst}}$ agrees quite well with $\mathrm{Cprms\_}_{\theta}^{\mathrm{meas}}$ for $\omega < 60°$, since, as noted above, the measured $\overline{\mathrm{Cp}}^{\mathrm{inst}\theta}(\omega)$ follows the predicted $\overline{\mathrm{Cp}}^{\mathrm{inst}\theta}(\omega)$ quite well. And since the measured $\overline{\mathrm{Cp}}^{\mathrm{inst}\theta}(\omega)$ does not follow the predicted curve when $\omega > 60°$, but instead remains fairly constant for any instantaneous wind angle, the quasi-steady theory (both the linear estimate and the full integral) overpredicts $\mathrm{Cprms\_}_{\theta}$ at these wind angles.

The linear model also underpredicts $\mathrm{Cprms\_}_{\theta}$ at the peaks ($\omega = 25°$ and $\omega = 60°$), and overpredicts $\mathrm{Cprms\_}_{\theta}$ when the $\mathrm{Cp}(\theta)$ slope is high. These errors are paradoxically reduced if the differential in Eq. (4.13) is performed crudely, with large $\Delta\omega$ steps both in the derivative and between the location where it is evaluated.

The net effect of these calculation methods on the total Cprms is displayed in Fig. 4.8(b), where the $\mathrm{Cprms\_}_{\theta}(\theta)$ and $\mathrm{Cprms\_}_{\mathrm{TI}}(\theta)$ are added as in Eq. (4.11):

$$\sigma_{\mathrm{Cp}}^{2}(\theta) = \left(\mathrm{Cprms\_}_{\mathrm{TI}}\right)^{2} + \left(\mathrm{Cprms\_}_{\theta}\right)^{2}$$

All three quasi-steady evaluations do a respectable job of predicting the total Cprms, though the linear estimate exhibits unrealistic peaks and valeys for reasons cited above. The measured quasi-steady Cprms curve in particular shows good agreement with the general shape of the actual measured Cprms, but consistently underpredicts Cprms. This has been examined in light of the flow mechanism model of Eq. (4.6). Applying Eq. (4.9) to Eq. (4.6) yields two additional terms:

$$\sigma_{\mathrm{Cp}}^{2}(\theta) = \left(\mathrm{Cprms\_}_{\mathrm{TI}}\right)^{2} + \left(\mathrm{Cprms\_}_{\theta}\right)^{2} + \left(\mathrm{Cprms\_}_{g'}\right)^{2} + \left(\mathrm{Cprms\_}_{\omega'}\right)^{2} \quad \text{where}$$

$$\mathrm{Cprms\_}_{g'}(\omega) = \left(1 + \mathrm{I}_{\mathrm{U}}^{2}\right) \cdot \left(\frac{\overline{U}_{\max}(\omega)}{\overline{U}_{ref}} \right)^{2} \cdot \sin^{2}(\alpha) \cdot g(\omega) \cdot \eta(\omega) \cdot \sigma_{g'},$$

$$\mathrm{Cprms}_{-\omega'}(\omega)=\left(1+\mathrm{I}_{\mathrm{U}}^{2}\right)\cdot\left(Cp_s(\omega)-Cp_a\right)\cdot\sigma_{\omega'},$$

$$\text{and } \sigma_{\omega'}(\omega)=\int_{-\infty}^{\infty}\eta(\omega(1+\omega'))\cdot f_{\omega'}(\omega')d\omega'.$$

(The function $f_{\omega}(\omega')$ is the probability distribution function for ω'. It is Gaussian, with a mean of 0 and $\sigma_{\omega'} = 0.3\omega$).

$\mathrm{Cprms}_{-g'}$ accounts for random changes in the vortex quality, while $\mathrm{Cprms}_{-\omega'}$ accounts for random changes in the vortex position (recall Fig. 4.4). These two terms are shown in Fig. 4.8(c), along with the resulting total Cprms. The values of $\sigma_{g'}$ and $\sigma_{\omega'}$ have been estimated at 0.45 and 0.3 respectively. For tap #9, it is primarily the absence of a term describing the effects of random vortex motion which results in the quasi-steady theory's underprediction of Cprms.

4.4.3 Probability distribution functions

While the matching of predicted and measured mean and peak Cp values is an important aspect of quasi-steady theory validation, a comparison of the probability distribution function (pdf) of $\mathrm{Cp}^{\mathrm{Q\text{-}S}}(t)$ and $\mathrm{Cp}(t)$ provides a more comprehensive picture of the accuracy of the quasi-steady model. This is particularly important for the prediction of peak suction events, since the pdf's of surface pressures on all faces of a square cylinder but the front are not normal (Gaussian) (Peterka and Cermak 1975, Ribeiro, 1992 #113). Studies have also shown that the skewness and kurtosis (flatness) varies greatly with the position on the building (Stathopoulos 1980), so that a knowledge of $\mathrm{Cp}_{\mathrm{mean}}$ ($\overline{\mathrm{Cp}}$) and $\mathrm{Cp}_{\mathrm{rms}}$ (σ_{Cp}) is not adequate to predict the expected peak suction.

Weibull, gamma, and log-normal distributions have all been used with reasonable success to represent Cp pdf's for different building pressure time series (Hosoya, et al.

1997). However, data from taps beneath the conical vortices for certain wind directions has displayed a bi-modal distribution (Letchford, et al. 1993, Cochran, 1992 #95) which is not well represented by any of these models. It will be shown in the following section that the various shapes of the Cp pdf's beneath the conical vortices are largely due to instantaneous changes in the wind direction, which are well predicted by quasi-steady theory if Eq. (4.4) is evaluated fully.

4.4.3.1 Calculating the pdf

If both the $(U/\overline{U})^2$ and $\overline{\mathrm{Cp}}(\theta)$ terms in Eq. (4.4) are linearized, then the pdf for Cp(t) becomes Gaussian, since the pdf for q(t) and u(t) are Gaussian (Letchford, et al. 1993). As mentioned above, wind pressures on buildings rarely are Gaussian, so this approximation cannot be considered valid[4].

The pdf of $\mathrm{Cp}^{\mathrm{Q\text{-}S}}(t)$ can be evaluated fully from Eq. (4.4) using the general principal that the probability distribution of a function $z = x{\cdot}y$ can be calculated using the convolution integral

$$f_z(z)dz = \int_{-\infty}^{\infty} f_y(z/x)\cdot f_x(x)dA$$

This can be evaluated discretely as

$$f_z(z_i) = \sum_{x_n=x_{min}}^{x_n=x_{max}} f_y(z_i/x_n)\cdot f_x(x_n)\cdot \ln\left(\frac{x_n+\Delta x}{x_n-\Delta x}\right)$$

where $\Delta x = x_{i+1} - x_i$, and $f_x(x)$=0 for x<x_{min} and x> x_{max}. Applying this to Eq. (4.4) for tap #9 gives

---

[4] Holmes (1981) has shown clearly how the $(U/\overline{U})^2$ term is expected to produce a skewed distribution, so that it is perhaps worth asking why any of a building's pressure taps would register a Gaussian Cp pdf.

$$f_{\mathrm{Cp}^{Q\text{-}S}}(\mathrm{Cp}_i^{Q-S}) = \sum_{\mathrm{C\overline{p}}(\theta)_n=-2.3}^{\mathrm{C\overline{p}}(\theta)_n=-0.4} f_{(U/\overline{U})^2}(\mathrm{Cp}_i^{Q-S}/\mathrm{C\overline{p}}(\theta)_n)\cdot f_{\mathrm{C\overline{p}}(\theta)}(\mathrm{C\overline{p}}(\theta)_n)\cdot \ln\left(\frac{\mathrm{C\overline{p}}(\theta)_n+\Delta\mathrm{C\overline{p}}(\theta)}{\mathrm{C\overline{p}}(\theta)_n-\Delta\mathrm{C\overline{p}}(\theta)}\right) \quad (4.14)$$

so that, for example, the probability that $\mathrm{Cp}^{Q\text{-}S}$ = -1 is the sum of the weighted probabilities that when Cp(θ)=-1, $(U/\overline{U})^2 = 1$, and when Cp(θ) = -1.5, $(U/\overline{U})^2 = 0.67$, etc.

The pdf's $f_{(U/\overline{U})^2}$ and $f_{\mathrm{C\overline{p}}(\theta)}$ can be calculated from the Gaussian pdf's of *U(t)* and *θ(t)*. In general, if x is a function of ξ, and ξ has a known pdf $f_\xi(\xi)$, then

$$f_x(x) = \frac{f_\xi(\xi_1)}{|x'(\xi_1)|} + \frac{f_\xi(\xi_2)}{|x'(\xi_2)|} + \ldots + \frac{f_\xi(\xi_n)}{|x'(\xi_n)|} \quad (4.15)$$

where the x' is the partial derivative of x with respect to ξ, and n is the number of different roots for a given value of x. Applying Eq. (4.15) to the function $\mathrm{C\overline{p}}^{\mathrm{inst}\theta}$ for σ_θ=10° from Fig. 4.7 resulted in anywhere from two to four roots. For example, since $\mathrm{C\overline{p}}^{\mathrm{inst}\theta}$ = -2 for both θ = 72° and θ = 49°, $f_{\mathrm{C\overline{p}}(\theta)}(-2)$ would have two roots, so that the probability that Cp=-2 is the sum of the weighted probabilities that θ = 72° or θ = 49°. (This is the procedure that was used to derive the f_{Cp}(Cp) pdf in Fig. 4.6). Fig. 4.9 shows the $f_{\mathrm{C\overline{p}}(\theta)}$ curves for tap #9 that were calculated for various nominal wind angles using a Gaussian pdf with σ_θ= 10° for $f_\theta(\theta)$. The sharp peaks are the result of small Cp′(θ) values at the various $\mathrm{C\overline{p}}^{\mathrm{inst}\theta}$ maxima and minima. Of particular interest is $f_{\mathrm{C\overline{p}}(\theta)}$ for ω_{nom} = 45°, which has peaks at Cp = -0.3 and -2.35. This is essentially what causes the bimodal behaviour of f_{Cp}; this will be discussed further later in this paper.

Also shown are selected $f_{\overline{\mathrm{Cp}}(\theta)}$ curves derived from applying Eq. (4.15) to curve fits of the measured $\overline{\mathrm{Cp}}^{\mathrm{inst}\theta}_{\mathrm{meas}}(\theta)$ values of Fig. 4.7. As expected, these pdf's agree fairly well with those calculated from the predicted $\overline{\mathrm{Cp}}^{\mathrm{inst}\theta}$ curves for $\omega < 50°$, but do not agree for $\omega > 60°$. In particular, the pdf for $\omega_{\mathrm{nom}} = 85°$ appears as a narrow spike at $\mathrm{Cp}(\theta) = 1.5$, because $\overline{\mathrm{Cp}}^{\mathrm{inst}\theta}_{\mathrm{meas}}$ is almost independent of ω for this wind angle.

Eq. (4.15) can also be used to derive $f_{(U/\bar{U})^2}$ from f_U. In this case, there is only one root, so that

$$f_{(U/\bar{U})^2} = \frac{\bar{U}^2}{2}\frac{f_U(U)}{U} = \frac{\bar{U}^2}{2U\sigma_U\sqrt{2\pi}}\exp\left(\frac{-U^2}{2\sigma_U^2}\right)$$

Combining $f_{(U/\bar{U})^2}$ with the $f_{\overline{\mathrm{Cp}}(\theta)}$ curves in Fig. 4.9 as described in Eq. (4.14) produces the pdf's shown in Fig. 4.10. These are compared to histograms of the experimental data. Note that $\overline{\mathrm{Cp}}(\theta) = \overline{\mathrm{Cp}}^{\mathrm{inst}\theta}(\theta)/(1 + I_U^2)$ was used to determine $f_{\overline{\mathrm{Cp}}(\theta)}$, as advised in Eq. (4.10). Also shown in Fig. 4.10 are selected Gaussian pdf's calculated using the mean and rms from the experimental data, as well as selected Cp pdf's calculated from the measured $\overline{\mathrm{Cp}}^{\mathrm{inst}\theta}_{\mathrm{meas}}(\theta)$ that were shown in Fig. 4.9. Fig. 4.10(b) presents the same data on a semilog scale, which allows a better look at the tails of the pdf's.

4.4.3.3 *Quasi-steady inaccuracy near* $\overline{\mathrm{Cp}} = 0$.

Eq. (4.4) does not allow the possibility that $\mathrm{Cp}(t) > 0$ for tap #9, since $\overline{\mathrm{Cp}}(\theta)$ is never > 0. The data indicate, however, that $\mathrm{Cp}(t)$ does occasionally become positive, especially when $|\overline{\mathrm{Cp}}(\theta)|$ becomes small, such as for $\omega < 30°$. This is at least partly due to the nature of the static pressure fluctuations in the wind tunnel.

Static pressure time series were simultanesouly measured during this experiment using pressure taps on the walls of the tunnel, as well as pitot tubes at model height and 1.5m above the tunnel floor. These measurements indicate the presence of static pressure fluctuations at these various locations which were correlated at low frequencies, but which were not correlated to the flow velocity. Applying this knowledge to the analysis in section 5.1 yields the equation

$$\begin{aligned}\mathrm{Cp_M}(t) &= \frac{p_M^{static}(t) - p_{ref}^{static}(t)}{\frac{1}{2}\rho\left(\overline{U}_{ref}\right)^2} + \frac{p_M^{static\_random}(t) - p_{ref}^{static\_random}(t)}{\frac{1}{2}\rho\left(\overline{U}_{ref}\right)^2} \\ &= \mathrm{Cp_M^{Q\text{-}S}}(t) + \mathrm{Cp_M^{s\text{-}r}}(t)\end{aligned}$$

$\mathrm{Cp_M^{s\text{-}r}}(t)$ was measured by comparing the static pressure fluctuations between the various locations mentioned above. It has a normal distribution with $\overline{\mathrm{Cp}}_{\mathrm{M}}^{\mathrm{s\text{-}r}} = 0$ and $\sigma_{\mathrm{Cp^{s\text{-}r}}} = 0.12$ (see Fig. 4.11). As a result, it has little influence on larger |Cp| values, but will change the pdf for small |Cp| values. The changes can be calculated with the convolution integral

$$f_{Cp}(Cp) = \int_{Cp_{min}^{Q-S}}^{Cp_{max}^{Q-S}} f_{Cp^{s-r}}(Cp - Cp^{Q-S}) \cdot f_{Cp^{Q-S}}(Cp^{Q-S})\, dCp^{Q-S}$$

This additional calculation was performed for all of the plots in Fig. 4.10; an example of the changes to the pdf is shown in Fig. 4.11(b) for $\omega_{nom} = 25°$.

4.4.3.3 Discussion of pdf shape

Both the predicted and the measured histogram of Cp(t) for tap #9 when ω_{nom} = 45° shows two peaks, an abrupt one at Cp = 0.5 and the more gradual peak at Cp = 1.2 (see Fig. 4.11). This is the result of the extreme bimodal nature of $f_{\overline{\mathrm{Cp}}(\theta)}$ for $\omega_{nom} = 45°$.

When $\omega(t) < 20°$, tap #9 is generally beyond the reattachment point, and so has Cp ≈ $\mathrm{Cp_a}$. For $\omega(t) > 30°$, the tap is typically beneath the zone of flow separation, and lower Cp's are evident. The bimodal distribution is the result of the tap being intermittently inside the separated flow zone, where a Cp pdf like that for $\omega_{nom} = 65°$ dominates, and outside the separated flow, where a Cp pdf like that for $\omega_{nom} = 25°$ dominates. Another way to think of the bimodal distribution is that it is the halfway point of the histogram transition from having a peak at Cp = -0.4 and Cp = -2. This is perhaps more evident in the log plots, as the negative tail rise up as ω_{nom} increases.

The change in the position of the reattachment and the vortex core is largely due to the change in the instantaneous wind angle. This is well modeled by the quasi-steady theory, especially for $\omega(t) < 50°$, as is evident in Figs. 4.7 and 4.9. The results is that the quasi-steady prediction of $f_{\overline{\mathrm{Cp}}(\theta)}$ match the measured histograms well for $\omega(t) < 50°$, as seen in Fig. 4.10(a). However, the quasi-steady prediction $f_{\overline{\mathrm{Cp}}(\theta)}$ for $\omega(t) > 60°$ is much less accurate, as was seen in Fig. 4.9. This has surprising little effect on the overall pdf, which on the linear plot (Fig 4.10(a)) matches the data fairly well. This is because of the dominance of the $f_{(u/\bar{U})'}$ distribution, which might be expected in this region, given the dominance of $\mathrm{Cprms\_{TI}}$ seen in Fig. 4.8 for these wind angles.

When viewed on a log scale in Fig. 4.10(b), the quasi-steady predictions made using the single predicted $\overline{\mathrm{Cp}}^{\mathrm{inst}\theta}$ curve actually show a better agreement with the data histograms than the predictions made with the measured $\overline{\mathrm{Cp}}^{\mathrm{inst}\theta}_{\mathrm{meas}}(\theta)$ curves. This could also have been anticipated from Fig. 4.8, where the over-prediction of $\mathrm{Cprms\_{\theta inst}}$, as compared to $\mathrm{Cprms\_{\theta meas}}$, compensates for the absence of a $\mathrm{Cprms\_{\omega'}}$ term.

The vortex motion which is expressed by the ω' term is not included in the quasi-steady model. As a result, the quasi-steady theory is bound to underestimate the frequency of peak suction events, since these events are tied to the presence of the vortex core above the tap. In the quasi-steady model, this can only occur during a shift in wind direction, while in fact random core motion can move the vortex over the tap for any wind direction. This is why the quasi-steady model, when using actual $\overline{Cp}^{\mathrm{inst}\theta}_{\mathrm{meas}}(\theta)$ data in Eq. (4.10), does such a good job of predicting the peak suctions for $\omega(t) = 65$, when the core's mean position is above the tap, but under-predicts the peaks for other wind directions. (Witness the shaded regions in Fig.4.10(b))

For $\omega(t)$ <30° and $\omega(t)$ >70°, this under-prediction is compensated for in simple quasi-steady theory by the over-prediction of the effects of σ_θ by the use of $\overline{Cp}^{\mathrm{inst}\theta}$ curve in Eq. (4.10), which falsely predicts that a shift in instantaneous wind direction to $\omega(t) =$ 65 produces the same suction regardless of ω_{nom}.

4.5 Conclusions

When evaluated fully, the quasi-steady theory captures the main charateristics of the distribution of pressures for taps beneath the conical vortices during cornering winds, including skewed and bimodal distributions. This is largely because fluctuations in the local velocity are passed directly to the surface by the conical vortex, and the $(U/\overline{U})^2$ term dominates. It is also because, for cornering winds, instantaneous changes in wind direction have a similar effect on the vortex to long term changes in wind direction, which is the fundamental assumption of quasi-steady theory.

However, as the mean wind direction becomes more normal to the roof walls, the vortex no longer responds in a quasi-steady manner, so that instantaneous changes in wind direction do not have the same effect as long term changes. As a result, the quasi-steady theory over-predicts surface pressures changes based on wind direction fluctuations. This indicates that the quasi-steady theory is ill-suited to modeling pressures beneath bubble separation.

Finally, the quasi-steady theory does not consider the effects on surface pressure of vortex motion not attributable to shifts in wind direction. Quasi-steady theory requires a shift in wind angle to a specific direction for the vortex to pass over a tap, but random vortex motion makes it possible for the vortex to pass over a tap for any instantaneous wind direction. Since it is the presence of the vortex above a tap which is responsible for the peak suction, quasi-steady theory underpredicts the peaks for most wind angles.

The combination of pressure peak under-prediction due to neglecting random vortex motion and over-prediction due to overestimating the effects of wind direction changes can produce correct predictions (as for tap #9 at $\omega_{nom} = 25°$), but will also under-predict peak pressures for crucial wind angles (such as $\omega_{nom} = 55°$).

It is also possible that the random vortex motion is more pronounced on full scale structures than for wind tunnel tests, since studies continue to show that peak and rms pressures are higher for full scale tests than for model-scale wind tunnel studies.

4.6 References

Calderone, I., Cheung, J. C. K., and Melbourne, W. H. (1994), "The full-scale significance on glass cladding panels, of data obtained from wind tunnel measurements of pressure fluctuations on building cladding", J. Wind Eng. Ind. Aerodyn., 53, 247-259.

Cook, N. J. (1990), The designer's guide to wind loading of building structures, part 2: static structures, Building Research Establishment Report, Garston, UK

Geurts, C. P. W. (1996), "Full-scale and wind-tunnel measurements of the wind and wind-induced pressures over suburban terrain", J. Wind Eng. Ind. Aerodyn., 64, 89-100.

Geurts, C. P. W., Rutten, H. S., and Wisse, J. A. (1997), "Spectral characteristics of wind induced pressures on a full scale building in suburban terrain", J. Wind Eng. Ind. Aerodyn., 69-71, 609-618.

Holmes, J. D. (1981), "Non-Gaussian characteristics of Wind Pressure Fluctuations", J. Wind Eng. Ind. Aerodyn., 7, 103-108.

Hosoya, N., Cermak, J. E., and Peterka, J. A. (1997), "Probabilistic Analysis of Area-Averaged Pressures on Model TTU Building", 8th US national conference on Wind Engineering, Baltimore MD,

Hoxey, R. P., Richards, P. J., Richardson, G. M., Robertson, A. P., and Short, J. L. (1995), "The Silsoe structures building: the completed experiment part 2", 9th International Conference on Wind Engineering, New Delhi, India,

Hoxey, R. P., and Robertson, A. P. (1994), "Pressure coefficients for low-rise building envelopes derived from full-scale experiments", J. Wind Eng. Ind. Aerodyn., 53, 283-297.

Kawai, H. (1983), "Pressure fluctuations on square prisms - Applicability of strip and quasi-steady theories", J. Wind Eng. Ind. Aerodyn., 13, 197-208.

Kawai, H., and Nishimura, G. (1996), "Characteristics of fluctuating suction and conical vortices on a flat roof in oblique flow", J. Wind Eng. Ind. Aerodyn, 60, 211-225.

Letchford, C. W., Iverson, R. E., and McDonald, J. R. (1993), "The application of the Quasi-Steady theory to full scale measurements on the Texas Tech Building", J. Wind Eng. Ind. Aerodyn., 48, 111-132.

Letchford, C. W., and Marwood, R. (1997), "On the influence of v & w component turbulence on roof pressures beneath conical vortices", J. Wind Eng. Ind. Aerodyn., 69-71, 567-577.

Li, Q. S., and Melbourne, W. H. (1995), "An experimental investigation of the effects of free-stream turbulence on streamwise surface pressures in separated and reattaching flows", J. Wind eng. Ind Aerodyn., 54/55, 313-323.

Maier-Erbacher, J., and Plate, E. J. (1991), "Measurement of velocity near and pressure on a cylindrical tower located on irregular terrain", J. Wind Eng. Ind. Aerodyn., 38, 167-184.

Melbourne, W. H. (1993), "Turbulence and the Leading Edge Phenomena", J. Wind Eng. Ind. Aerodyn., 49, 45-64.

Papoulis, A. (1984), Probability, random variables, and stochastic processes, McGraw-Hill Book company, New York

Peterka, J. A., and Cermak, J. E. (1975), "Wind pressures on Buildings- Probability Densities", Journal of the Structural Division, ASCE, 101(No. ST6), 1255-1267.

Richards, P. J., Hoxey, R. P., and Wanigaratne, B. S. (1995), "The effect of directional variations on the observed mean and rms pressure coefficients", J. Wind Eng. Ind. Aerodyn., 54/55, 359-367.

Saathoff, P. J., and Melbourne, W. H. (1989), "The generation of peak pressures in separated/ reattaching flows", J. Wind Eng. Ind. Aerodyn., 32, 121-134.

Sankaran, R., and Jancauskas, E. D. (1993), "Measurements of cross-correlation in separated flows around bluff cylinders", J. Wind Eng. Ind. Aerodyn., 49, 279-288.

Stathopoulos, T. (1980), "PDF of Wind Pressures on Low-Rise Buildings", Journal of the Structural Division, ASCE, 106(No. ST5), 973-990.

Tieleman, H. W., and Hajj, M. R. (1995), "Pressures on a flat Roof- application of Quasi-Steady Theory", 1995 ASCE Engineering mechanics conference, Boulder, Co,

Uematsu, Y., and Isyumov, N. (1998), "Peak gust pressures acting on the roof and wall edges of a low-rise building", J. Wind Eng. Ind. Aerodyn., 77&78, 217-231.

4.7 Figures

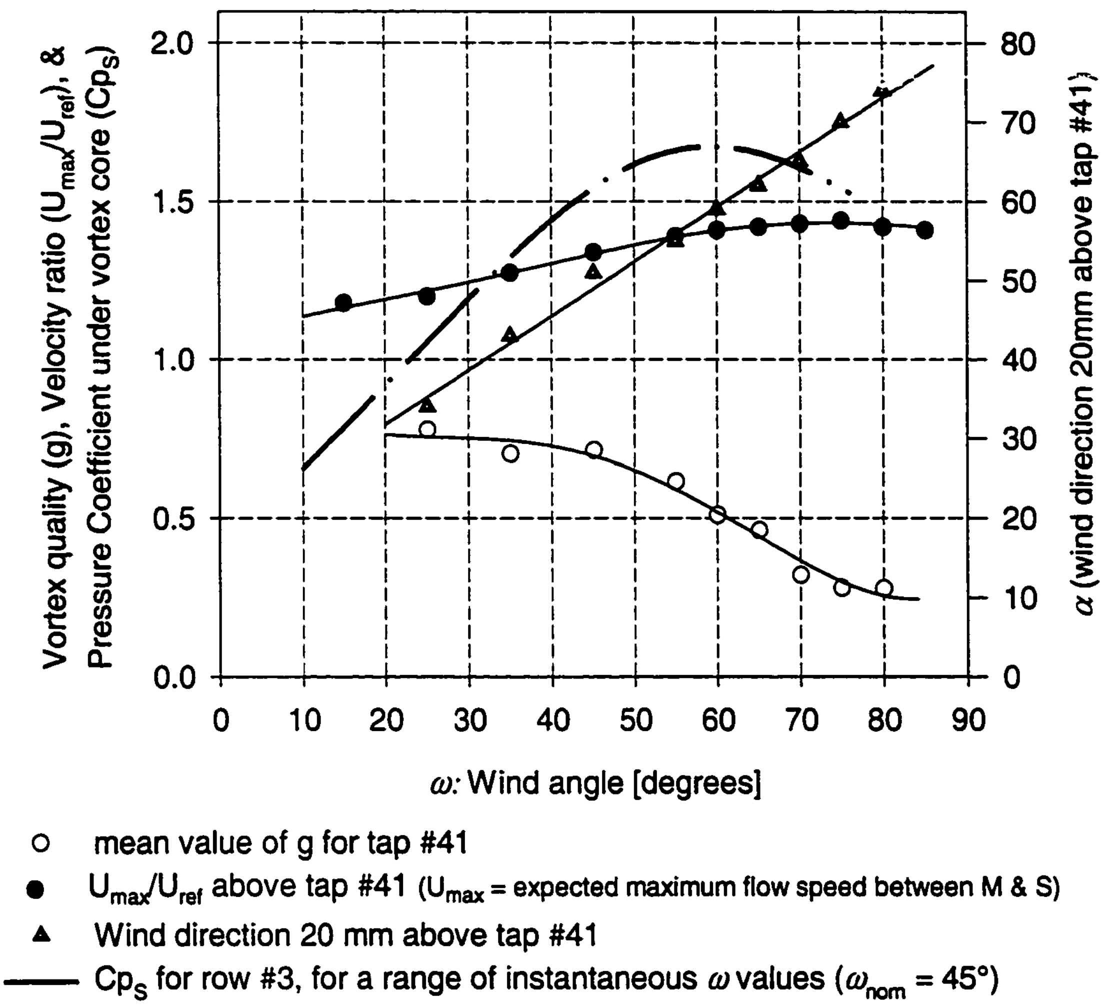

Figure 4.1: Examples of the dependence of the parameters of Eq. (5) on wind direction

Comments on the data in Figure 4.1:

- For g, U_{max}/U_{ref}, & α:
  - ω-axis represents the nominal wind direction, $\overline{\omega(t)}$; The data is taken from a series of wind vector measurements using a hot-wire probe placed at several different heights above tap #41.
  - These curves are from conditionally sampled data: Only the velocities recorded when tap#41 measures the minimum Cp in row #3 were used in these averages.
- For Cps: ω-axis represents the instantaneous wind angle. The minimum values of Cp for all taps in row #2 for every concurrent sample are selected, then grouped by concurrent wind direction and averaged.

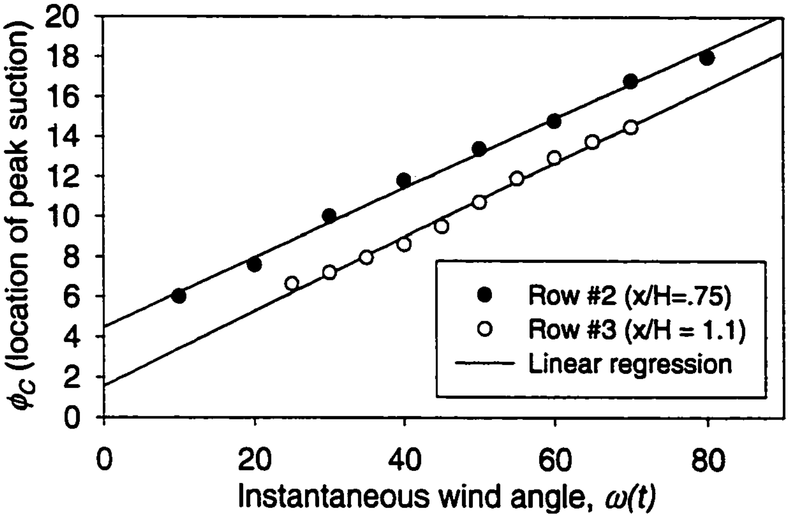

Figure 4.2: Position of vortex core as a function of wind direction, showing core angle dependence on distance from apex.

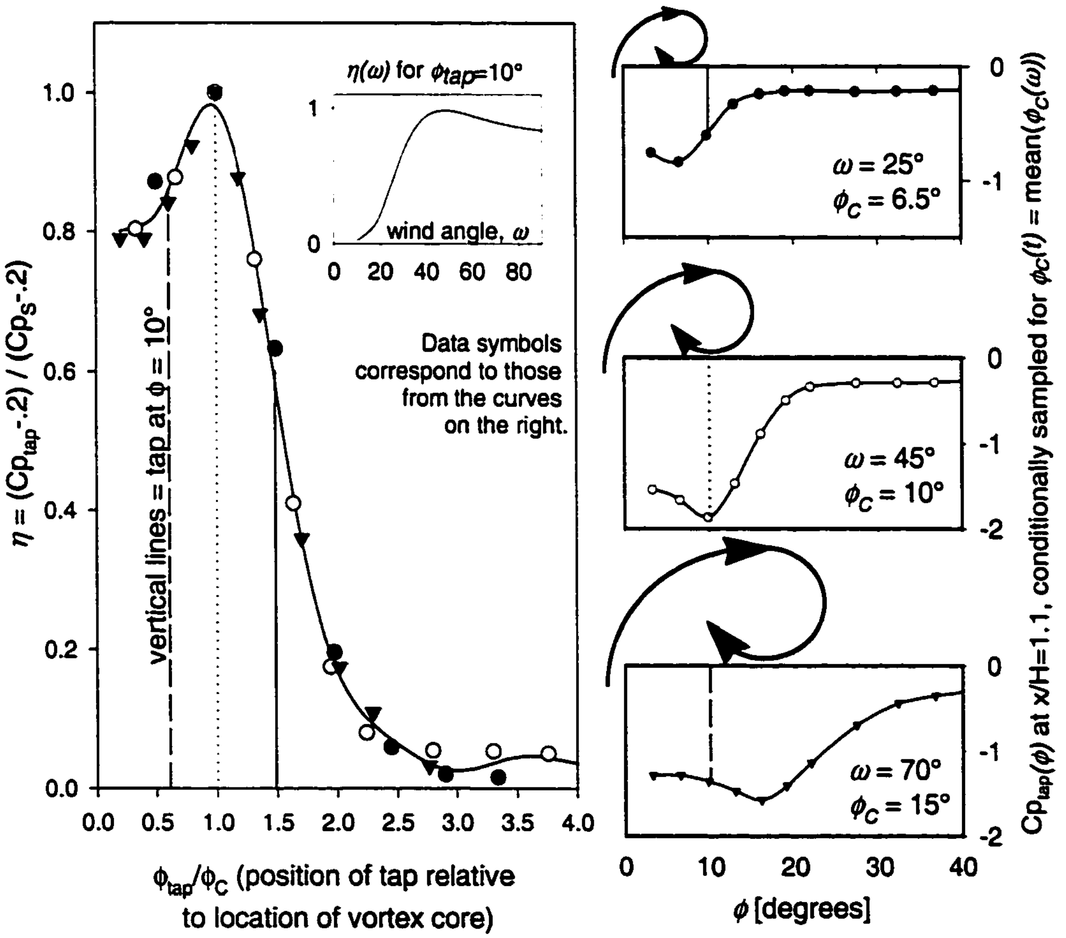

Figure 4.3: Calculation of Cp(ω) at a given tap using the mean Cp profile and the location of the tap relative to the location of the vortex core for each wind direction ω.

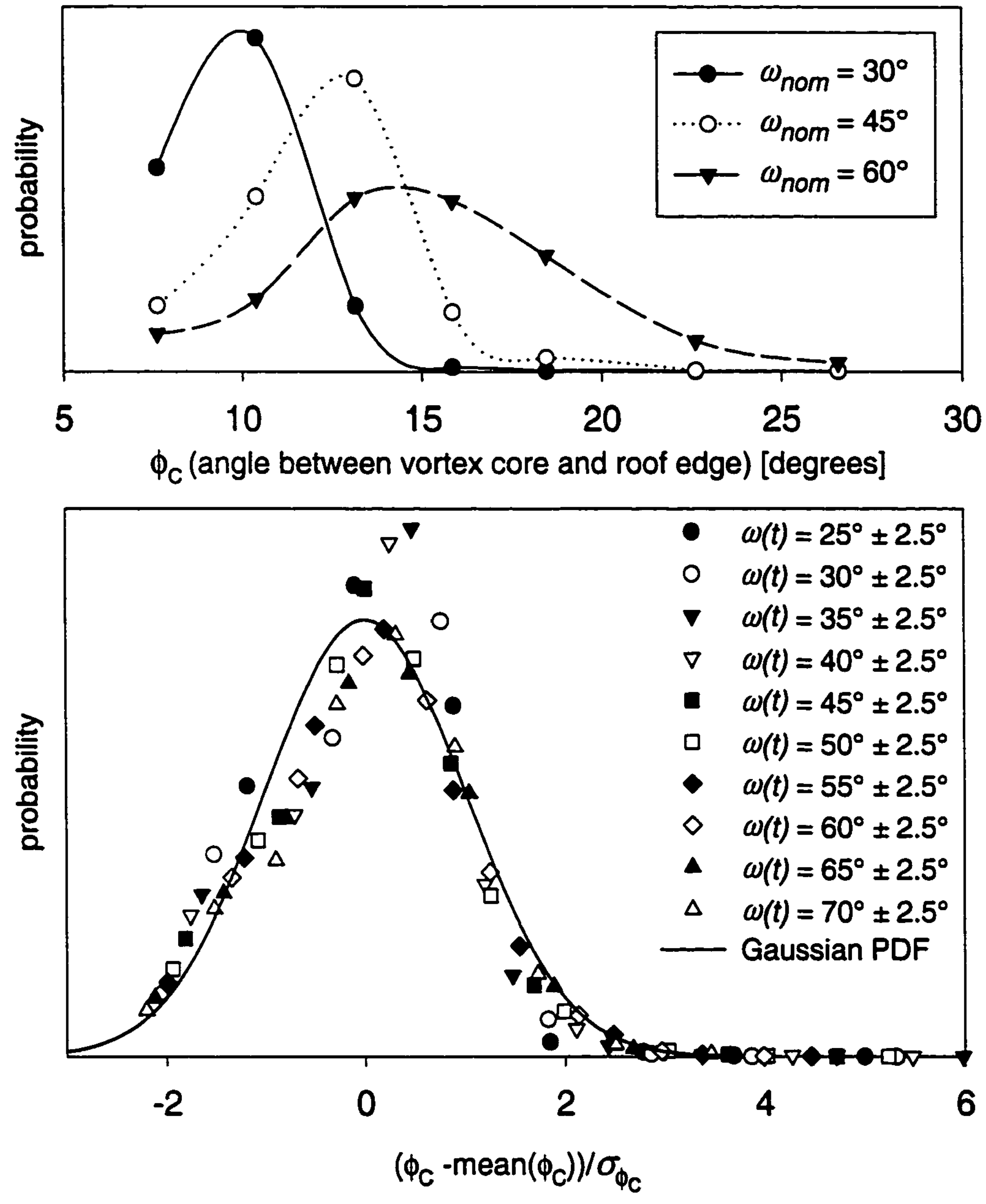

Figure 4.4: Random vortex core motion for various instantaneous wind angles.

- Core position is determined by the location of the peak suction.
- All data are from a run with a nominal wind angle of 45°
- The instantaneous wind vector is measured 16mm above tap #41.
- Data is from row #2 (taps 12-18)

(See the Section 3.2 for more information on how this data was gathered)

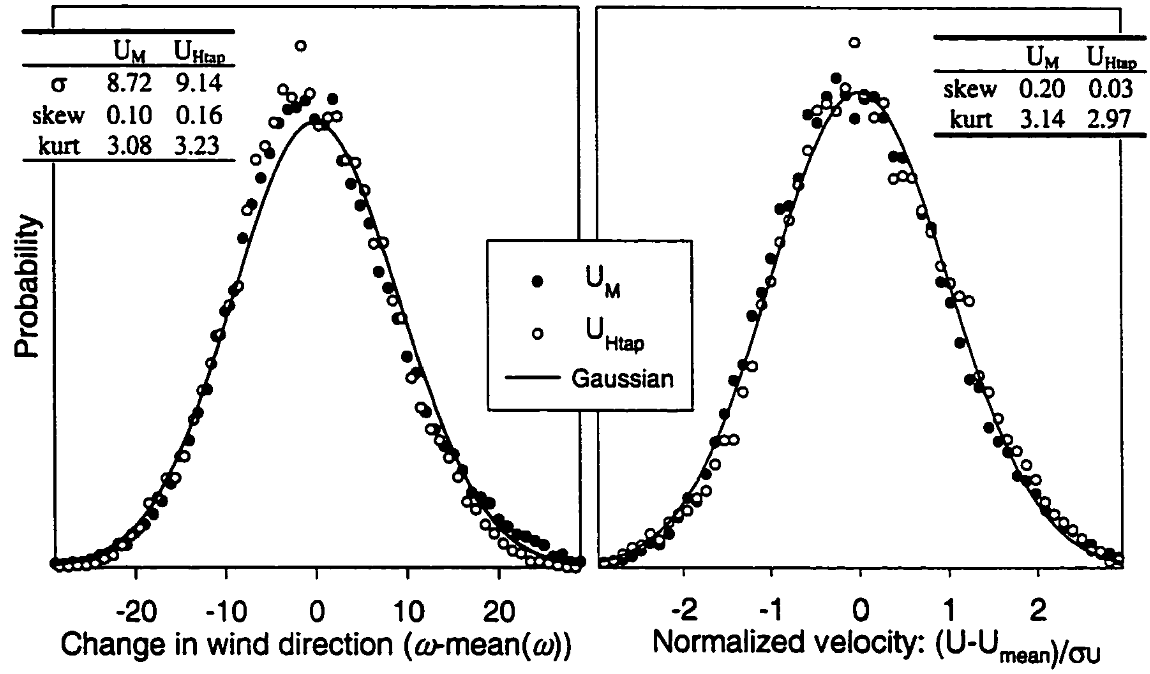

Figure 4.5: Probability distributions for:

● $U_M(t)$: Wind vector 16 mm above tap #40 (conditionally sampled for peak suction at tap #40)

o $U_{Htap}(t)$: wind vector at roof height when building model has been removed from the tunnel.

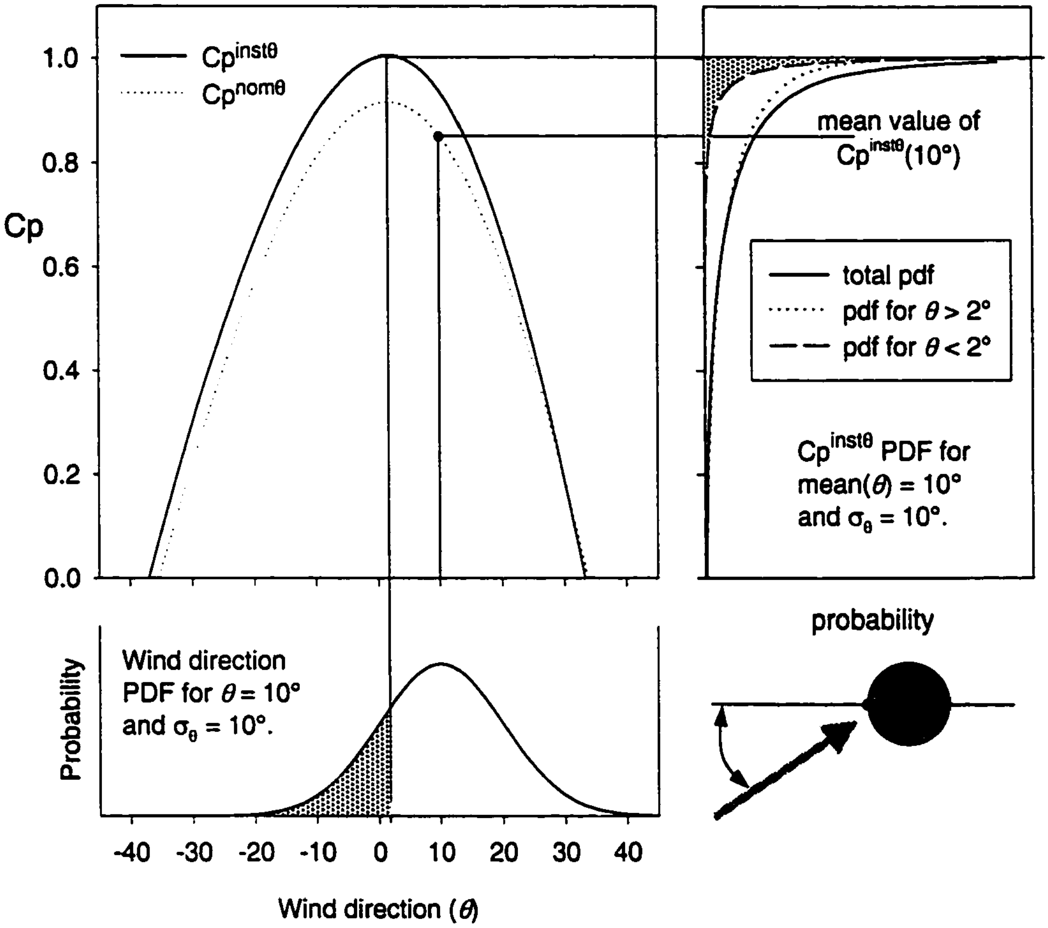

Figure 4.6: Instantaneous (theoretical) and mean (measured) Cp(θ) curves for a tap on the front face of a tower. Also shown is the Cp(t) probability distribution for a nominal wind direction of 10°.

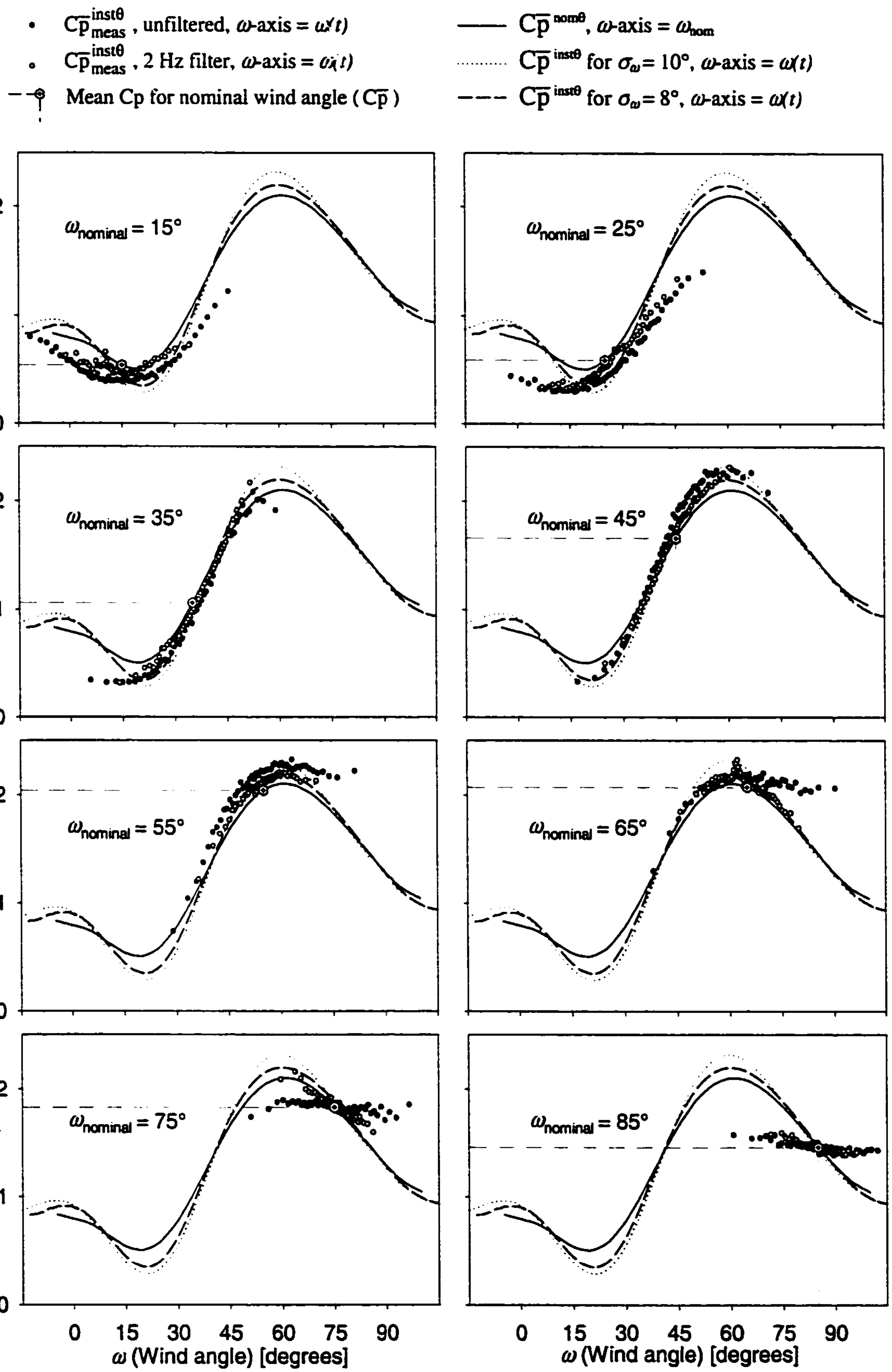

Figure 4.7: Testing the quasi-steady assumption of wind angle dependence

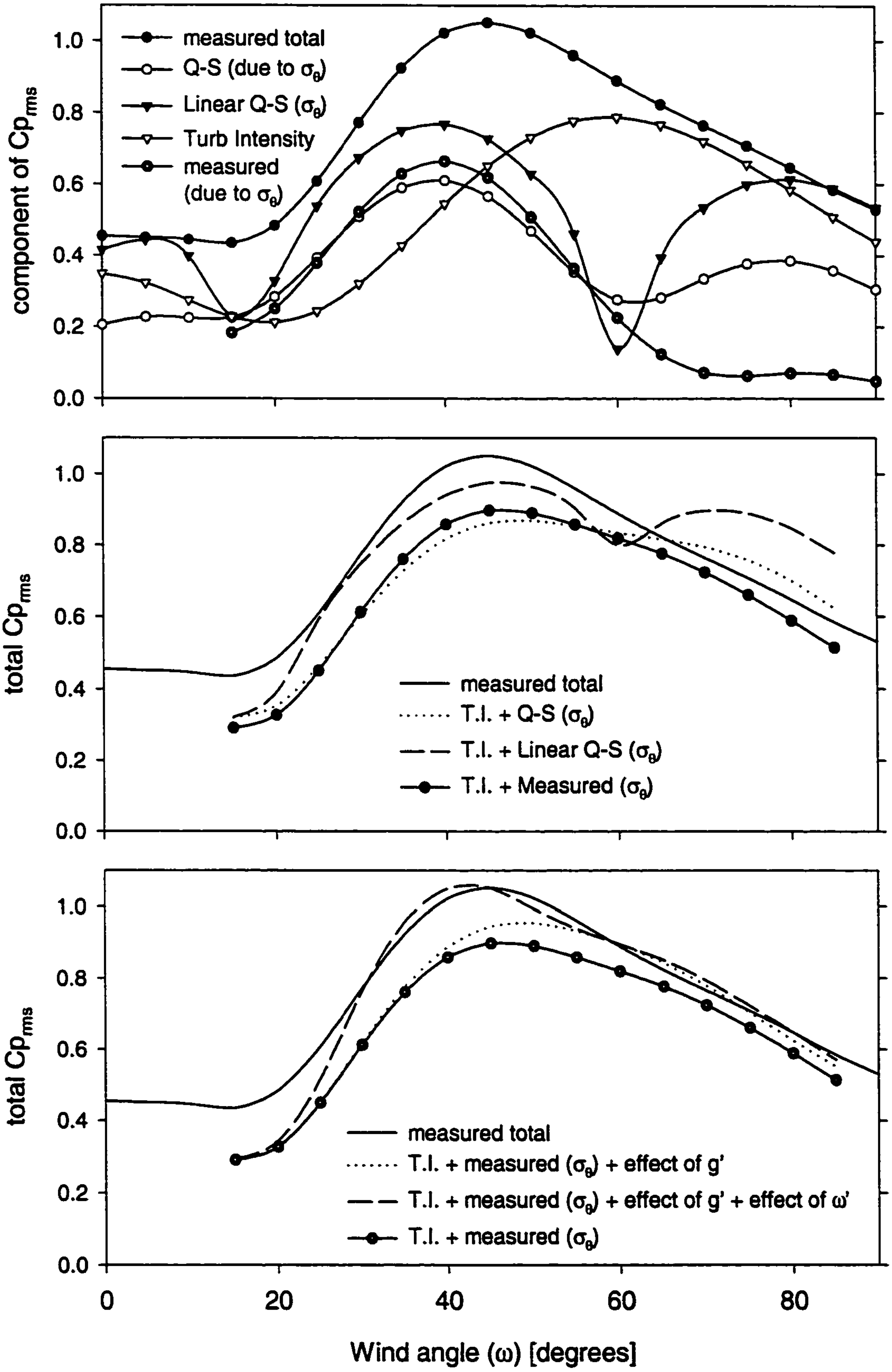

Figure 4.8: Components of Cp_{rms} for tap #9

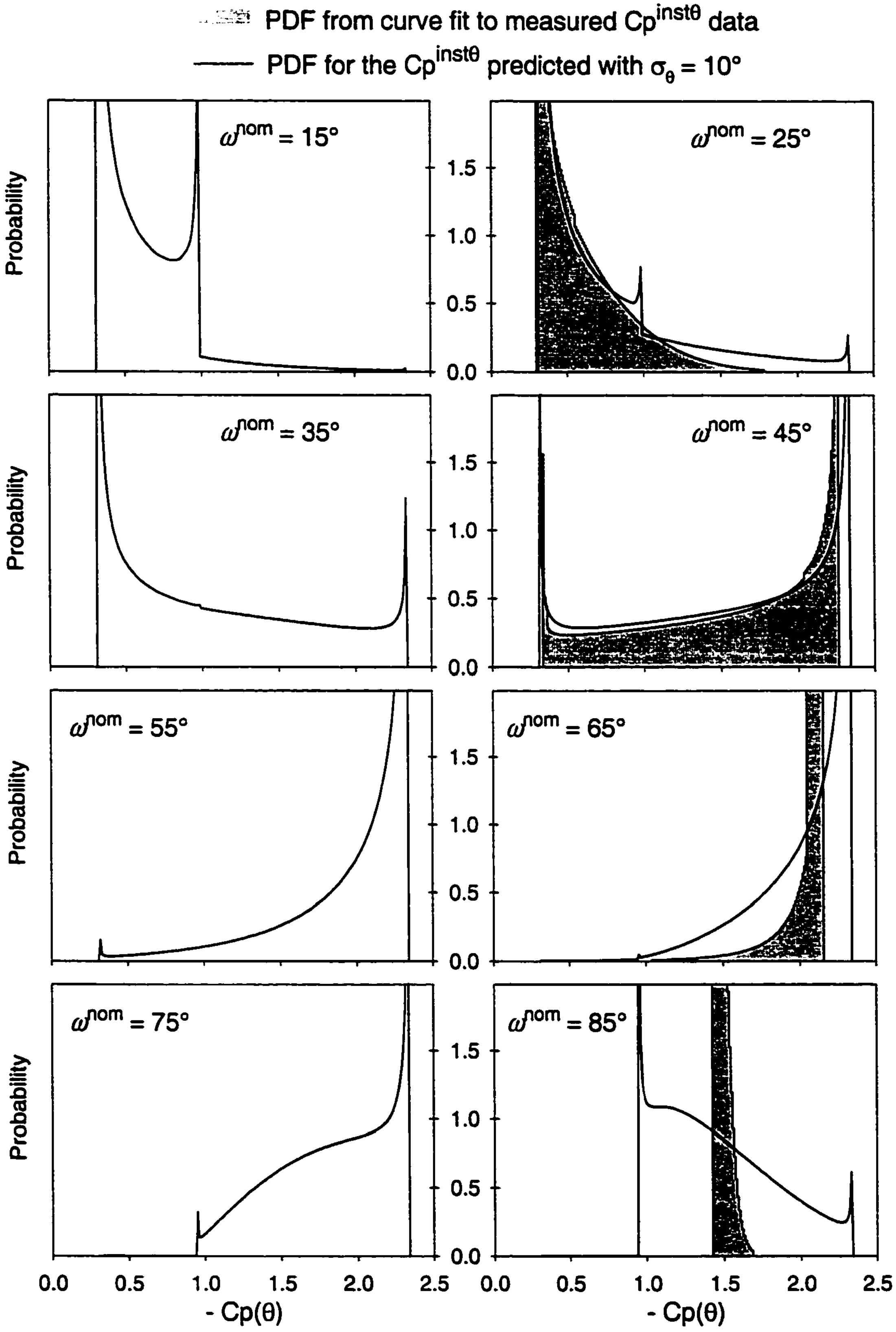

Figure 4.9: Probability distributions of Cp(θ) at tap #9 for various nominal wind directions

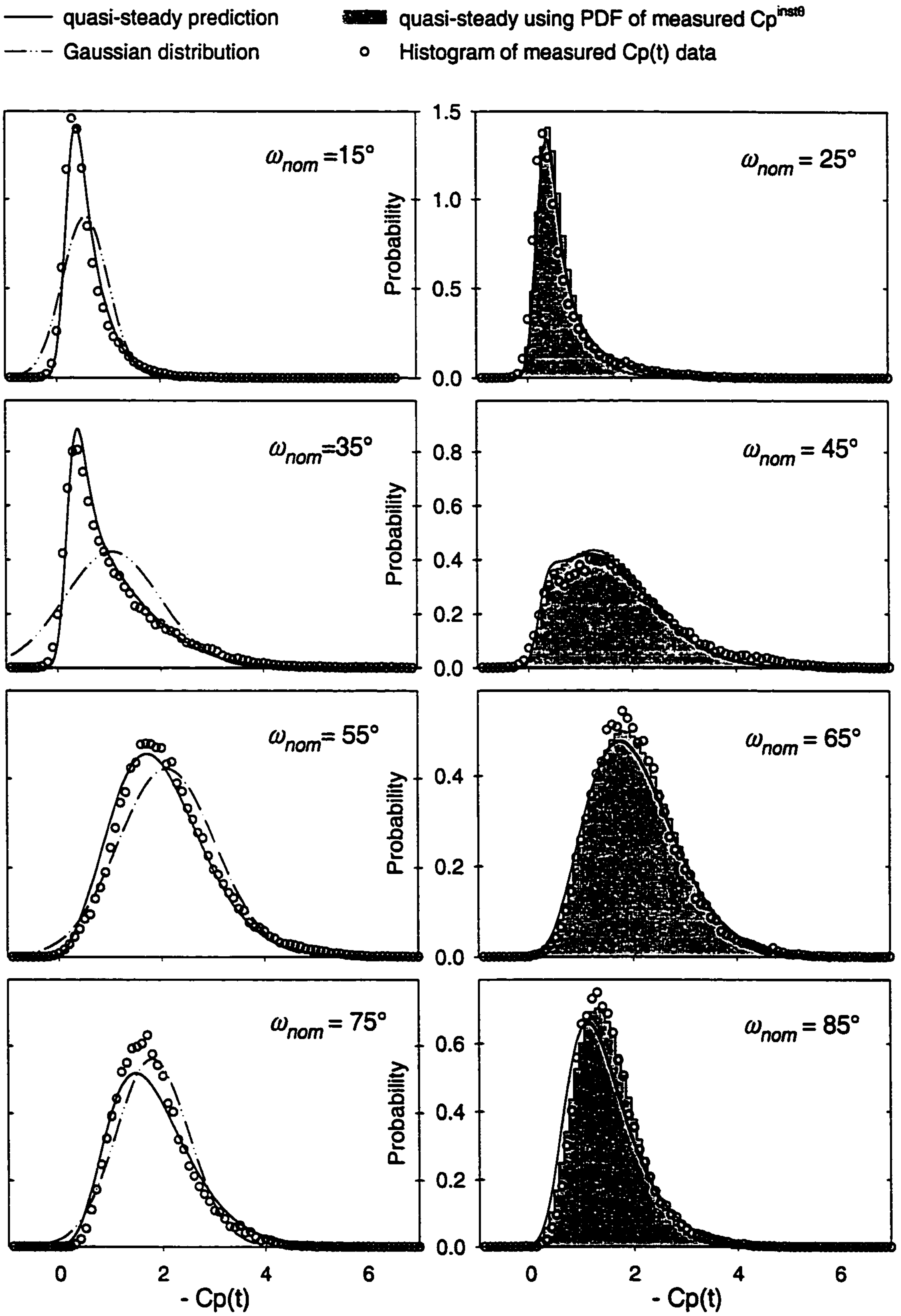

Figure 4.10: Probability distributions of Cp(t) at tap #9 for various nominal wind directions
(a) Linear plots

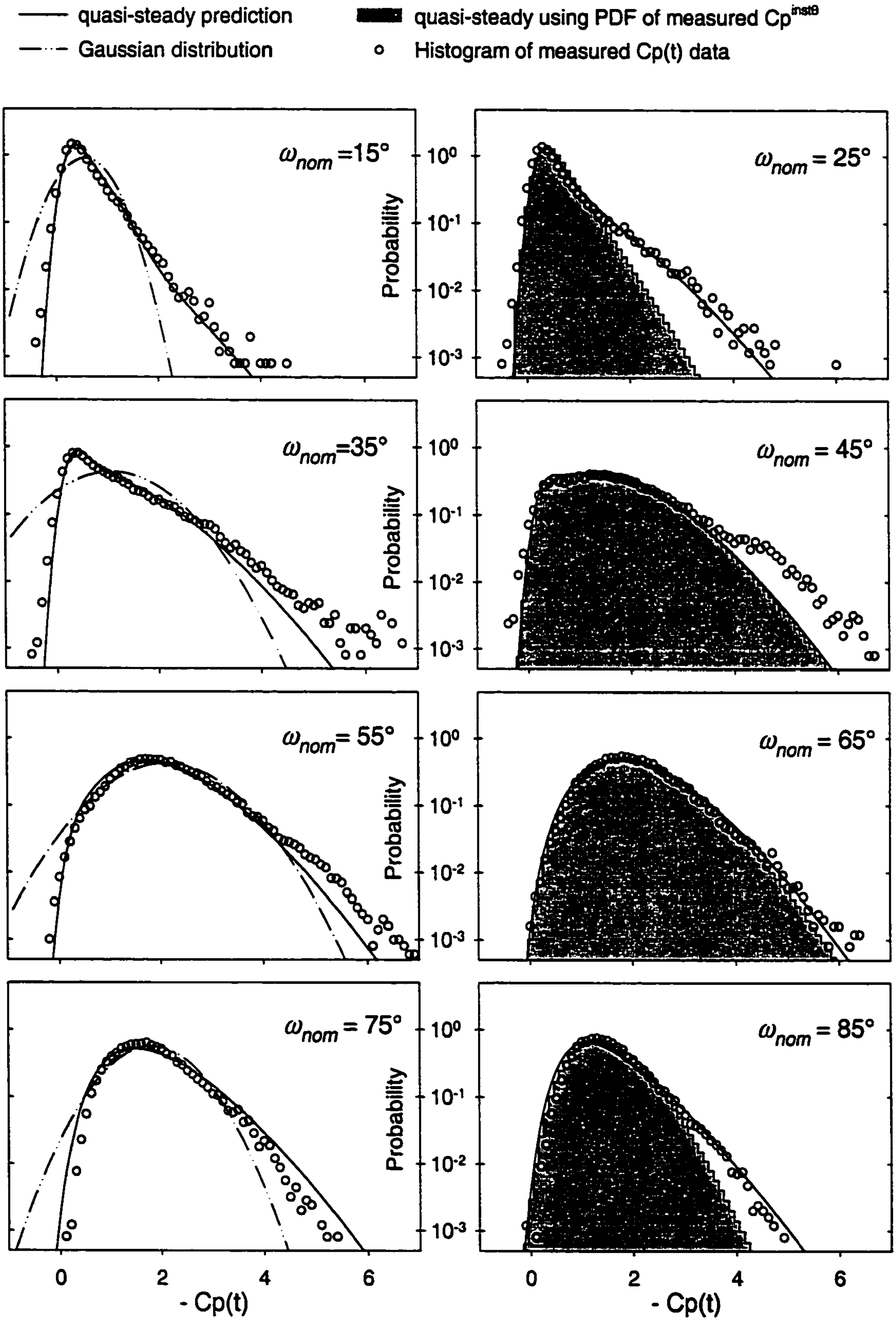

Figure 4.10 (Continued)
(b) Log plots

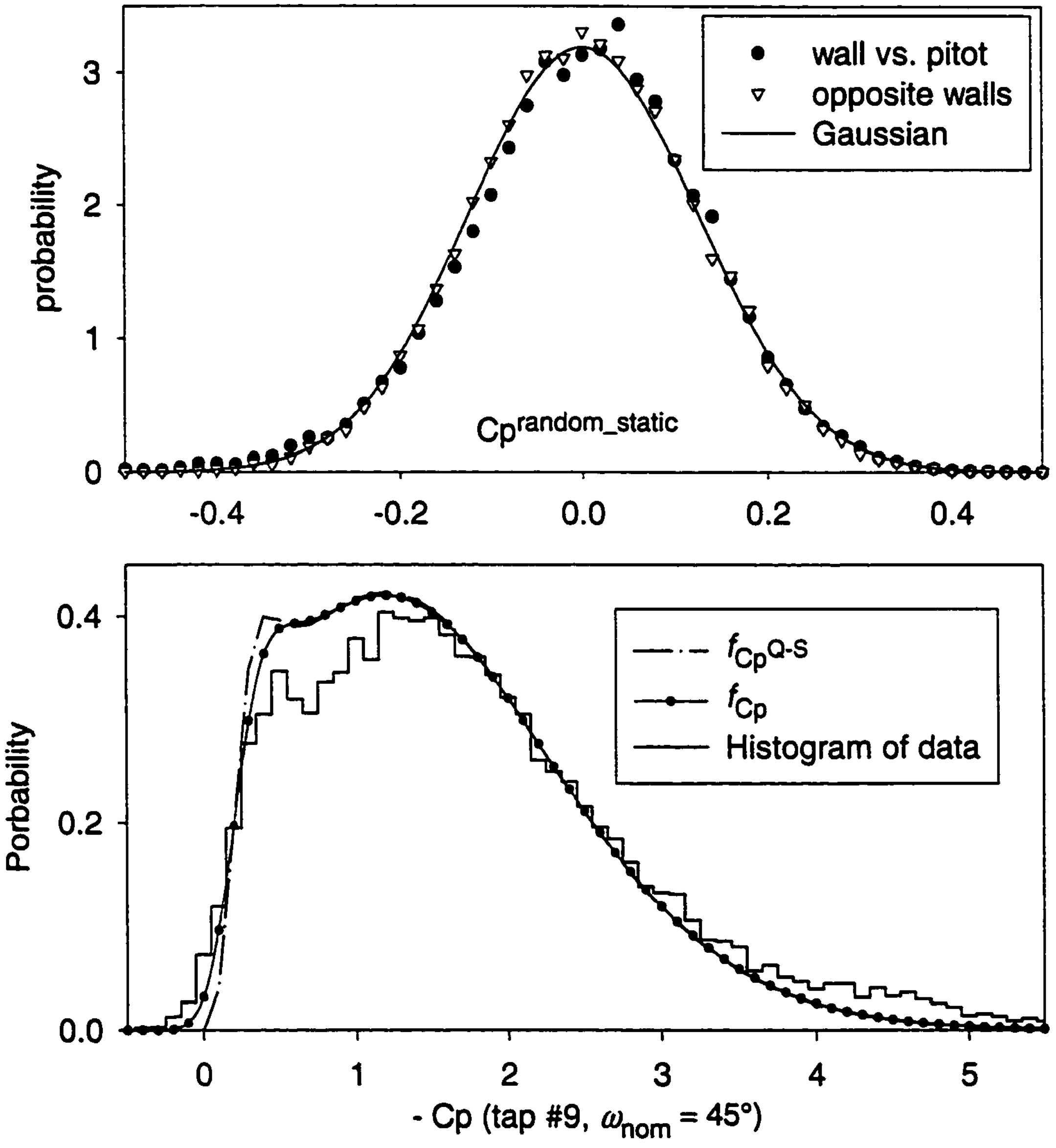

Figure 4.11: Effect of random static pressure fluctuations on pdf of Cp for tap #9, at a nominal wind direction of 45°.

CHAPTER 5: THE MITIGATION OF VORTEX INDUCED ROOFTOP SUCTION

Most of the material in Chapter 5 is to be presented at the Fourth International Colloquium on bluff body Aerodynamics and Applications, at the Ruhr-University of Bochum, Germany.

5.1 Introduction

The worst mean and peak suctions on low-rise building roofs, whether flat, gabled, hipped, or mono-sloped, occur beneath the separated flow along the leading edges (Lin, et al. 1995, Stathopoulos, et al. 1996, Xu and Reardon 1998). To give some idea of the magnitude of these suctions, a simple calculation of lift beneath a single conical vortex has been performed using the relationship established by Lin, et al. (1995), $\mathrm{Cp_S}(x) = \mathrm{Cp_S}(x_0)/\sqrt{x/x_0}$. This relationship is compared in Fig. 5.1 to a typical instantaneous pressure peak, taken from data measured at CSU on a 1:25 TTU model. The comparison is favorable, with $\mathrm{Cp_S}(x_0 = 1\mathrm{m}) = -8$. The lift force can now be calculated as

$$\begin{aligned} F_{corner} &= q\int \mathrm{Cp_S}(x,y)dA = q\int \mathrm{Cp_S}(x)\cdot 0.75\cdot y(x)/2dx \\ F_{corner}(x_1) &= q\int_0^{x_1} \mathrm{Cp_S}(x_0)\sqrt{x_0/x}\,\frac{x\tan(\theta_r)}{2}dx = q\cdot \mathrm{Cp_S}(x_0)\cdot\tan(\theta_r)\cdot\sqrt{x_0}\cdot x_1^{1.5}/4 \end{aligned} \tag{5.1}$$

where F_{corner} is the total lift force relative to Cp = 0 caused by the vortex for the triangular roof region delineated by reattachment line (θ_r), the roof edge, and the line $x = x_0$. The reattachment in Fig. 5.1 can be considered complete at $\theta_r = 25°$.

Ten-minute wind speed averages of 30 m/s have been measured in tropical storms at 9.1m above the ground (Simiu and Scanlan 1986), so that U_H can be estimated as 25m/s for the calculation of the velocity head q for H = 4m. To put his into perspective, winds speeds above 20 m/s are often considered dangerous; according to the Beaufort scale, they can knock a pedestrian over. Applying these numbers to Eq. (5.1) gives the results presented in Fig. 5.2. The single vortex is predicted to produce enough suction on the short side of the TTU building to lift 2300 kg (5000 lbs). This is one quarter to one third the weight of an occupied single-wide mobile home (Schriever 1977), and helps to explain why it is recommended that smaller mobile homes be securely tied to the ground.

Fig. 5.2 also shows two one-meter square areas which experience comparable lift from the vortices. Area A, at the corner, experiences enough force to lift 80 kg (180 lbs.) from each of the two vortices, while Area B also experiences a total vortex induced lift of 160 kg. In general, with the exception of the area right in the roof corner, the worst suction that a rooftop appurtenance will experience will be when that item is as close to the leading corner as possible, while still completely within the separated flow triangle. This has been confirmed qualitatively by one of the failure modes observed at CSU for a roof-top mounted solar panel array. As the wind speed is increased, it is the panels which are closest to the leading corner and also completely under the vortices which first begin to lift off of the roof surface.

This problem can not be easily avoided by placing roof mounted items away from the zones of flow separation, since almost all most of the roof is under the separated flow for one wind direction or another. As we will see, this problem is also exacerbated by low parapets, which enlarge the vortices and move them further towards the roof center without reducing the suction. Even if roof-mounted items are not an issue however, the amount of force exerted on the roof itself is enough to cause the roofs to come off of homes that are not properly equipped with hurricane straps.

The analysis of Chapters 2 and 3 suggests that the problem of extreme vortex induced suction can be reduced or eliminated if the reattachment is inhibited and the flow curvature near the leading edge increased. It has long been known that the vortices can be eliminated by installing curved roof edges, which effectively prevents the flow separation from occurring at all (Richardson and Surry 1994). However, this is not necessarily a practicable solution for existing structures, so this chapter examines a couple of techniques for the mitigation of extreme rooftop suction which can be applied to existing low rise buildings with sharp roof edges. This is accomplished by passively venting the separated flow using a porous parapet or a roof-mounted airfoil or spoiler. The success of the porous parapet has been reported elsewhere, where it was found to provide greater suction reduction than range of devices designed to smooth the flow around the corner or to disturb the vortices with items place near the core (Surry and Lin 1995). To the author's knowledge, the spoiler has not been used elsewhere.

It is anticipated that the mitigation devices developed in this study will be of use for any roof shape, as well as for all flow directions, including bubble separation.

5.2 Experimental procedures

The model scale experiments were conducted in the Meteorological boundary layer wind tunnel at using the BII boundary layer as described in Chapter 3. Flow visualization was also performed. Initially, the 1:50 scale model of the TTU WERFL building was used (recall Fig. 3.2). However, because of the small size of the opening between the spoiler and the roof surface, a 1:25 scale model of the TTU WERFL site was used for subsequent tests in the same boundary layer. In this case, pressure tap locations matched those currently in place at the full-scale site, with some additional taps added as indicated in Fig. 5.3. The tap diameter was 0.5 mm, and the same tubing system was used as for the 1:25 tests. Wind tunnel test duration was 36 seconds, which is equivalent to 15 minutes at full scale; during this time, 16,384 data points were collected at each of the 48 taps at a frequency of 455 Hz. All mitigation tests on the 1:25 model were taken at a wind angle of $\omega = 50°$. Testing of the porous parapet was also conducted on the 1:25 model. Only the spoiler has been tested at full scale.

The basic configurations for which results will be presented in this chapter are depicted in Fig. 5.4 and are described below:

i. The spoiler: 9 mm wide, at an angle of 10° to the roof, with an overhang of 2mm, mounted 6 mm above the surface.

ii. The mesh porous parapet: 10 mm high, consisting of two layers of 70% porous wire mesh or screen, combining to produce a ~50% porosity. (some results using just a single layer of the wire grid are presented as well)

iii. The circular hole porous parapet: a 1mm thick metal sheet with 3.5 mm diameter holes (50% porous)

iv. The slatted fence porous parapet: A fence of 1mm wide metal strips, angled at 45°, with 13 mm between the vertical supports and 1.5mm between the individual slats.

v. A cylindrical railing, 6mm in diameter and 5mm from the surface

vi. A solid parapet, 10mm high and 5 mm thick.

5.3 Results

One design goal was to attempt to devise a means of passively venting the flow separation to prevent vortex formation and early flow reattachment with a minimal impact on the visual appearance of the roof edge. A wide range of parapet and spoiler sizes and positions were compared. The results of all of these tests will not be presented here, but are summarized as follows:

I. Angling the slats and the spoiler towards the roof surface improves mitigation

II. An overhang improves the spoiler performance

III. Increasing the porous parapet height beyond 10 mm had no effect.

IV. Introducing an opening beneath the full parapet, or sealing the top half of the porous parapet, both provide mitigation comparable to the porous parapets

V. Details, such as the location of the supports and the presence of small blockages or openings in the fence, have little effect on the overall mitigation effectiveness.

The details of how the mitigation device is attached to the roof, can, however, significantly affect the pressures at a specific tap, especially very close to the leading edge, where taps can be beneath the spoiler. The use of a single extreme suction tap near the leading edge can also provide misleading information, as in the case of the solid parapet, which simply causes the vortex to move away from the roof edge, without reducing the suction.

To truly capture the effects of the unmitigated vortex, a sufficient tap density is also required along a given x = constant line. This is only the case for the x = 1.44m (nominal 5ft) and x = 1.13m (nominal 9ft) lines. (Recall that in Fig. 1, only a single tap was beneath the separation for the first two tap rows, so that the profile shapes and peaks had to be estimated from the pressures profiles of other rows farther from the corner). As a result, the results reported here will focus on the "5ft" and "9ft" rows. Since the pressures are so well correlated beneath the entire vortex, the data from these rows is actually expected to provide a better indication of the suction at x = 0.5m than data from tap #2.

The question of whether the pressures at individual taps should be considered at all can be raised. Would an area average provide a better indication of mitigation effectiveness? This depends on what aspect of the building design is being considered. For individual solar panels or pavers, pressured averaged over areas such as those depicted in Fig. 2 are necessary. For the whole building load, the whole roof needs to be considered. For gravel scour or shingles, individual point pressures are required. Point pressures also take on added relevance if a single point can be expected to pressurize the undersize of a roof-mounted item such as a paver. This study presents primarily point pressure data, for consistency with data presented in earlier chapters, but the data gathered in the study could certainly be used to calculated various area averages.

Care must be taken in drawing conclusions from individual taps away from the leading edge as well, though. Fig. 5.5 shows the histograms for taps 18, 19 and 20, for two of the porous parapets. For tap #20, the 70% porous mesh has the lowest mean suction (Cp = -0.94, compared with Cp = -1.26 for the 50% porous plate and Cp = -1.30 for the bare roof). However, like the bare roof histogram, it displays the bi-modal hump characteristic of a tap in the re-attachment zone (recall Fig 4.12b, for $\omega = 35°$), indicating that there is still considerable streamline curvature, possible due to the continued presence of a vortex. Since the vortex is weakened, but still present, the peak suctions remain higher than for the circular-hole porous parapet.

Conversely, the nearly identical pdf's for the circular hole parapet at all 3 taps indicate the presence of a large, low curvature separation bubble.

The reduction of peak suction can be used as a simple measure of mitigation effectiveness, since it is often the occurrence of extreme event which is the limiting factor. However, a single peak event is not a robust statistic, and certainly would not be recommended for fine tuning a mitigation device. A statistic based on the tail of the probability distribution would be more appropriate.

With these caveats in mind, Fig 5.6 presents the mean and peak pressures for the "5ft" and "9ft" rows for the various configurations described above. The spoiler is seen to be the most effective of the mitigation devices for reducing both the mean and the peak suction. The various porous parapets provide comparable overall mitigation, though the circular holes appears to provide the best peak reduction. The single circular cylinder railing provides the least mitigation of the devices shown. The low solid parapet is not considered a mitigation measure, since it worsens the mean suction and provides comparable peak suction to the bare roof corner. This confirms the results of previous studies (Sun 1993).

5.4 Discussion

5.4.1 Measuring Mitigation

All of these mitigation devices work by splitting the shear layer at the roof corner, and allowing the flow which passes under or through the device to disrupt the vortex (see Fig. 5.7). Without the vortex, the flow curvature above the separated flow in reduced, as shown in Fig 5.8. The suction reduction can be quantified by using the vortex suction equation, Eq. (4.5). With no vortex, g is reduced to 0, so that Cp_S is simply the same as Cp_M:

$$Cp_S(t)=\left(\frac{U_M(t)}{\overline{U}_M(\omega(t))}\right)^2\left[1-\left(\frac{\overline{U}_M(\omega(t))}{\overline{U}_{ref}}\right)^2\right] \tag{5.2}$$

Fig. 5.9 shows the change in Cp at tap #19 with wind direction. The data is from the full-scale facility at TTU, where tap #19 corresponds to tap # 50501. The value of Cp reaches a maximum near ω = 70°; this can be explained by Eq. (5.2), since U_M/U_{ref} reaches a maximum at this angle (recall Fig. 3.11).

Fig. 5.10 shows that the mitigated pressure patterns also follow that of U_M (and that of the bare roof) when distance from the corner is considered. This is also the result of an increase in local velocity towards the roof corner. This was shown in Fig 3.10(a), but it could be argued that some of the increase in velocity directly above the vortex was the result of the additional curvature created by the vortex. However, the flow speed directly above the leading edge also increases with decreasing x, as shown in Fig 5.11.

The dependence of Cp on the local velocity underlines the limits to mitigation. The flow passing over an isolated building must accelerate, and the mean value of U_M/U_{ref} near the corner is not likely to drop below 1.4 for ω = 50° without substantial changes to the upstream conditions. This implies a mean Cp of –1 according to Eq. (5.2), which is what has been observed in this study. If the flow is also turbulent, then Eq. (5.2) also dictates that the Cp(t) probability distribution follows that of U^2, as described in Chapter 4. A Cp(t) pdf based on Eq. (5.2) is shown in Fig. 5.12. The Cp(θ) curve from Fig. 5.9 was used to calculate $f_{Cp(\theta)}$ as described in Chapter 4. Both curves have been scaled to match the histograms presented in Fig 5.5, where the 16384 data points were binned into groups with $\Delta Cp = 0.1$. The curves indicate that the peak suction event for the test runs performed at CSU for tap #19 (50501) is expected to be –3.2. This can be seen as a limit to the potential for suction reduction; if the mean flow speed above the roof edge is 1.4 times the reference velocity, and the turbulence intensity is 20%, minimum Cp values below –3 near the leading edge cannot be eliminated.

The flow velocity at the roof edge can be reduced by items which act as windbreaks to the upstream flow, such as trees or nearby buildings. Generally, however, while the haphazard surrounding windbreaks may be sufficient to reduce the number of wind directions for which the vortices form and high local winds exist, if any upstream fetch permits an unabated cornering wind, extreme suction peaks characteristic of an isolated building will be possible (Surry and Lin 1995). For this reason, mitigation devices could prove helpful even in more densely built areas such as suburbs.

5.4.2 Relative merits of various mitigation techniques.

The spoiler is not only the most effective of the mitigation measures tested, it is also the smallest addition to a roof corner. The full scale airfoil tested at TTU measures only 10cm x 2cm, and tests at CSU show little or no improvement from using a larger airfoil. There are some drawbacks, however. Rough calculations indicate that the spoiler is expected to generate twice as much lift as an equivalent area under the vortex. Since the spoiler is quite small compared to the vortex region, there is a net suction reduction, but a poorly installed spoiler could worsen the situation right at the roof edge. The lift force of the spoiler needs to be measured experimentally. The spoiler is also mounted very close to the roof edge, and the venting region between the spoiler and the roof could get plugged by debris in a storm.

The cylindrical railing, with a drag coefficient near 1.0, will also generate an upward force since the flow passes over the corner at an angle, but there considerably less lift than for the spoiler. The cylinder is also, however, appreciably less effective.

The porous parapets offer a solution where a device with lift cannot be suitably attached to the leading edge of the roof. There is considerable drag ($C_D \sim 1.2$-1.5 for most designs), but this will be transferred into a downward force on the roof by the parapet supports, which would in general be beneficial.

5.5 Conclusions

Several methods of reducing the high peak suctions experienced beneath separated flows on rooftops have been investigated through a wind tunnel and full-scale study of pressures on the TTU WERFL building. All of the methods offer significant reductions in peak surface pressures by venting the separated flow zone. The most effective technique involves the use of a small spoiler or airfoil mounted the roof's edge.

The resulting mitigated pressures approach the minimum suction that is considered attainable for an isolated building, which is determined by the flow speed at the roof edge. Typical results show a 50% reduction in the worst-case Cp values. Visualization and the analysis of the rooftop pressure patterns indicate that this is achieved through the elimination of the vortices in the separated flow zone.

5.6 References

Lin, J.-X., Surry, D., and Tieleman, H. W. (1995), "The distribution of pressure near roof corners of flat roof buildings", *J. Wind Eng. Ind. Aerodyn.*, **56**, 235-265.

Richardson, G. M., and Surry, D. (1994), "The Silsoe Structures Building: Comparison between full-scale and wind-tunnel data", *J. Wind Eng. Ind. Aerodyn.*, **51**, 157-176.

Schriever, W. R. (1977), *Wind forces on Mobile Homes*, produced by National Research Council Canada, June 1977.

Simiu, E., and Scanlan, R. H. (1986), *Wind Effects on Structures*, John Wiley & sons, Inc., New York

Stathopoulos, T., Kumar, K. S., and Mohammadian, A. R. (1996), "Design wind pressure coefficients for monoslope roofs: A time series approach", *J. Wind Eng. Ind. Aerodyn*, **65**, 143-153.

Sun, Y. (1993), *Wind loading on loose-laid roofing paver systems*, Ph. D. thesis, Department of Civil Engineering, University of Colorado, Fort Collins.

Surry, D., and Lin, J. X. (1995), "The effect of surroundings and roof corner geometric modifications on roof pressures on low-rise buildings", *J. Wind Eng. Ind. Aerodyn*, **58**, 113-138.

Xu, Y. L., and Reardon, G. F. (1998), "Variations of wind pressure on hip roofs with roof pitch", *J. Wind Eng. Ind. Aerodyn.*, **73**, 267-284.

5.7 Figures

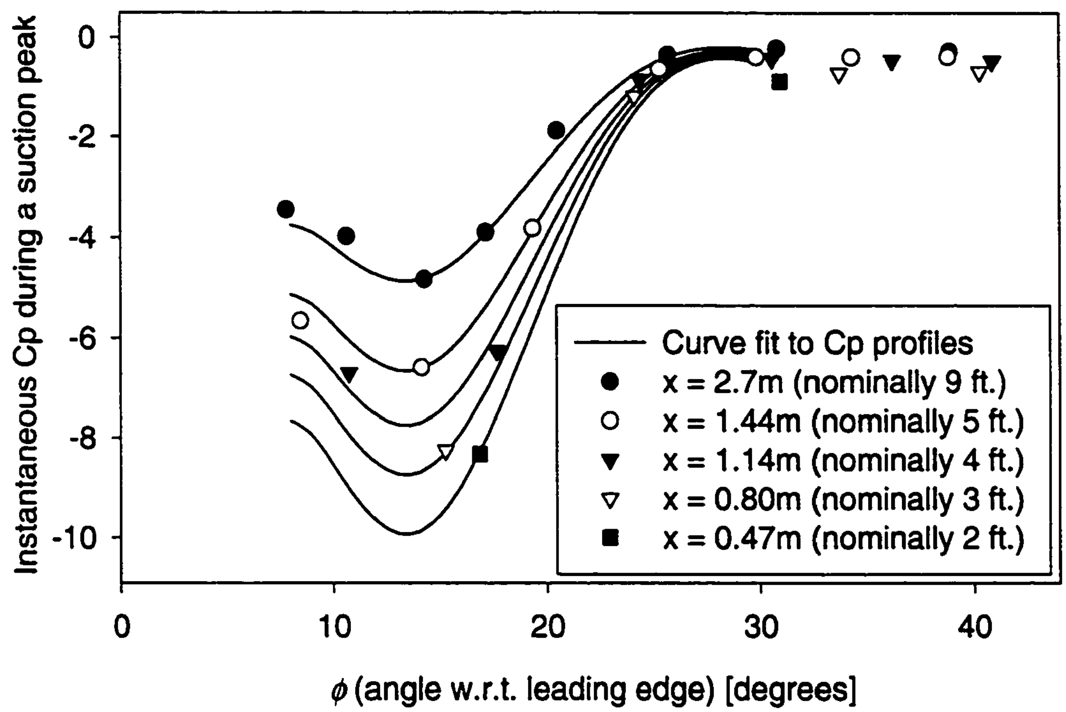

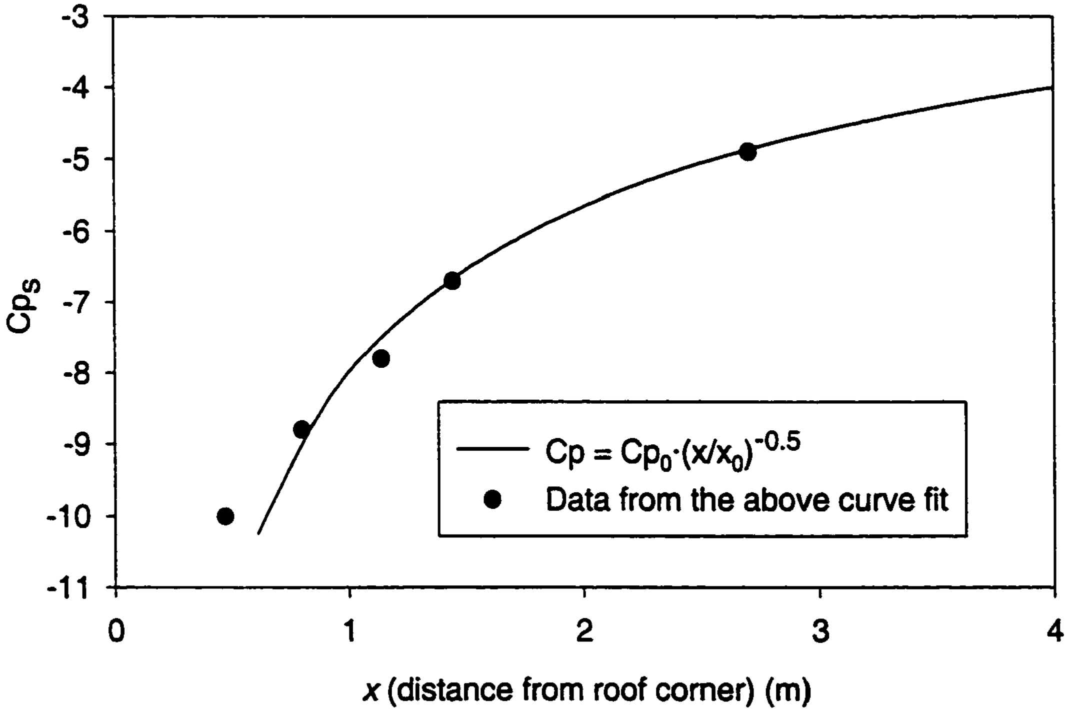

Figure 5.1: Measured and expected pressure profile data under the vortex core for various lines normal to the roof edge for $\omega = 50°$.

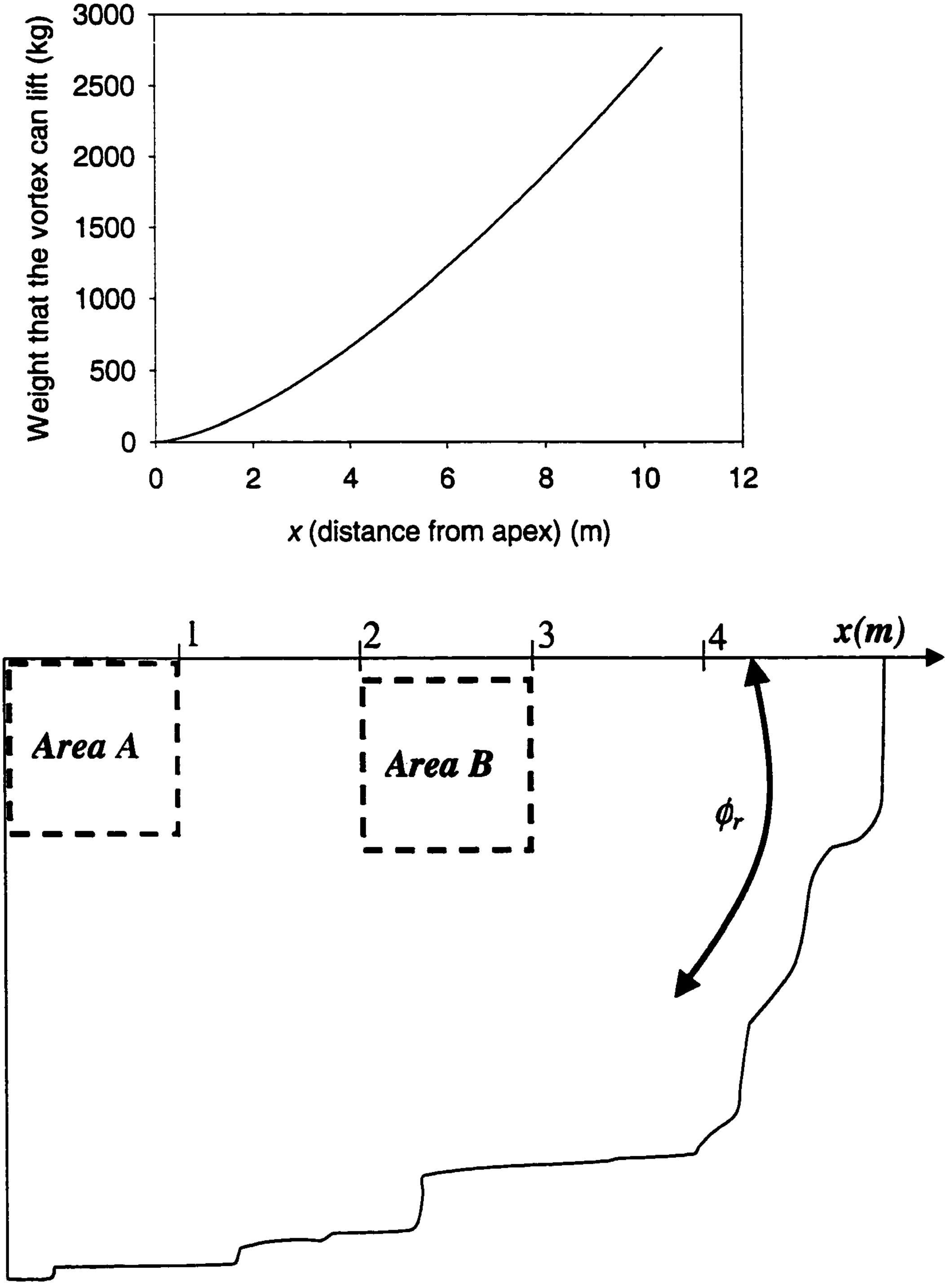

Figure 5.2: Cumulative force of vortex on shaded area.

	“2ft.” row	
tap#	x (mm)	y (mm)
2	18.5	5.6
3	18.5	11.1
4	18.5	18.6
	“3 ft” row	
tap#	x (mm)	y (mm)
7	31.6	8.6
8	31.2	14.0
9	31.5	21.0
10	31.5	26.7
	“4 ft” row	
tap#	x (mm)	y (mm)
11	44.8	8.5
12	44.0	14.0
13	44.5	20.2
14	45.0	26.6
15	44.6	32.6
16	44.6	38.6
17	45.0	44.6
	“5 ft” row	
tap#	x (mm)	y (mm)
18	56.5	8.4
19	56.6	14.2
20	57.0	20.0
21	56.6	26.8
22	57.0	32.7
23	57.0	38.8
24	56.6	45.5
25	56.3	56.2
26	54.5	63.0
27	59.0	112.0

	“9 ft” row	
tap#	x (mm)	y (mm)
28	106.0	14.5
29	106.1	19.9
30	106.5	27.0
31	107.0	33.0
32	106.4	39.7
33	106.0	51.1
34	106.5	63.5
35	106.5	85.8
36	107.0	112.0
	other taps	
37	183.5	126.0
38	183.5	226.0
39	183.5	324.5
40	183.5	424.0
41	258.5	28.0
42	258.5	126.5
43	12.4	272.0
44	85.3	272.0
45	282.7	272.0
46	355.0	272.0
1	12.1	14.6

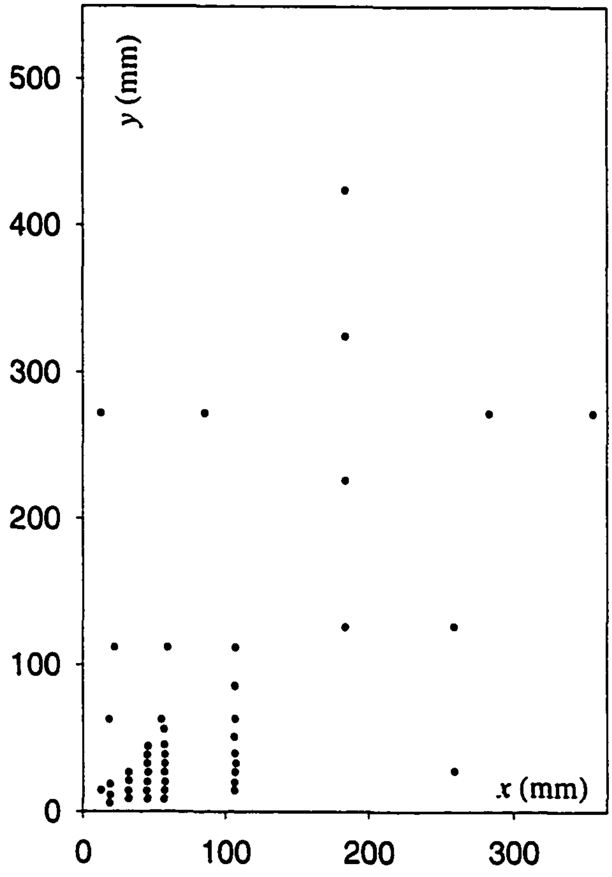

Figure 5.3: Tap locations on 1:25 TTU WERFL building model roof. Taps 1-3, 5, 6, 11-14, 18-23, 26-34, & 36 correspond to taps installed on the full-scale site.

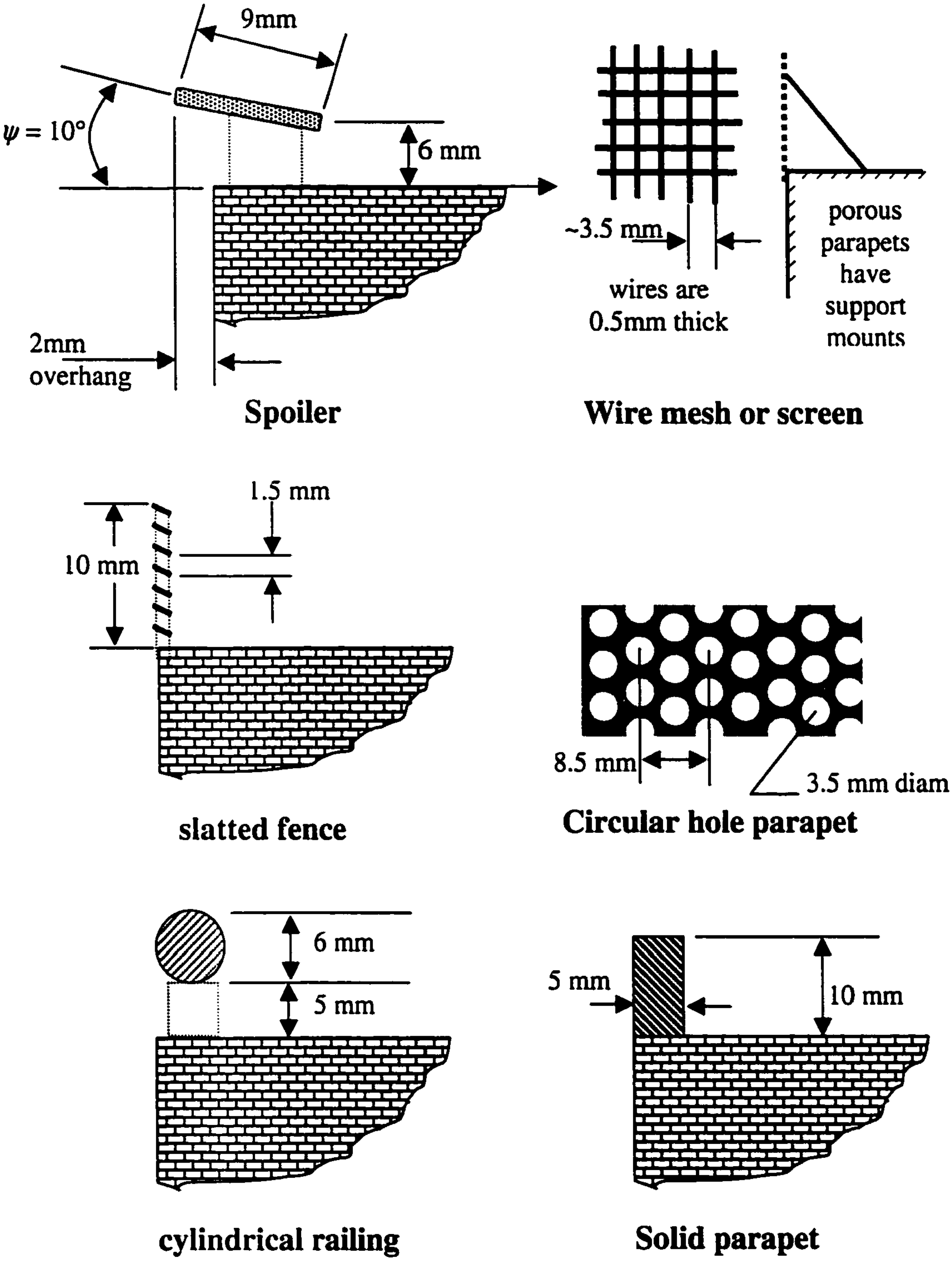

Spoiler

Wire mesh or screen

slatted fence

Circular hole parapet

cylindrical railing

Solid parapet

Figure 5.4: Schematic illustrations of mitigation device configurations and dimensions

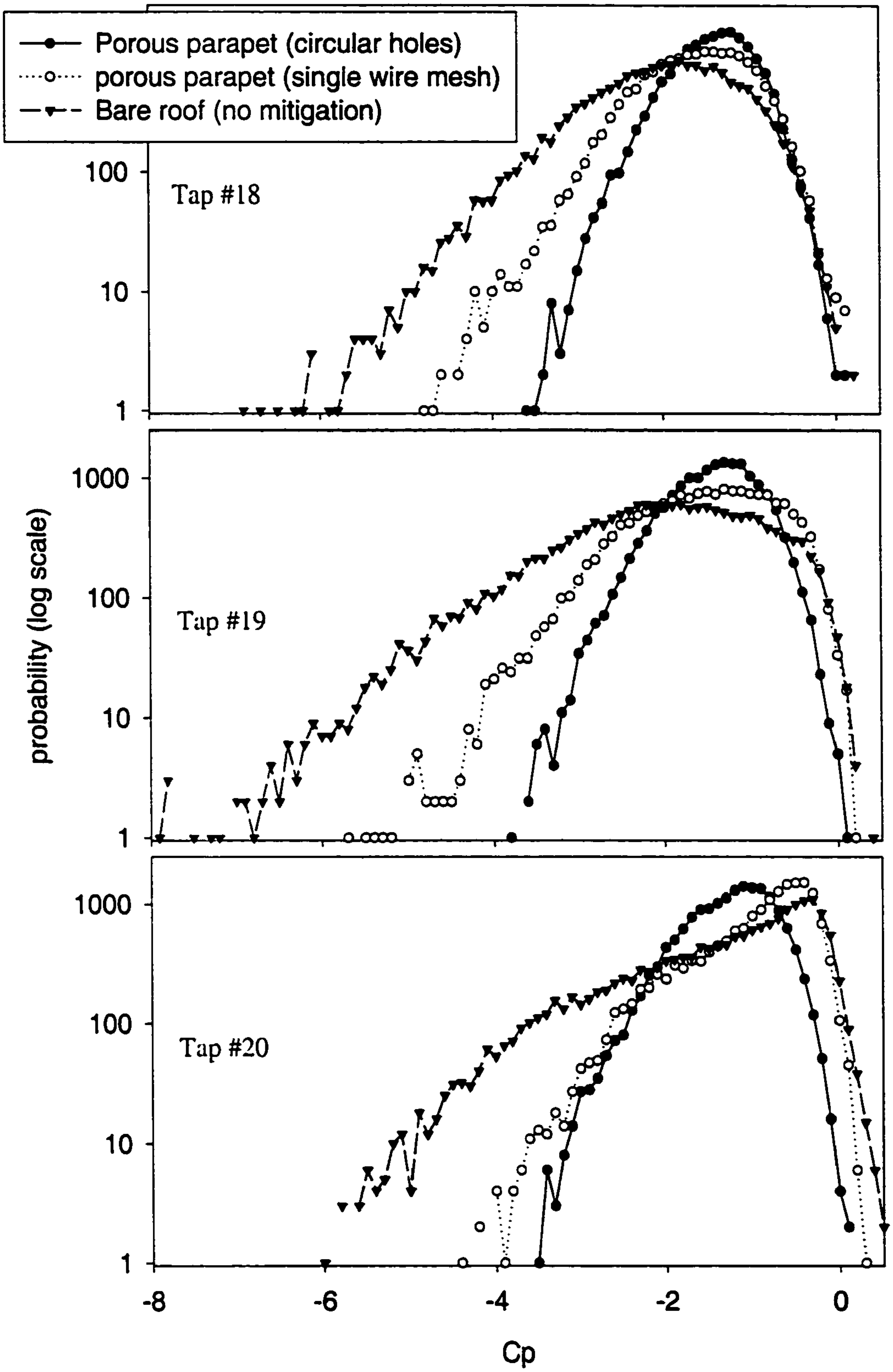

Figure 5.5: Histograms of Cp for 3 taps in the x = 1.44m row.

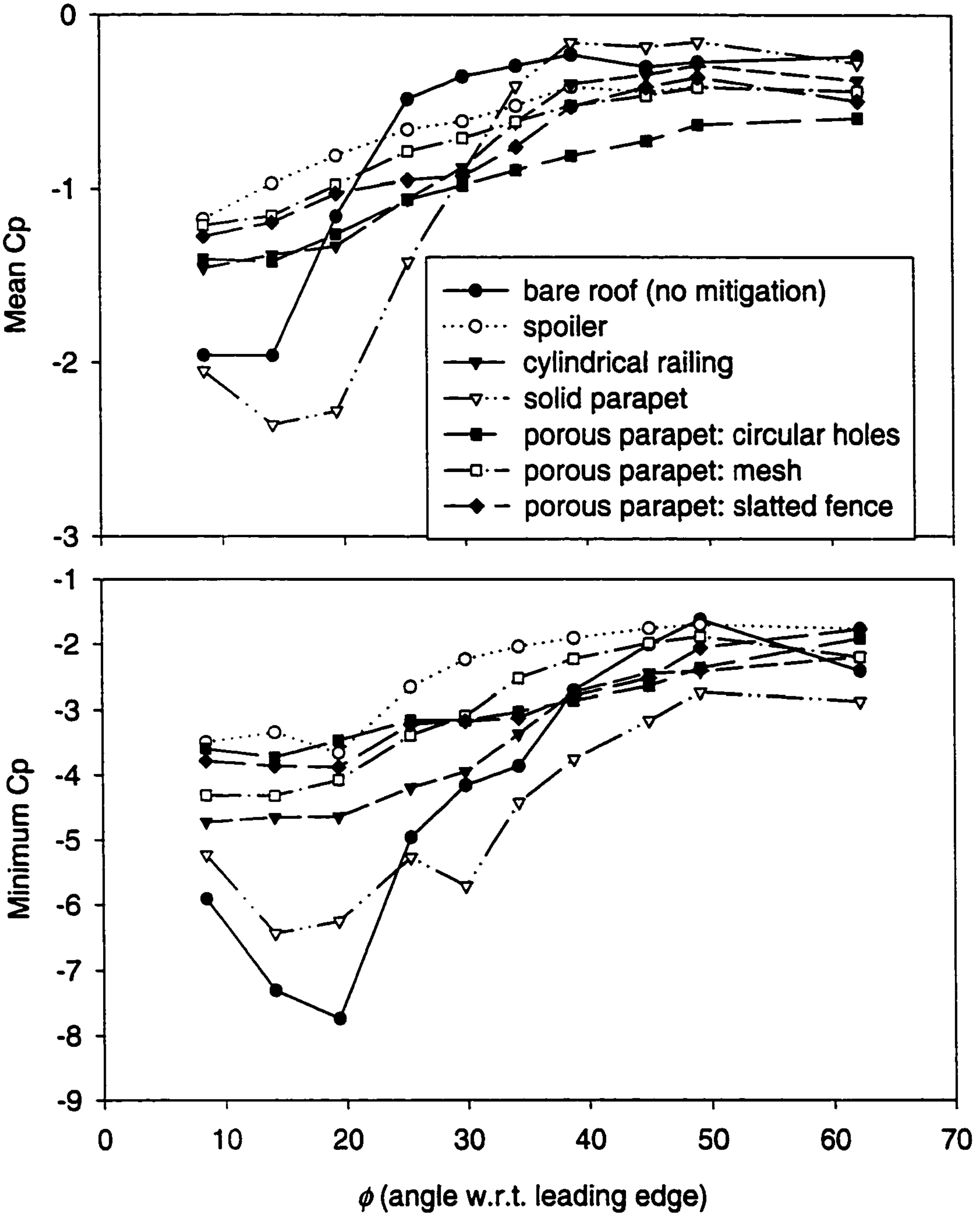

Figure 5.6 Roof-top pressure coefficients with and without mitigation measures for $\theta = 220°$ (which for these taps means that $\omega = 50°$)

(a) Row of taps at 1.44m (nominally 5 ft) from the corner

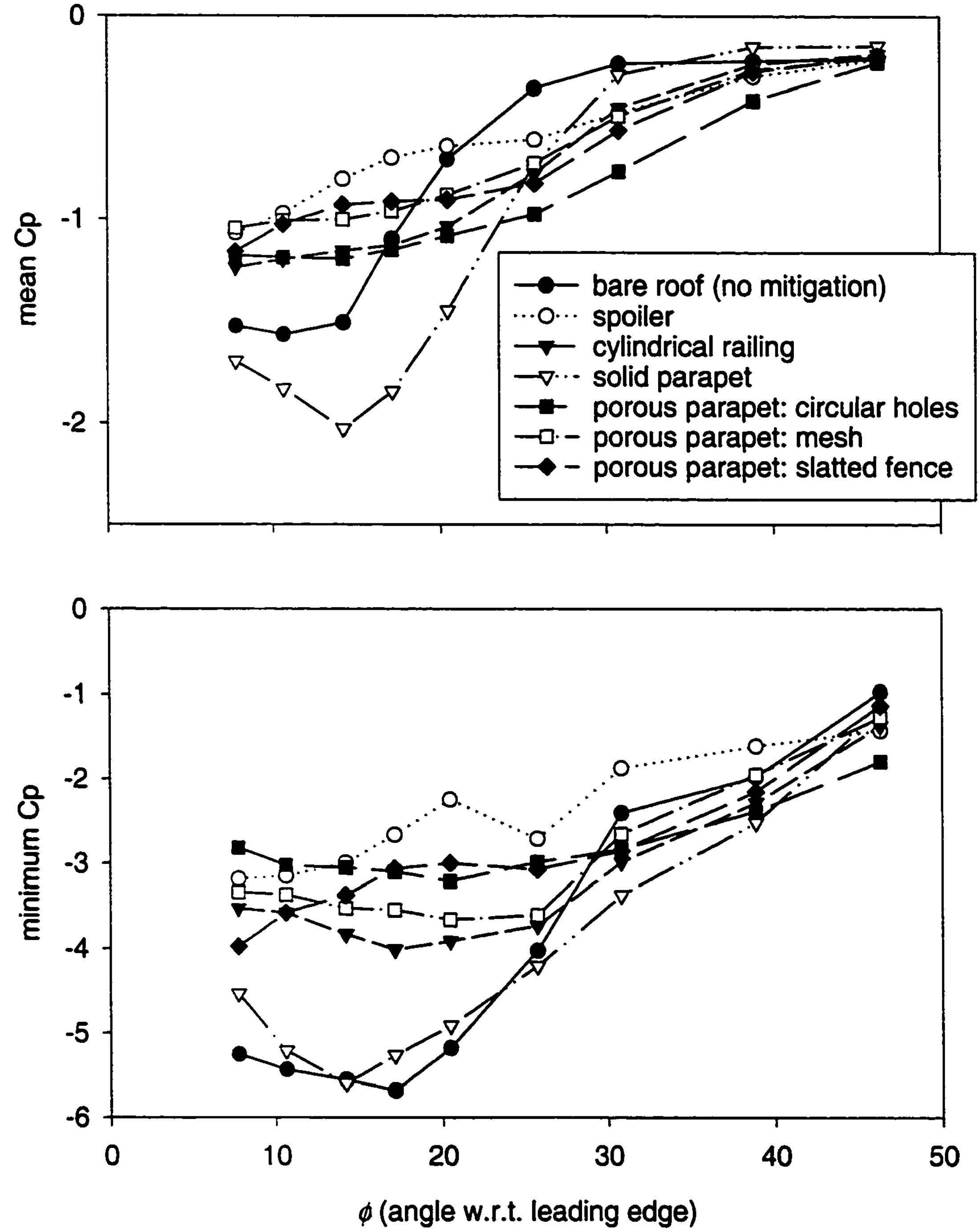

Figure 5.6 (continued) (b) Row of taps 2.70m (nominally 9 ft.) from the corner

(a) Porous parapet: slated fence

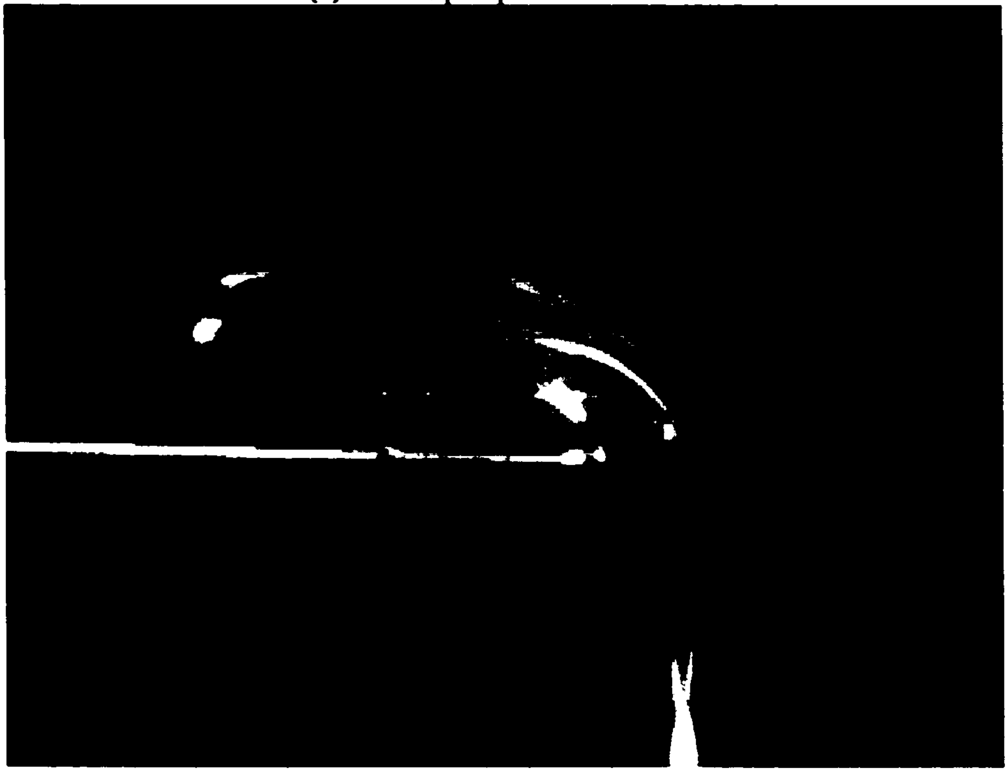

(b) Spoiler

Figure 5.7: Visualization of flow over a porous parapet. Flow is from right to left. Building corner is dark rectangle in the lower left. In (a), Horizontal black lines are the parapet bars; in (b), upper horizontal white line is the top of the far wall's spoiler.

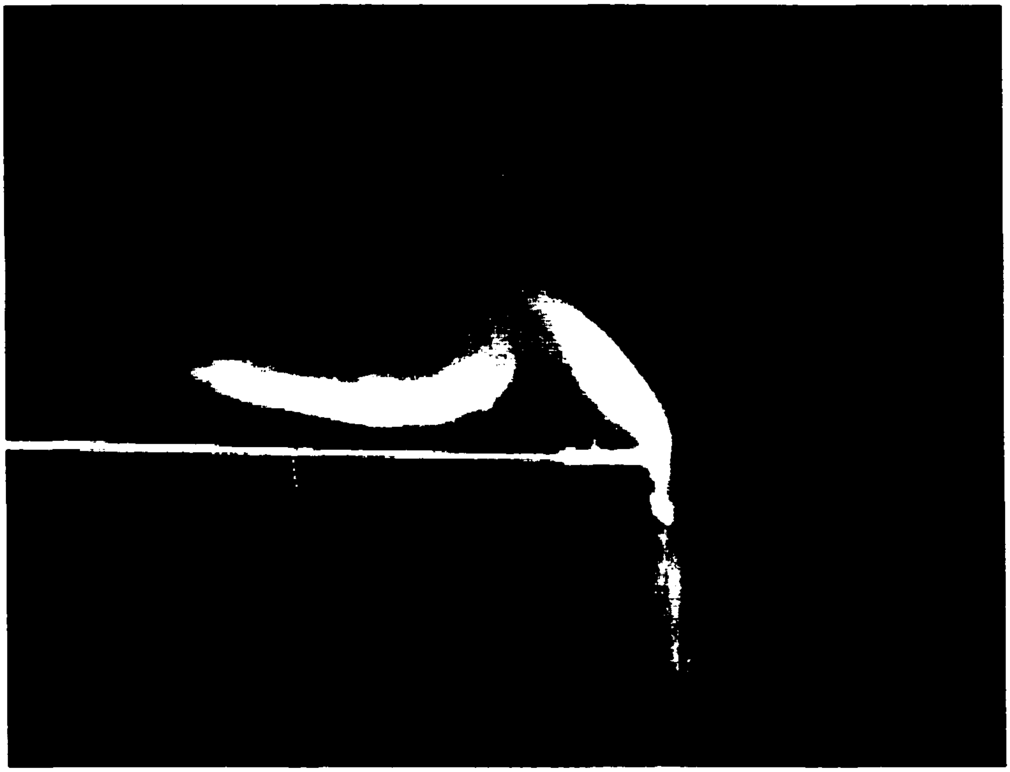

(a) vortex

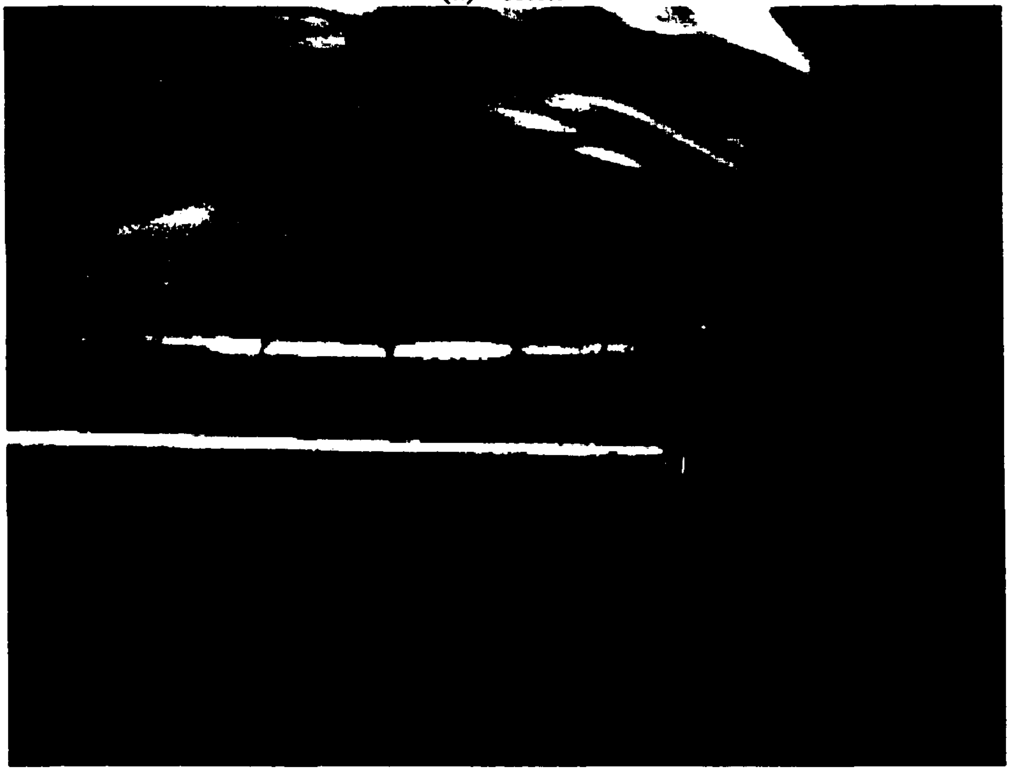

(b) Porous parapet: slatted fence

Figure 5.8: Change in flow separation due to the mitigation devices.

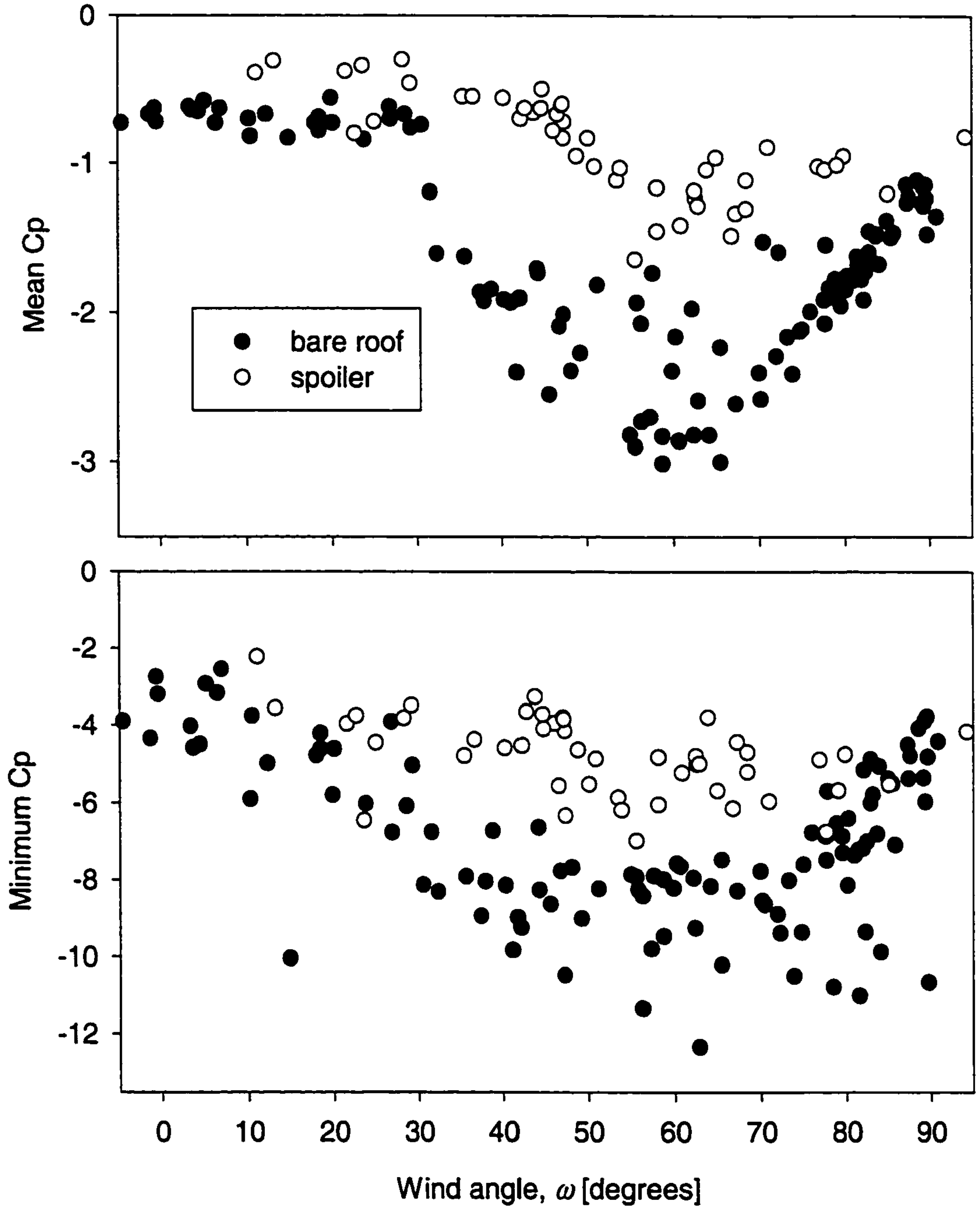

Figure 5.9: TTU data: effect of spoiler at full scale on tap 50501, which corresponds to tap #19 on the 1:25 model. Spoiler is 10cm wide and 3.65 m long. It is mounted 8 cm above the roof surface, with a 1 cm overhang. It is angled at $\psi = 11°$ to the roof surface.

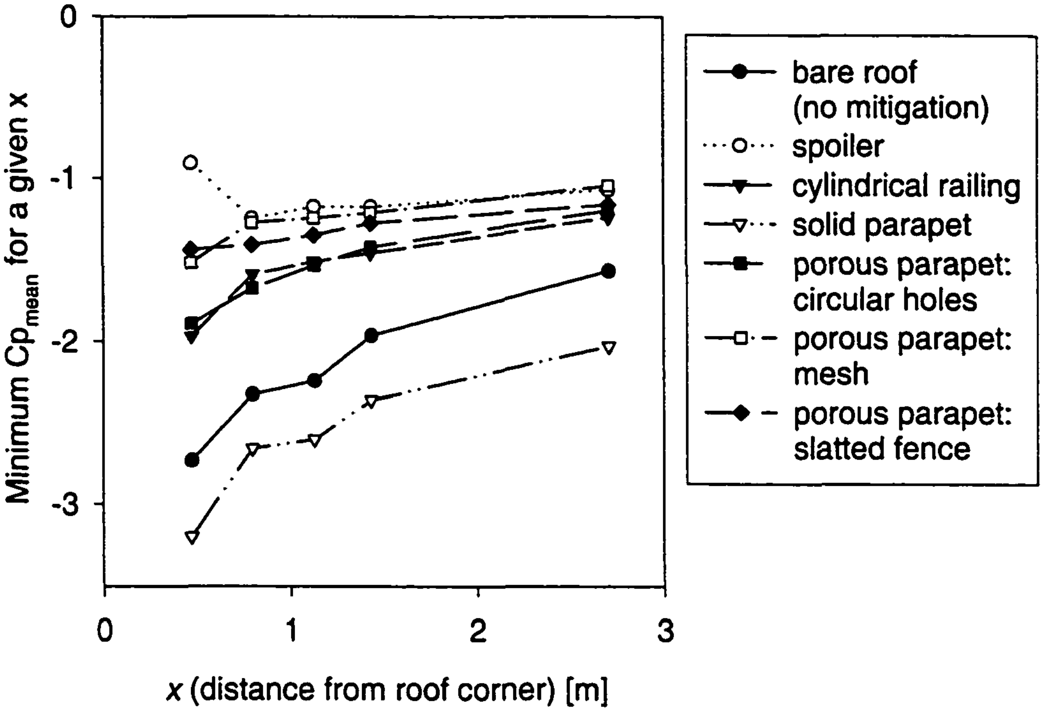

Figure 5.10: Change in mean Cp with distance from the corner for various mitigation techniques

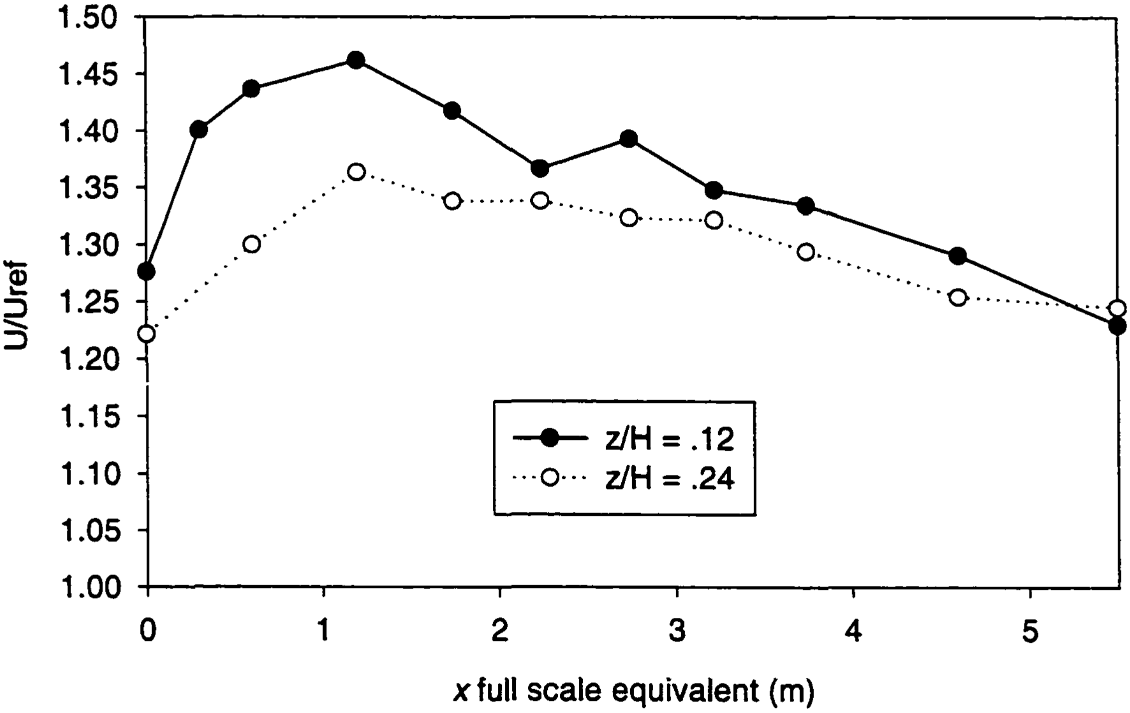

Figure 5.11: Change in velocity directly above the leading edge for $\omega = 45°$ (data from 1:50 model)

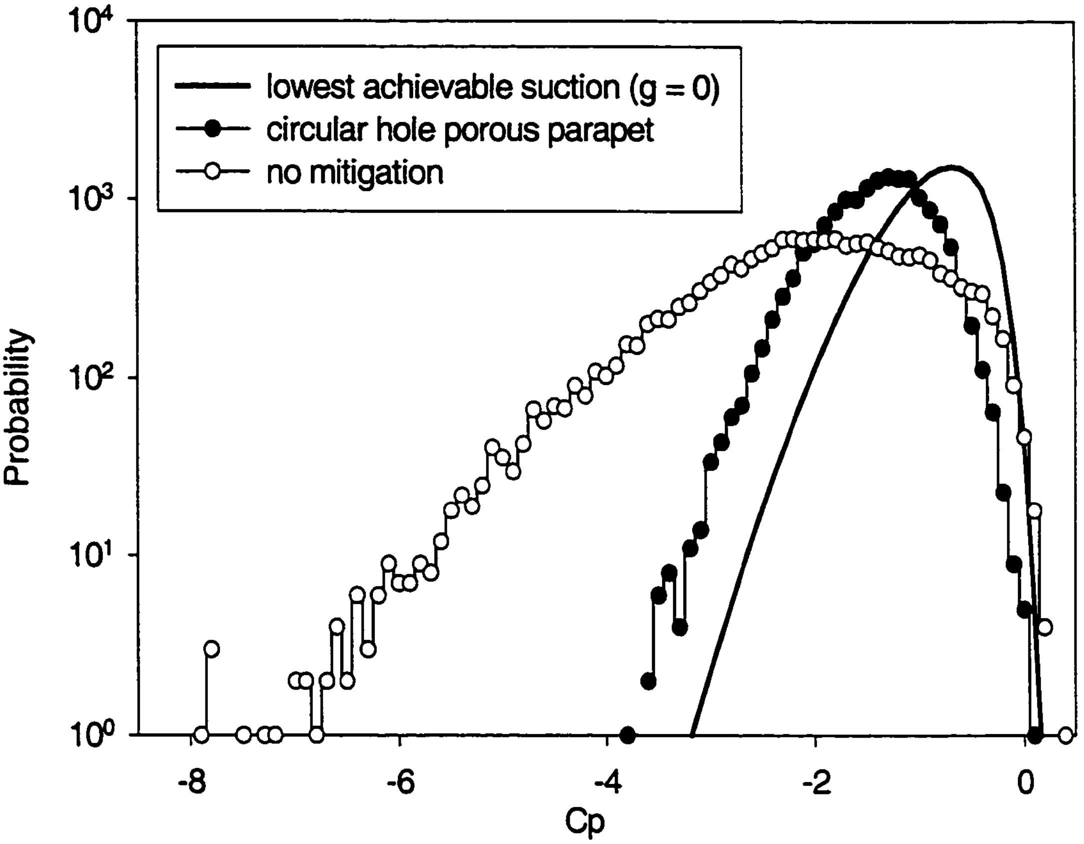

Figure 5.12: Histograms for 16384 samples, $\Delta Cp(t)$ bin size = 0.1. The data (circles) is from Figure 5.5 for tap #19. Lowest achiavable suction histogram (thick line) is based on probability density functions calculated from Eq. (5.2). The probability = 1 intercept indicates expected minimum Cp for a 36 second wind tunnel or 15 minute full-scale run.

CONCLUSIONS AND RECOMMENDATIONS

In order to better understand the vortex mechanism which produces extreme peak suction events on the roofs of low-rise buildings, this study has performed the first simultaneous recording of flow images, multiple surface pressures, and flow velocities for a conical roof edge vortex.

The results of these wind tunnel experiments have

1) confirmed and quantified several known trends:

- The conical vortex along a given roof edge gets larger as the flow becomes more normal to that roof edge.
- Turbulence in the upstream flow moves the vortices towards the roof edge when compared to the position of the vortices in smooth flow.
- The peak suction events under the separation bubble (for winds normal to the wall) are the result of unstable vortices which form at irregular intervals and locations on the leading edge, and which are convected along the surface at irregular intervals.

2) settled some previous questions:

- Peak suction occurs beneath and follows the motion of the primary vortex core, and not under a secondary vortex.
- In turbulent flow, vortex size is an indicator of wind direction, and only acts as an indicator of suction strength because certain wind directions produce greater suctions.

- The considerable vortex motion and the asymmetric pressure profile beneath the vortex account for the location of the greatest mean and rms Cp values.

3) revealed some new facts:

- For a given distance from the corner x, smaller vortices cause higher suction in smooth flow.
- While instantaneous wind direction changes control the expected vortex position, there is considerable random vortex motion about this expected position.

Based on the experimental observations and the need for more insight into the problem, a new model of the vortex flow mechanism was developed to replace the existing and flawed potential flow model. This model is embodied in Eq. (4.5) and links the instantaneous surface pressure directly to the flow vector fluctuations at the roof edge, and quantifies vortex quality with a new parameter, the amplification factor 'g'. There has been a good deal of discussion in the wind engineering literature concerning the effects of upstream turbulence on suction beneath the vortices, and the model can be used to explain how the various components of incident turbulence influence surface pressure. In particular, the role of lateral turbulence, which has often been emphasized, is explicitly described in terms of fluctuations in the local wind direction.

The model is experimentally verified, and is shown to explain several aspects of vortex behaviour, such as

- The increase in suction toward the corner (the local velocity increases)
- The minimum mean Cp at $\omega = 60°$ (the velocity reaches a maximum near $\omega = 65°$, and the wind component normal to the vortex increases with ω while the vortex stability decreases.)

- How peak Cp's below –10 can be achieved with gusts only 60% above the mean, and total speeds of only 2.4 times the reference mean.

An analysis of the vortex mechanism flow model indicates that the quasi-steady theory should be able to predict the fluctuating surface pressures beneath the vortices, with the exception of terms related to

i) random changes in the vortex position (beyond changes related to wind direction shifts)
ii) changes in the vortex strength related to the reattachment and the curvature, as expressed by g.

The relative impact of these terms is assessed and found to be comparable to the effects of wind direction shifts (i.e. low frequency lateral turbulence). It is conceivable that these terms could be incorporated in the lateral and longitudinal turbulence terms, respectively.

The predominant conclusion in wind engineering literature is that the quasi-steady theory does not accurately predict fluctuating pressures under the vortices. One reason why earlier studies rejected the quasi-steady theory is that they performed neither a full theoretical assessment of the quasi-steady implications, nor an experimental evaluation of the quasi-steady assumptions. Both of these were done in Chapter 4. The basic assumption that instantaneous wind direction shifts have the same effect as longer term changes is shown experimentally not to be valid unless $35° < \omega_{mean} < 55°$. However, because of the dominant effect of longitudinal turbulence and because of the crucial nature of the $35° < \omega_{mean} < 55°$ angles, the fully evaluated quasi-steady theory is able to predict the skewed and bimodal probability distributions for taps near the vortices reasonably well. The quasi-steady theory should not be used to estimate peak pressures, however, especially for the case of the separation bubble. When the quasi-steady theory is applied, $Cp^{inst}(\theta)$ ought to be calculated and used.

Finally, the insight provided by the flow model suggests the design of suction mitigation devices which passively vent the separated flow zone to prevent vortex formation and early reattachment. A novel device, the vortex spoiler (developed initially by researchers at Texas Tech University) produces the best results when compared to several variations of the most effective device currently found in the literature, the porous parapet. The flow model suggests that the mitigation provided by the spoiler approaches that which is considered possible for an isolated building in turbulent flow.

Recommendations for future work

While it is surmised that small-scale turbulence (smaller than the size of the building) controls the nature of the vortex shear layer reattachment, this remains unverified. To correlate the location of the reattachment with the presence of small-scale turbulence in the flow over the leading edge, the use of wavelet transforms is suggested. However, these experiments would have to be done at larger scale than 1:25 because of the speed at while the vortex changes. This could be achieved in the wind tunnel using a partial building corner simulation. This technique was investigated early in this research, but remains to be fully developed. The generation of very small-scale turbulence by the leading edge itself may prove to be of interest here.

Pressure tests designed to record the peak suction under the vortex require taps at least every three degrees, starting at the leading edge, to reliably capture the peak event (and hence the core location).